Theoretical Study on Dispersion Force and Isotope Effect in Noncovalent Interactions

非共有結合性相互作用における分散力と同位体効果に関する理論的研究

February 2013

Waseda University
Graduate School of Advanced Science and Engineering
Major in Chemistry and Biochemistry
Research on Electronic State Theory

五十幡　康弘
Yasuhiro IKABATA

Contents

List of abbreviations

AP	approximate spin projection
BFGS	Broyden-Fletcher-Goldfarb-Shanno
BSSE	basis set superposition error
CBS	complete basis set limit
CCSD(T)	coupled cluster singles and doubles with perturbative triples correction
CI	configuration interaction
CIS(D)	configuration interaction singles with perturbative doubles correction
CP	counterpoise
CPU	central processing unit
DFT	density functional theory
EBF	electronic basis function
EOM-CCSD	equation-of-motion coupled cluster singles and doubles
FT	Floris-Tomasi
GIE	geometric isotope effect
GGA	generalized gradient approximation
HF	Hartree-Fock
KM	Kitaura-Morokuma
KS	Kohn-Sham
LC	long-range correction
LDA	local density approximation
LRD	local response dispersion
MAD	mean absolute deviation
MAPD	mean absolute percentage deviation
MD	mean deviation
MkMRCC	Mukherjee's multireference coupled cluster
MO	molecular orbital
MP2	second-order Møller-Plesset

NBF	nuclear basis function
NO	nuclear orbital
NOMO	nuclear orbital plus molecular orbital
NR	nuclear relaxation
PCM	polarized continuum model
PD	parallel-displaced
RPA	random phase approximation
RVS	reduced variational space
SCF	self-consistent field
SOMO	singly occupied molecular orbital
TDKS	time-dependent Kohn-Sham
TDDFT	time-dependent density functional theory
WFT	wavefunction theory
XC	exchange-correlation
XDM	exchange-dipole moment

General introduction

Recent advances in theories, algorithms, and computational capabilities have enhanced large-scale quantum-chemical calculations intended for biomolecules, macromolecules, supramolecules, and molecular clusters. Noncovalent interactions, e.g., hydrogen bond, π-π stacking interaction, and charge-transfer interaction, play an important role in determining geometry, property, and function of these systems. DFT, which is a popular quantum-chemical methodology at present, includes the electron correlation effect through one-body equation similar to the HF method. This is why DFT usually gives reasonable energetics and properties with relatively short computational time. However, most of XC functionals for DFT cannot reproduce noncovalent interactions. Dispersion-dominant interactions are especially difficult to be described, even qualitatively. The dispersion force originates in long-range electron correlation, whereas pure XC functionals are given by local variables such as electron density.

To describe noncovalent interactions within the DFT framework, a number of dispersion correction methods have been developed during the last decade. The DFT-D method by Grimme *et al.* explicitly adds interatomic dispersion energies into the total energy using predetermined dispersion coefficients. Though this method is simple and widely utilized for applications, the empirical nature may deteriorate the predictive capability of quantum-chemical calculations. Nonlocal functionals such as vdW-DF by Langreth, Lundqvist, and coworkers are proposed to enable non-empirical dispersion correction. However, the non-locality requires numerical calculation of doubly spatial integral, which may increase computational time significantly.

Sato and Nakai proposed the LRD method in 2009. Similar to nonlocal functionals, this method computes dispersion correction energy based on electron density. The doubly spatial integral is avoided by the multicenter-multipole expansion. According to the numerical assessment of the LRD combined with the LC-BOP functional, interaction energies and potential energy curves of molecular complexes were accurately reproduced. However, geometry optimization based on the analytical energy gradient of the LRD method was not available. Moreover, these numerical assessments

had been limited for closed-shell ground-state systems. Further theoretical development and assessment of the LRD method were required to enhance the applicability.

While the methodology to treat the dispersion force in DFT is still a developing area, WFT can treat the dispersion interaction through the electron correlation theory such as the MP perturbation and the coupled-cluster method. The systematic improvement of accuracy is possible by increasing the cutoff order of wavefunction expansion. Therefore, one can calculate noncovalent interactions accurately if sufficient computational resource is available.

One of the remaining problems in WFT is the difficulty in estimating nuclear quantum effects and isotope effects, which are important in protonic interactions such as the hydrogen bond. The electronic structure calculation based on the BO approximation is performed using point charges of nuclei. To consider nuclear quantum effects, one has to solve the Schrödinger equation for nuclei based on the potential energy hypersurface obtained by the electronic structure calculation. This procedure is difficult to be applied to polyatomic molecules. The NOMO method is a non-BO theory that describes nuclear wavefunction as the multiplication of NOs. The NOMO method can treat nuclear quantum effects and isotope effects with comparative computational time to conventional WFT. While the NOMO method has been developed to treat not only nuclear quantum effects but also nonadiabatic effects, the application to noncovalent interactions has not been performed.

Part I of this thesis summarizes studies on the extension of the LRD method, which is a density-dependent dispersion correction method for DFT. In Part II, the isotope effect in noncovalent interactions is investigated using the NOMO method, which is a WFT including nuclear wavefunction.

Part I consists of four chapters. Chapter 1 gives the review of dispersion correction in the field of DFT. As for the LRD method, the theoretical background of its low empiricism and computational cost is explained in detail.

In Chapter 2, the LRD method is extended to the SCF treatment. Previous LRD calculations were performed in the post-SCF manner, where the dispersion correction energy is calculated using converged electron density. Since the LRD energy is dependent on electron density similar to XC functionals, it should be extended to fully

SCF calculation by implementing dispersion potential for the Fock matrix. An efficient algorithm enabled us to compute the differentiation of atomic polarizabilities with respect to electron density. According to the numerical assessment, the dispersion potential brought about negligible changes on total energy and electronic distribution. Computational time and number of interactions were also unchanged. Based on the SCF treatment, the analytical gradient of the LRD energy was developed. The inclusion of the LRD energy gradient improved intermolecular equilibrium geometric parameters especially in the case of dispersion-dominated molecular complexes.

In Chapter 3, the performance of the LRD method for open-shell systems is numerically assessed. Dispersion coefficients and atomic polarizabilities by the LRD method behaved reasonably in open-shell atoms and molecules. In open-shell van der Waals complexes, the LRD method combined with the LC exchange provided accurate interaction energies compared to highly parameterized XC functionals. In phenalenyl radical π-stacked dimer, which has a delocalized SOMO, the dispersion correction is essential to reproduce the potential energy curve despite the existence of covalent interaction owing to the overlap of two SOMOs. These results show the usefulness of the LC-BOP+LRD approach for open-shell noncovalent interactions.

In Chapter 4, the LRD method is extended to the excited-state calculation based on TDDFT. Recently, excited-state molecular complexes are studied using TDDFT. Although previous studies applied ground-state dispersion correction to the excited state, the dispersion correction based on excited-state electronic structure has not been examined. In this chapter, state-specific dispersion correction method is developed by using the difference density matrix of TDDFT. Numerical assessment was performed for exciton-localized systems consisting of π-π*/n-π* excited molecule and a ground-state molecule. The LRD method combined with the LC-BOP functional accurately reproduced interaction energies and their shifts from the ground state. Furthermore, the LRD method improved the binding energy of aromatic excimers even though the exciton delocalization and charge-transfer interaction are dominant components of intermolecular attraction forces.

Part II consists of three chapters. Chapter 5 introduces the quantum-chemical theory based on the BO approximation and the NOMO method. The reason why nuclear

quantum effects and isotope effects are easily treated by the NOMO method is also mentioned.

In Chapter 6, the GIE in the hydrogen bond is theoretically analyzed. According to previous experimental and theoretical studies, the isotopic substitution of atom X (X = H and D) in the hydrogen bond A-X···B was found to shorten the A-X bond and elongate the X···B distance. While the intramolecular bond shrinkage is explained by the anharmonicity of potential energy, the intermolecular elongation was not clearly interpreted. In this chapter, the NOMO method is applied to interpret the intermolecular GIE in terms of interaction energy components. First, the RVS-SCF method, which is an interaction energy decomposition method for conventional HF calculations, was extended to the NOMO framework. As a result of calculating the shift of energy components, the intramolecular bond shrinkage was found to weaken the electrostatic interaction. On the other hand, the intermolecular bond elongation was clarified to weaken the exchange-repulsion interaction to stabilize the total system.

In Chapter 7, the GIE in the dihydrogen bond is investigated using the NOMO method. This interaction is represented as A-X···X-B (X = H, D, and T), where the proton acceptor in the hydrogen bond is replaced with negatively charged hydrogen atom. Although the dihydrogen bond has been noticed both experimentally and theoretically, few studies on the isotope effect were reported. In this chapter, geometry optimizations for X = H, D, and T were performed using the analytical energy gradient of the NOMO/HF energy. The averaged distance of X···X increased with increasing nuclear mass. This tendency is opposite to the shrinkage of intramolecular covalent bonds. Thus, the weakening of X···X interaction was discovered as the isotope effect of the dihydrogen bond.

Finally, future prospects are stated after the results of each chapter are briefly summarized.

Part 1

Theoretical Extension and Numerical Assessment of Dispersion Correction Method for Density Functional Theory

Chapter 1
Theoretical Background

DFT is currently a popular quantum-chemical methodology. The electron correlation effect included in one-body equation provides reasonable energetics and properties with relatively short computational time. However, most of XC functionals used in DFT cannot reproduce dispersion-dominant noncovalent interactions. This is why a number of dispersion correction methods including the LRD method have been developed. The first section of this chapter briefly reviews dispersion correction methods proposed for DFT. Then, the formulation of the LRD method is explained.

1.1. Dispersion correction methods for density functional theory

A simple and straightforward approach for dispersion correction is to add atom-atom dispersion energies. The most widely used method based on such scheme is the DFT-D2 proposed by Grimme [1].

$$E_{\mathrm{DFT-D2}} = E_{\mathrm{DFT}} - s_6 \sum_{a<b} \frac{C_6^{ab}}{R_{ab}^6} f_{\mathrm{damp}}(R_{ab}) \tag{1.1}$$

Here, C_6^{ab} denotes the dispersion coefficient for atom pair ab, s_6 is a global scaling factor that depends on the XC functional, and R_{ab} is an interatomic distance. In order to avoid near-singularities for small R, a damping function f_{damp} must be multiplied. The dispersion coefficients are calculated from a formula which couples ionization potentials and static polarizabilities of isolated atoms. A problem with the DFT-D2 method is that the dispersion coefficients are predetermined and constant quantities. Therefore, the same coefficient will be assigned to an element no matter what its oxidation or hybridization state. However, the errors introduced by this approximation can be large, e.g., the carbon C_6 coefficients can differ by almost 35% between the sp and sp^3 hybridized states [2]. As for the refinement of DFT-D2 named DFT-D3 [3], the environmental dependence is captured by considering the number of neighbors each

atom has.

The XDM model [4] is another environment-dependent scheme, exploiting the existence of a region of electron density depletion around an electron, so-called XC hole. This model gives the C_6 coefficient as

$$C_6^{ab} = \frac{\left\langle d_{\mathrm{X}}^2 \right\rangle_a \left\langle d_{\mathrm{X}}^2 \right\rangle_b \alpha_a \alpha_b}{\left\langle d_{\mathrm{X}}^2 \right\rangle_a \alpha_b + \left\langle d_{\mathrm{X}}^2 \right\rangle_b \alpha_a}, \tag{1.2}$$

$$\left\langle d_{\mathrm{X}}^2 \right\rangle_a = \sum_\sigma \int \mathrm{d}\mathbf{r}\ \rho_\sigma(\mathbf{r})\, d_{\mathrm{X}\sigma}^2(\mathbf{r}), \tag{1.3}$$

$$d_{\mathrm{X}\sigma}(\mathbf{r}) = \left\{ \frac{1}{\rho_\sigma(\mathbf{r})} \sum_{ij} \left[\int \mathrm{d}\mathbf{r}\ \phi_{i\sigma}(\mathbf{r}')\, \mathbf{r}'\, \phi_{j\sigma}(\mathbf{r}') \right] \phi_{i\sigma}(\mathbf{r})\, \phi_{j\sigma}(\mathbf{r}) \right\} - \mathbf{r}, \tag{1.4}$$

where α_a is the atomic polarizability, $\rho(\mathbf{r})$ is the electron density, and $\phi_{i\sigma}(\mathbf{r})$ is the ith occupied orbital with σ spin. $\left\langle d_{\mathrm{X}}^2 \right\rangle_a$ is interpreted as the exchange-dipole moment. In the XDM model, the C_6 coefficients are altered through two effects. First, the polarizabilities of atoms in molecules are scaled from their reference atom values according to their effective atomic volumes. Second, the dipole moments respond to the chemical environment through changes of the exchange hole. The computational cost is relatively high, comparable to the cost of a hybrid functional [5].

The methods mentioned above require predetermined input parameters to calculate the dispersion interaction, either the C_6 coefficients directly or the atomic polarizabilities. On the other hand, the nonlocal correlation functional does not rely on external input parameters but rather obtain the dispersion interaction directly from the electron density. The representative is the vdW-DF proposed by Langreth, Lundqvist, and coworkers [6]. Using the vdW-DF, the XC energy E_{XC} is computed as follows:

$$E_{\mathrm{XC}} = E_{\mathrm{X}}^{\mathrm{GGA}} + E_{\mathrm{C}}^{\mathrm{LDA}} + E_{\mathrm{C}}^{\mathrm{vdW-DF}}, \tag{1.5}$$

$$E_{\mathrm{C}}^{\mathrm{vdW-DF}} = \int\int \mathrm{d}\mathbf{r}_1 \mathrm{d}\mathbf{r}_2 \rho(\mathbf{r}_1) \phi(\mathbf{r}_1, \mathbf{r}_2) \rho(\mathbf{r}_2). \tag{1.6}$$

Eq. (1.5) represents that the correlation energy is the sum of local (LDA) and nonlocal (vdW-DF) energies in order to avoid double counting. The dispersion energy is included in the nonlocal correlation energy given by a doubly spatial integral of the electron density $\rho(\mathbf{r})$ and the integration kernel $\varphi(\mathbf{r}_1, \mathbf{r}_2)$. The straightforward integration of Eq. (1.6) requires a higher computational cost than GGAs or hybrid functional. Román-Pérez and Soler reduced the computational cost of vdW-DF by an efficient implementation [7]. Another approach to reduce computational cost is avoiding the doubly integral by the expansion of the nonlocal correlation energy. The LRD method [8,9] is based on this idea as explained in the next section, enabling density-dependent dispersion correction with low computational cost.

Finally, we mention the approach dependent on virtual orbitals. In the context of DFT, orbitals can be used to calculate the correlation energy according to the adiabatic-connection fluctuation dissipation theorem [10]. The particular approach which has received attention recently is the RPA [11,12]. Although results have been encouraging, RPA shares with the post-HF methods a high computational cost (approximately proportional to the fourth power of the system size) and slow convergence with respect to basis set size.

In summary, the properties of individual dispersion correction method are compared in Table 1.1. The LRD method is found to be a well-balanced approach in terms of reliability and efficiency.

Table 1.1. Properties of the dispersion correction methods for DFT.

	Reference for C_6	C_6 depend on	Additional cost	Ref.
DFT-D2	various	constant	negligible	[2]
DFT-D3	TDDFT	geometry	negligible	[4]
XDM	polarizabilities	atomic volume, exchange hole	≈ hybrid DFT	[5]
LRD	C_6 calculated	density	small	[8,9]
vdW-DF	C_6 calculated	density	≈ 50 % of GGA	[7]
RPA	none	orbitals	large	[11,12]

1.2. Local response dispersion method

This section explains the LRD method formulated by Sato and Nakai [8,9]. Let us begin with the second-order dispersion energy expression between isolated (distinguishable) molecules *A* and *B* in the ground-state [13],

$$E_{\mathrm{disp}}[A\cdots B] = -\sum_{m}^{A}\sum_{n}^{B}\frac{\left|\left\langle m^{A}n^{B}\left|\hat{V}_{AB}\right|0^{A}0^{B}\right\rangle\right|^{2}}{\omega_{m}^{A}+\omega_{n}^{B}}, \tag{1.7}$$

where $\hat{V}_{AB}$ is the electrostatic interaction operator between molecules *A* and *B*, $\left|0^{A}\right\rangle$ and $\left|m^{A}\right\rangle$ are the ground and the *m*th excited states of the molecule *A*, and ω_{m}^{A} is the corresponding excitation energy, with similarly defined quantities for *B*. The atomic units are used throughout in this section. Applying the following integral transformation:

$$\frac{1}{a+b} = \frac{2}{\pi}\int_{0}^{\infty}\frac{a}{a^{2}+u^{2}}\frac{b}{b^{2}+u^{2}}\mathrm{d}u, \tag{1.8}$$

Eq. (1.7) is equivalently expressed as

$$E_{\mathrm{disp}}[A\cdots B] = -\frac{1}{2\pi}\int \mathrm{d}\mathbf{r}_{1}\mathrm{d}\mathbf{r}_{1}'\mathrm{d}\mathbf{r}_{2}\mathrm{d}\mathbf{r}_{2}'\int_{0}^{\infty}\mathrm{d}u\,\frac{\chi^{A}(\mathbf{r}_{1},\mathbf{r}_{1}',\mathrm{i}u)\chi^{B}(\mathbf{r}_{2},\mathbf{r}_{2}',\mathrm{i}u)}{\left|\mathbf{r}_{1}-\mathbf{r}_{2}\right|\cdot\left|\mathbf{r}_{1}'-\mathbf{r}_{2}'\right|}, \tag{1.9}$$

in terms of the dynamic density response functions χ^{A} and χ^{B} defined by

$$\chi^{A}(\mathbf{r},\mathbf{r}',\omega) = 2\sum_{m}^{A}\frac{\omega_{m}^{A}}{(\omega_{m}^{A})^{2}-\omega^{2}}\left\langle 0^{A}\left|\hat{\rho}^{A}(\mathbf{r})\right|m^{A}\right\rangle\left\langle m^{A}\left|\hat{\rho}^{A}(\mathbf{r}')\right|0^{A}\right\rangle, \tag{1.10}$$

with *B* analogs, where $\hat{\rho}(\mathbf{r}) = \sum_{i}^{A}\delta^{3}(\mathbf{r}_{i}-\mathbf{r})$ is the density operator.

A key to separate variables of integration is a multicenter multipole expansion of the intermolecular Coulomb operator. A molecular volume has to be divided or

distributed into constituent atoms. For this purpose, the atomic partition function $w_a(\mathbf{r})$ is introduced. Thus, Coulomb interaction between electrons at $\mathbf{r}_1$ in molecule A and $\mathbf{r}_2$ in molecule B leads

$$\frac{1}{|\mathbf{r}_1-\mathbf{r}_2|}=\sum_a^{\mathrm{A}}\sum_b^{\mathrm{B}}\frac{w_a(\mathbf{r}_1)w_b(\mathbf{r}_2)}{|\mathbf{r}_1-\mathbf{r}_2|}=\sum_a^{\mathrm{A}}\sum_b^{\mathrm{B}}\frac{w_a(\mathbf{r}_1)w_b(\mathbf{r}_2)}{|\mathbf{R}_{ab}-\mathbf{r}_{a1}-\mathbf{r}_{b2}|}, \tag{1.11}$$

where the normalization condition $\sum_a^A w_a(\mathbf{r})=1$ is inserted. Vectors are written using $\mathbf{R}_{ab} = \mathbf{R}_b - \mathbf{R}_a$, $\mathbf{r}_{a1} = \mathbf{r}_1 - \mathbf{R}_a$, and $\mathbf{r}_{b2} = \mathbf{r}_2 - \mathbf{R}_b$, with $\mathbf{R}_a$ and $\mathbf{R}_b$ being position vectors of atoms a and b. Here and in the following, labels a and b are used for atoms belonging to molecules A and B, respectively. All vectors, multipole moments, and polarizabilities are in the space-fixed global coordinate system.

Scaled by the weight functions inside summations of Eq. (1.11), the Coulomb operator is reasonably expanded on its centers a and b. Such an expansion in terms of spherical harmonics is a well-established matter. According to the Stone's book [13],

$$\frac{1}{|\mathbf{R}_{ab}-\mathbf{r}_{a1}-\mathbf{r}_{b2}|}=\sum_{l_1=0}^{\infty}\sum_{l_2=0}^{\infty}R_{ab}^{-l_1-l_2-1}\sum_{m_1m_2}S^{ab}_{l_1m_1,l_2m_2}\times R_{l_1m_1}(\mathbf{r}_{a1})R_{l_2m_2}(\mathbf{r}_{b2}), \tag{1.12}$$

where R_{ab} is the internuclear distance. R_{lm} is the regular solid Harmonics. $S^{ab}_{l_1m_1,l_2m_2}$ is the angular factor of the multipole expansion defined by

$$S^{ab}_{l_1m_1,l_2m_2}=(-1)^{l_1}\left[\frac{(2l_1+2l_2+1)!}{(2l_1)!(2l_2)!}\right]^{1/2}\delta_{L,l_1+l_2}\times\begin{pmatrix} l_1 & l_2 & L\\ m_1 & m_2 & M\end{pmatrix}C_{L,M}(\hat{\mathbf{R}}_{ab}), \tag{1.13}$$

where the 2×3 matrix is Wigner's 3-j symbol and $C_{L,M}$ is the spherical harmonics with Racah's normalization factor evaluated at the polar angles of the unit vector $\hat{\mathbf{R}}_{ab}=\mathbf{R}_{ab}/R_{ab}$.

By expanding the Coulomb operator with distributed multipole moments centered

on each nucleus, the second-order dispersion energy between two separated molecules can be written as

$$E_{\mathrm{disp}}[A\cdots B] = -\sum_{nn'}\sum_{aa'}^{A}\sum_{bb'}^{B} R_{ab}^{-n} R_{a'b'}^{-n'} \Gamma_{nn'}^{aa',bb'}, \tag{1.14}$$

$$\Gamma_{nn'}^{aa',bb'} = \frac{1}{2\pi}\sum_{l_1l_1'l_2l_2'}\sum_{m_1m_1'm_2m_2'} S_{l_1m_1,l_2m_2}^{ab} S_{l_1'm_1',l_2'm_2'}^{a'b'} \int_0^\infty \mathrm{d}u\, \alpha_{l_1m_1,l_1'm_1'}^{aa'}(\mathrm{i}u)\, \alpha_{l_2m_2,l_2'm_2'}^{bb'}(\mathrm{i}u), \tag{1.15}$$

where $n = l_1 + l_2 + 1$. Note that the order of dispersion energy is defined as $n + n' = 6, 8, 10, \cdots$. $\alpha_{lm,l'm'}^{aa'}(\mathrm{i}u)$ is interpreted as the atomic $(a = a')$ or atomic pair $(a \neq a')$ polarizability.

$$\alpha_{lm,l'm'}^{aa'}(\mathrm{i}u) = \int \mathrm{d}\mathbf{r}\int \mathrm{d}\mathbf{r}'\, w_a(\mathbf{r}) w_{a'}(\mathbf{r}')\, \chi^A(\mathbf{r},\mathbf{r}',\mathrm{i}u)\, R_{lm}(\mathbf{r}-\mathbf{R}_a)\cdot R_{l'm'}(\mathbf{r}'-\mathbf{R}_{a'}) \tag{1.16}$$

In order to obtain a convenient expression of Eq. (1.14), the polarizabilities have to be localized. This is achieved by relying on the local response approximation to the response function [14],

$$\chi(\mathbf{r},\mathbf{r}',\omega) = \nabla\cdot\nabla'\left[\frac{\rho(\mathbf{r})}{\omega_0^2(\mathbf{r}) - \omega^2}\delta^3(\mathbf{r}-\mathbf{r}')\right], \tag{1.17}$$

where $\omega_{\mathbf{q}=0}^2$ specifies a practical approximation made for the dispersion relation. As for the LRD method, the dispersion relation proposed by Vydrov and van Voorhis [15] is adopted,

$$\omega_{\mathbf{q}=0}^2(\mathbf{r}) = \frac{q_0^2(\mathbf{r})}{3} = \frac{k_{\mathrm{F}}^2(1+\lambda s^2)^2}{3}, \tag{1.18}$$

where $k_{\mathrm{F}} = (3\pi^2\rho)^{1/3}$ is the local Fermi wave vector, $s = |\nabla\rho|/(2k_{\mathrm{F}}\rho)$ is the reduced density gradient, and λ is an empirical parameter introduced for adjusting decay of the response at the density tail. Substituting Eq. (1.17) into Eq. (1.16),

$$\alpha_{lm,l'm'}^{aa'}(\mathrm{i}u) = \int \mathrm{d}\mathbf{r}\, w_a(\mathbf{r}) w_{a'}(\mathbf{r})\, \alpha(\mathbf{r},\mathrm{i}u)\, \nabla R_{lm}(\mathbf{r}-\mathbf{R}_a)\cdot\nabla R_{l'm'}(\mathbf{r}-\mathbf{R}_{a'}) \,. \tag{1.19}$$

The polarizability density $\alpha(\mathbf{r},\mathrm{i}u)$ is given by

$$\alpha(\mathbf{r},\mathrm{i}u) = \frac{\rho(\mathbf{r})}{\omega_{\mathbf{q}=0}^2(\mathbf{r}) + u^2} \,. \tag{1.20}$$

In terms of composite variables $t,t',u,u' \in \{lm; -l \le m \le l; l \ge 1\}$, the LRD energy is finally obtained as

$$E_{\mathrm{LRD}} = -\frac{1}{2}\sum_{aa'}\sum_{tt'}\int_0^\infty \mathrm{d}u\, \alpha_{tt'}^{aa'}(\mathrm{i}u)\beta_{tt'}^{aa'}(\mathrm{i}u) \,, \tag{1.21}$$

$$\beta_{tt'}^{aa'}(\mathrm{i}u) = \sum_{bb'}\sum_{uu'} f_{tu,t'u'}^{ab,a'b'} T_{tu}^{ab} T_{t'u'}^{a'b'} \alpha_{uu'}^{bb'}(\mathrm{i}u) \,. \tag{1.22}$$

Note that the restriction with respect to aa' and bb' is removed to include the intramolecular dispersion interaction. Instead, the damping function $f_{tu,t'u'}^{ab,a'b'}$ is introduced to prevent divergence at short internuclear distances. The interaction function T_{tu}^{ab} factorizes into radial and angular parts

$$T_{l_1m_1,l_2m_2}^{ab} = \frac{1}{\sqrt{2\pi}}(1-\delta_{ab}) R_{ab}^{-l_1-l_2-1} S_{l_1m_1,l_2m_2}^{ab} \,. \tag{1.23}$$

To impose the hermiticity with single-center spatial integrals, the atomic pair polarizabilities are approximated as follows:

$$\alpha_{tt'}^{aa'}(\mathrm{i}u) = \frac{1}{2}\left\{\alpha_{tt'}^{a(a')}(\mathrm{i}u) + \alpha_{t't}^{a'(a)}(\mathrm{i}u)\right\}, \tag{1.24}$$

where $\alpha^{a(a')}$ is numerically computed with spatial mesh points $\{\mathbf{r}_i\}$ and the weights $\{w_i\}$ distributed around atom a

$$\alpha_{tt'}^{a(a')}(\mathrm{i}u) = \sum_{i\in a} w_i w_a(\mathbf{r}_i) w_{a'}(\mathbf{r}_i) \alpha(\mathbf{r}_i, \mathrm{i}u) \nabla R_t(\mathbf{r}_i - \mathbf{R}_a) \cdot \nabla R_{t'}(\mathbf{r}_i - \mathbf{R}_{a'}). \tag{1.25}$$

Becke-type [16] and Stratmann-Scuseria-Frisch [17] partition functions were practically adopted as $w_a(\mathbf{r})$ in Ref. [8] and [9], respectively.

Next, let us explain the damping function. In the LRD method, $f_{tu,t'u'}^{ab,a'b'}$ in Eq. (1.22) is given as follows:

$$f_{tu,t'u'}^{ab,a'b'} = f_{l_1 l_2}^{ab} f_{l'_1 l'_2}^{a'b'}, \tag{1.26}$$

$$f_{l_1 l_2}^{ab} = \exp\left[-\frac{l_1 + l_2 - 1}{2} \left(\frac{R_{ab}}{\overline{R}} \right)^{-6} \right], \tag{1.27}$$

where $\overline{R}$ is the damping radius. From numerical tests, three- and four-center interactions were required to reproduce asymptotic behavior while two-center interaction was sufficient to reproduce interaction energies at the equilibrium geometry. Therefore, larger radii are adopted for three- and four-center interactions, i.e.,

$$\overline{R} = \frac{\overline{R}_a + \overline{R}_{a'}}{1 + \delta_{aa'}} + \frac{\overline{R}_b + \overline{R}_{b'}}{1 + \delta_{bb'}}. \tag{1.28}$$

The interaction involving atoms aa' and bb' is damped with the sum of effective radii of the constituent atoms, estimated from the static dipole polarizabilities obtained within the local response model

$$\overline{R}_a = \kappa \left\{ \overline{\alpha}^a \right\}^{1/3} + \frac{R_0}{2}, \tag{1.29}$$

where κ and R_0 are the global constants fitted for rare-gas interactions. Here, $\overline{\alpha}^a$ is the static atomic polarizability, defined as

$$\begin{aligned}\overline{\alpha}^{a} &= \sum_{a'} \alpha^{a(a')}(\mathrm{i}\delta) \\ &= \int \mathrm{d}\mathbf{r} w_a(\mathbf{r}) \left\{ \sum_{a'} w_{a'}(\mathbf{r}) \right\} \alpha(\mathbf{r}, \mathrm{i}\delta) \\ &= \int \mathrm{d}\mathbf{r} w_a(\mathbf{r}) \alpha(\mathbf{r}, \mathrm{i}\delta), \end{aligned} \tag{1.30}$$

with the last integral approximated by numerical quadrature as in Eq. (1.25). The polarizability should be computed at a small finite frequency (0.01 a.u. in Ref. [9]) for stabilizing the integration of polarizability density given by Eq. (1.20).

References

[1] S. Grimme, *J. Comput. Chem.* **27**, 1787 (2006).

[2] Q. Wu, W. Yang, *J. Chem. Phys.* **116**, 515 (2002).

[3] S. Grimme, J. Antony, S. Ehrlich, H. Krieg, *J. Chem. Phys.* **132**, 154104 (2010).

[4] A. D. Becke, E. R. Johnson, *J. Chem. Phys.* **122**, 154104 (2005).

[5] L. A. Burns, A. Vázquez-Mayagoitia, B. G. Sumpter, D. C. Sherrill, *J. Phys. Chem.* **134**, 084107 (2011).

[6] M. Dion, H. Rydberg, E. Schröder, D. C. Langreth, B. I. Lundqvist, *Phys. Rev. Lett.* **92**, 246401 (2004).

[7] G. Román-Pérez, J. M. Soler, *Phys. Rev. Lett.* **103**, 096102 (2009).

[8] T. Sato, H. Nakai, *J. Chem. Phys.* **131**, 224104 (2009).

[9] T. Sato, H. Nakai, *J. Chem. Phys.* **133**, 194101 (2010).

[10] F. Furche, T. Van Voorhis, *J. Chem. Phys.* **122**, 164106 (2005).

[11] J. G. Ángyán, R. Liu, J. Toulouse, G. Jansen, *J. Chem. Theory Comput.* **7**, 3116 (2011).

[12] A. Hesselmann, *Phys. Rev. A* **85**, 012517 (2012).

[13] A. J. Stone, *Theory of Intermolecular Forces* (Clarendon, Oxford, 1996).

[14] J. F. Dobson, B. P. Dinte, *Phys. Rev. Lett.* **76**, 1780 (1996).

[15] O. A. Vydrov, T. Van Voorhis, *J. Chem. Phys.* **130**, 104105 (2009).

[16] A. D. Becke, *J. Chem. Phys.* **88**, 2547 (1988).

[17] R. E. Stratmann, G. E. Scuseria, M. J. Frisch, *Chem. Phys. Lett.* **257**, 213 (1996).

Chapter 2
Self-Consistent Field Treatment and Analytical Energy Gradient of Local Response Dispersion Method

2.1. Introduction

The LRD method was proposed as a density-dependent dispersion correction method with computationally efficiency [1,2]. This method is derived from the second-order perturbation energy between two isolated molecules, and based on the local response approximation to the density response function [3]. Because the LRD method calculates the dispersion coefficient using electron density and its gradient only, the numerical quadrature for conventional XC functionals is available. Small additional cost is required because the doubly numerical spatial integral is avoided by the multicenter-multipole expansion. Sato and Nakai reported the derivation, implementation, and numerical assessment based on two-center (atom-atom) interactions in the first paper of the LRD method [1]. Considering the two-center interactions was sufficient to reproduce the interaction energy of S22 benchmark set accurately [4]. In their second paper [2], multicenter interactions including three-center and four-center terms reproduced molecular C_6 coefficients and asymptotic behavior of molecular complexes.

In the previous reports, the LRD energy was added to the total DFT energy as a perturbation, namely, post-SCF approach. In other words, electron spin densities were not optimized with respect to the total energy. In addition to the XDM model [5], the nonlocal van der Waals functional such as vdW-DF [6,7], VV09 [8], and VV10 [9] were implemented self-consistently. The extension of the LRD method to fully SCF calculation is important from the theoretical point of view, because it enhances robustness and applicability.

This chapter formulates and assesses the SCF treatment by explicit derivation of dispersion potential for the LRD method. Furthermore, analytical energy gradient based on the SCF treatment is developed. The numerical assessments are also performed to compare the results between SCF and post-SCF treatments. The geometry optimizations

with the present method are also examined.

2.2. Theory

This subsection briefly reviews the LRD method. By expanding the Coulomb operator with distributed multipole moments centered on each nucleus, the second-order dispersion energy between two molecules can be written as

$$E_{\mathrm{disp}} = -\sum_{nn'}\sum_{aa'}^{A}\sum_{bb'}^{B} R_{ab}^{-n} R_{a'b'}^{-n'} \Gamma_{nn'}^{aa',bb'} , \tag{2.1}$$

where aa' and bb' run over atoms in molecules A and B, respectively. The order of dispersion energy is defined as $n+n' = 6, 8, 10, \cdots$. In terms of composite variables $t,t',u,u' \in \{lm; -l \le m \le l; l \ge 1\}$, Eq. (2.1) is rewritten as

$$E_{\mathrm{disp}} = -\frac{1}{2}\sum_{aa'}\sum_{tt'}\int_0^\infty \mathrm{d}u\, \alpha_{tt'}^{aa'}(\mathrm{i}u)\beta_{tt'}^{aa'}(\mathrm{i}u) , \tag{2.2}$$

$$\beta_{tt'}^{aa'}(\mathrm{i}u) = \sum_{bb'}\sum_{uu'} f_{tu,t'u'}^{ab,a'b'} T_{tu}^{ab} T_{t'u'}^{a'b'} \alpha_{uu'}^{bb'}(\mathrm{i}u) . \tag{2.3}$$

Note that the restriction with respect to aa' and bb' is removed to include the intramolecular dispersion interaction. The interaction function T_{tu}^{ab} factorizes into radial and angular parts,

$$T_{l_1m_1,l_2m_2}^{ab} = \frac{1}{\sqrt{2\pi}}(1-\delta_{ab}) R_{ab}^{-l_1-l_2-1} S_{l_1m_1,l_2m_2}^{ab} , \tag{2.4}$$

and the atomic pseudo-polarizabilities are defined with atomic partition functions,

$$\alpha_{lm,l'm'}^{aa'}(\mathrm{i}u) = \int \mathrm{d}\mathbf{r}\, w_a(\mathbf{r}) w_{a'}(\mathbf{r}) \alpha(\mathbf{r},\mathrm{i}u) \nabla R_{lm}(\mathbf{r}-\mathbf{R}_a)\cdot\nabla R_{l'm'}(\mathbf{r}-\mathbf{R}_{a'}) . \tag{2.5}$$

The conventional post-SCF treatment calculates the LRD energy using converged electron density obtained without the dispersion potential. Here, the dispersion potential is added to the KS Fock matrix. The SCF treatment requires the derivatives of the dispersion energy with respect to the density matrix elements. The density dependence originates from two parts; namely, the multipole polarizabilities $\alpha_{tt'}^{aa'}$ giving interaction coefficients and the effective radii used in the damping functions. In consequence, the derivatives are compactly written in terms of the polarizability derivatives,

$$\frac{\partial E_{\mathrm{LRD}}}{\partial \mathbf{P}_{\mu\nu}^{\sigma}} = -\sum_{aa'} \int_0^{\infty} \mathrm{d}u \left\{ \frac{\partial \alpha_{tt'}^{aa'}(\mathrm{i}u)}{\partial \mathbf{P}_{\mu\nu}^{\sigma}} \beta_{tt'}^{aa'}(\mathrm{i}u) + \alpha_{tt'}^{aa'}(\mathrm{i}u) \frac{\partial \overline{\alpha}^{a}}{\partial \mathbf{P}_{\mu\nu}^{\sigma}} \frac{\partial \beta_{tt'}^{aa'}(\mathrm{i}u)}{\partial \overline{\alpha}^{a}} \right\}. \tag{2.6}$$

The direct evaluation of this formula, however, faces difficulty in keeping and treating a large number of polarizability derivatives, which increase as the density matrix size and atom pair aa' become large. To make the problem tractable, the order is reversed between multipole couplings (sum over tt' and the iu integral) with the spatial integrals.

$$\frac{\partial E_{\mathrm{LRD}}}{\partial \mathbf{P}_{\mu\nu}^{\sigma}} = -\sum_{a} \int \mathrm{d}\mathbf{r}\, w_a(\mathbf{r}) \sum_{\xi} \frac{\partial \xi(\mathbf{r})}{\partial \mathbf{P}_{\mu\nu}^{\sigma}} \frac{\partial Z^{a}}{\partial \xi(\mathbf{r})}, \tag{2.7}$$

where

$$Z^{a} = \frac{1}{2} \sum_{a'} w_{a'}(\mathbf{r}) \int_0^{\infty} \mathrm{d}u\, \alpha(\mathbf{r}, \mathrm{i}u) \left\{ \nabla R_t^{(a)} \cdot \nabla R_{t'}^{(a')} \beta_{tt'}^{aa'}(\mathrm{i}u) \right\}. \tag{2.8}$$

Thus, the derivatives with respect to density variables $\xi \in \left\{ \rho_{\alpha}, \rho_{\beta}, \gamma_{\alpha\alpha}, \gamma_{\alpha\beta}, \gamma_{\beta\beta} \right\}$ become as follows:

$$\frac{\partial Z^a}{\partial \xi} = \sum_{a'} w_{a'}(\mathbf{r}) \left[\int_0^\infty \mathrm{d}u \frac{\partial \alpha(\mathbf{r}, \mathrm{i}u)}{\partial \xi} \left\{ \nabla R_t^{(a)} \cdot \nabla R_{t'}^{(a')} \beta_{tt'}^{aa'}(\mathrm{i}u) \right\} \right.$$

$$\left. + \frac{\partial \alpha(\mathbf{r}, \mathrm{i}\delta)}{\partial \xi} \left\{ \int_0^\infty \mathrm{d}u \, \alpha_{tt'}^{aa'}(\mathrm{i}u) \frac{\partial \beta_{tt'}^{aa'}(\mathrm{i}u)}{\partial \overline{\alpha}^a} \right\} \right]. \tag{2.9}$$

It should be noted that Eqs. (2.7) and (2.9) still inhibit an efficient implementation, since $\beta_{tt'}^{aa'}$ is to be at hand when working for the atomic center *a* in XC-like quadrature. $\beta_{tt'}^{aa'}$, as defined in Eq. (2.3), is obtained after completing single center spatial integrals for all atoms, by accumulating the interactions involving aa' pair. Thus, the author designed that the evaluation of Eq. (2.7) at the *n*th iteration of the SCF procedure uses $\beta_{tt'}^{aa'}$ in Eq. (2.9) computed at the (*n*-1)th iteration. The first cycle adopts null potential. This iterative scheme corresponds to the use of an approximate electronic gradient in the SCF procedure, leading to the proper solution. The SCF is expected to converge safely because of the relatively small effect of dispersion terms on the total KS potential.

Provided the SCF convergence, analytical gradient of the LRD energy with respect to nucleus *a* is formulated as follows:

$$\frac{\partial E_{\mathrm{LRD}}}{\partial \mathbf{R}_a} = -\sum_{a'} \int_0^\infty \mathrm{d}u \alpha_{tt'}^{aa'}(\mathrm{i}u) \frac{\partial \beta_{tt'}^{aa'}(\mathrm{i}u)}{\partial \mathbf{R}_a}$$

$$- \sum_{a'} \int \mathrm{d}\mathbf{r} \left\{ w_{a'}(\mathbf{r}) \sum_{\xi} \frac{\partial \xi(\mathbf{r})}{\partial \mathbf{R}_a} \frac{\partial Z^{a'}}{\partial \xi(\mathbf{r})} + 2 \frac{\partial w_{a'}(\mathbf{r})}{\partial \mathbf{R}_a} Z^{a'} \right\}. \tag{2.10}$$

The first term is an explicit differentiation of the interaction function and damping function with respect to nuclear coordinates. The other two terms are derived in analogy with the analytical gradient of conventional XC functionals [10]. The former is a differentiation with respect to density-dependent terms, which is easily derived from the dispersion potential. The latter arises since the partition function depends on the nuclear configuration and hence has a nonzero gradient with respect to nuclear displacements.

2.3. Implementation

The LRD method described above was implemented into Gaussian 09 package [11], both as post-SCF and SCF procedures. The present code can afford full inclusions of up to tenth order interactions and partially account for up to 14th interactions. Because of minor numerical impact, the different rank of polarizabilities are excluded, i.e., $l = l'$ in Eq. (2.5). Furthermore, the tenth order dipole-octapole $\{l_1, l_2\} = \{1, 3\}, \{3, 1\}$ and higher order interactions are truncated. In the numerical assessment, the LRD energy was calculated considering sixth, eighth, and tenth order two-center and sixth order multicenter interactions. Becke-type atomic partition function without atomic-size adjustments [12], which is the default in the Gaussian program, was adopted. The imaginary frequency integrals in Eqs. (2.2), (2.9), and (2.10) were approximated by ten-point Gauss-Chebyshev quadrature. Because the variable u was changed to $t = u/\sqrt{1+u^2}$ and the integrand is an even function, the domain of these integrals [0, ∞) can be transformed into [-1, 1] to apply the quadrature.

2.4. Numerical assessment

2.4.1. Computational details

LC [13] Becke-88 [14] with one-parameter progressive correlation [15] functional was adopted in all calculations. The range separation parameter μ for LC was 0.47. In the LRD calculation, the dielectric model parameter and the damping parameters were taken from the previous work [2]: $\lambda = 0.232$, $\kappa = 0.600$, and $R_0 = 3.22$ in atomic units, respectively. The 6-311++G(3df,3pd) [16-18] and 6-31++G(d,p) [18,19] basis sets were adopted in the assessment of the SCF treatment and geometry optimization, respectively.

2.4.2. SCF treatment

First, the SCF effect is discussed from the viewpoint of energy, charge, and computational cost. Table 2.1 shows total and LRD energies of the S22 benchmark set [4] obtained by the post-SCF and SCF procedures. Geometries were taken from the literature [5]. Comparing with the post-SCF results, the SCF treatment gives lower total energies. However, the energy differences are extremely small: two orders of magnitude less than the dispersion energies. Similar trend of the SCF effect has been reported in the XDM model [5]. It is interesting that the variations of the LRD energies by the SCF treatment are approximately twice of those of the total energies.

Table 2.1. Total energies E_{tot} and LRD energies E_{LRD} of the S22 benchmark set by the post-SCF and SCF procedures (in Hartree).

	E_{tot}			E_{LRD}		
	Post-SCF	SCF		Post-SCF	SCF	
Ammonia dimer	–112.884537	–112.884538	(–0.549)	–0.000828	–0.000829	(–1.093)
Water dimer	–152.632075	–152.632076	(–0.242)	–0.000572	–0.000572	(–0.480)
Formicacid dimer	–378.886820	–378.886821	(–0.814)	–0.002593	–0.002595	(–1.621)
Formamide dimer	–339.144172	–339.144173	(–1.690)	–0.003130	–0.003134	(–3.372)
Uracil dimer	–827.924080	–827.924087	(-6.845)	–0.010871	–0.010884	(–13.688)
2-pyridoxine-2-aminopyridine	-625.645677	-625.645689	(–12.428)	–0.011500	–0.011524	(–24.902)
Adenine-thymine WC complex	–919.405776	–919.405792	(–16.582)	–0.015710	–0.015743	(–33.211)
Methane dimer	–80.790741	–80.790744	(–2.938)	–0.001255	–0.001261	(–5.882)
Ethene dimer	–156.715767	–156.715770	(–2.819)	–0.003028	–0.003034	(–5.626)
Benzene-methane	–271.976314	–271.976324	(–10.014)	–0.006430	–0.006450	(–20.037)
PD-benzene dimer	–463.162120	–463.162175	(–54.941)	–0.015066	–0.015177	(–110.750)
Pyrazine dimer	–527.294513	–527.294554	(–41.174)	–0.013089	–0.013172	(–82.920)
Stacked uracil dimer	–827.909548	–827.909591	(–43.478)	–0.018401	–0.018488	(–87.407)
Stacked indole-benzene	–594.414319	–594.414407	(–87.951)	–0.021240	–0.021418	(–177.535)
Stacked adenine-thymine	–919.400162	–919.400251	(–88.641)	–0.027188	–0.027367	(–178.646)
Ethene-ethyne	–155.465162	–155.465166	(–3.516)	–0.001999	–0.002006	(–7.030)
Benzene-water	–307.896338	–307.896348	(–10.049)	–0.006267	–0.006287	(–20.133)
Benzene-ammonia	–288.022638	–288.022648	(–10.672)	–0.006397	–0.006419	(–21.376)
Benzene-hydrogen cyanide	–324.784386	–324.784393	(–7.544)	–0.006447	–0.006462	(–15.106)
T-shaped benzene dimer	–463.161707	–463.161727	(–20.186)	–0.011564	–0.011604	(–40.549)
T-shaped indole-benzene	–594.415077	–594.415109	(–31.259)	–0.015692	–0.015755	(–62.785)
Phenol dimer	–613.401627	–613.401647	(–20.210)	–0.013145	–0.013185	(–40.535)

* Differences of two schemes are shown in parentheses (in μHartree).

Table 2.2 shows the CPU times and the number of SCF iterations. The CPU times are extremely close to each other. The SCF iterations are equal except for benzene-methane, even in which the difference is one iteration. The results in Tables 2.1 and 2.2 confirm that the SCF treatment does not lead to large variations of the energy and computational cost.

Table 2.2. Total CPU time T_{SCF} and SCF interactions N_{SCF} for the single-point calculation of the S22 benchmark set by the post-SCF and SCF procedures of the LRD method.

	T_{SCF}		N_{SCF}	
	Post-SCF	SCF	Post-SCF	SCF
Ammonia dimer	0:01:16	0:01:16	10	10
Water dimer	0:00:46	0:00:44	10	10
Formicacid dimer	0:06:31	0:06:16	11	11
Formamide dimer	0:09:53	0:09:31	12	12
Uracil dimer	2:34:22	2:26:11	15	15
2-pyridoxine-2-aminopyridine	2:49:16	2:35:48	16	16
Adenine-thymine WC complex	4:41:05	4:18:23	15	15
Methane dimer	0:01:56	0:01:53	9	9
Ethene dimer	0:05:14	0:05:22	9	9
Benzene-methane	0:23:33	0:26:02	10	11
PD-benzene dimer	2:03:23	1:54:51	12	12
Pyrazine dimer	1:26:34	1:22:44	13	13
Stacked uracil dimer	3:20:53	3:06:15	15	15
Stacked indole-benzene	4:19:28	4:07:33	15	15
Stacked adenine-thymine	6:40:51	6:29:10	16	16
Ethene-ethyne	0:03:34	0:03:25	11	11
Benzene-water	0:21:57	0:21:24	12	12
Benzene-ammonia	0:25:16	0:24:50	12	12
Benzene-hydrogen cyanide	0:26:21	0:24:27	12	12
T-shaped benzene dimer	1:44:57	1:49:52	12	12
T-shaped indole-benzene	3:28:14	3:29:35	14	14
Phenol dimer	2:33:04	2:37:10	14	14

* T_{SCF} is shown in hours:minutes:seconds.

** X5680 (3.33GHz) processor on a single core was used.

Table 2.3. Mulliken charges calculated by the post-SCF and SCF procedures of the LRD method.

		Post-SCF	SCF	
Water dimer	O_a	–0.9309	–0.9312	(–0.0002)
	H_a	0.4088	0.4086	(–0.0002)
	H_b	0.5546	0.5551	(0.0006)
	O_b	–0.9756	–0.9748	(0.0007)
	H_c	0.4716	0.4711	(–0.0004)
Benzene-methane	C_a	–0.0649	–0.0644	(0.0005)
	C_b	–0.0557	–0.0552	(0.0005)
	H_a	0.0511	0.0507	(–0.0004)
	H_b	0.0521	0.0518	(–0.0003)
	C_c	–0.4483	–0.4428	(0.0055)
	H_c	0.0399	0.0404	(0.0005)
	H_d	0.3807	0.3730	(–0.0077)
PD-benzene dimer	C_a	0.5151	0.4876	(–0.0275)
	C_b	–0.0783	–0.0780	(0.0003)
	C_c	–0.1982	–0.1927	(0.0056)
	C_d	–0.2010	–0.1833	(0.0177)
	H_a	0.0283	0.0288	(0.0004)
	H_b	0.0251	0.0246	(–0.0005)
	H_c	0.0520	0.0514	(–0.0006)
	H_d	0.0565	0.0563	(–0.0002)
Benzene-water	C_a	–0.0282	–0.0288	(–0.0006)
	C_b	–0.0622	–0.0615	(0.0007)
	C_c	–0.1962	–0.1937	(0.0025)
	C_d	–0.0622	–0.0615	(0.0007)
	H_a	0.0553	0.0552	(–0.0001)
	H_b	0.0563	0.0564	(0.0001)
	H_c	0.0571	0.0572	(0.0001)
	H_d	0.0580	0.0577	(–0.0003)
	O	–0.9692	–0.9658	(0.0034)
	H_e	0.4180	0.4175	(–0.0005)
	H_f	0.6268	0.6226	(–0.0042)

* Differences of two schemes are shown in parentheses.

Next, let us examine the SCF effect on the electronic structure. Table 2.3 shows Mulliken atomic charges obtained by the post-SCF and SCF calculations for four complexes in the S22 set: water dimer, benzene-methane, PD benzene dimer, and benzene-water as representatives of hydrogen-bonded, C-H/π interacted, π/π stacked, and O-H/π interacted systems, respectively. Geometries and atomic labeling for symmetry-unique atoms are shown in Figure 2.1. For most of atoms, the difference is small as expected, less than 10^{-3}. However, some atomic charges are obviously changed by introducing the dispersion potential. In terms of the absolute value, atomic charges of C and H_d in the benzene-methane and those of O and H_f in the benzene-water decrease more than 3×10^{-3}. In the PD-benzene dimer, atomic charges of C_a and C_d changes more than 10^{-2}.

For more detailed analysis, Figure 2.2 describes the density difference maps of the benzene-methane, PD-benzene dimer, and benzene-water. Here, blue and red areas indicate increases and decreases in densities, respectively. Obviously, the intramolecular electron density decreases, and intermolecular one increases in all systems. As for the benzene-methane and benzene-water complexes, the electron density increases around the hydrogen atom faced to the aromatic ring, which decreases the positive value of Mulliken charge. The PD-benzene dimer has greatly density-increasing area, which is consistent with the relatively large change of Mulliken charge. The diffused electron may contribute to the increase of atomic polarizability and dispersion correction energy. In contrast, the intermolecular electron density may destabilize the electrostatic interaction. Thus a clear trend was found, i.e., the electron redistribution from molecules to intermolecular spaces while atomic charges do not change significantly.

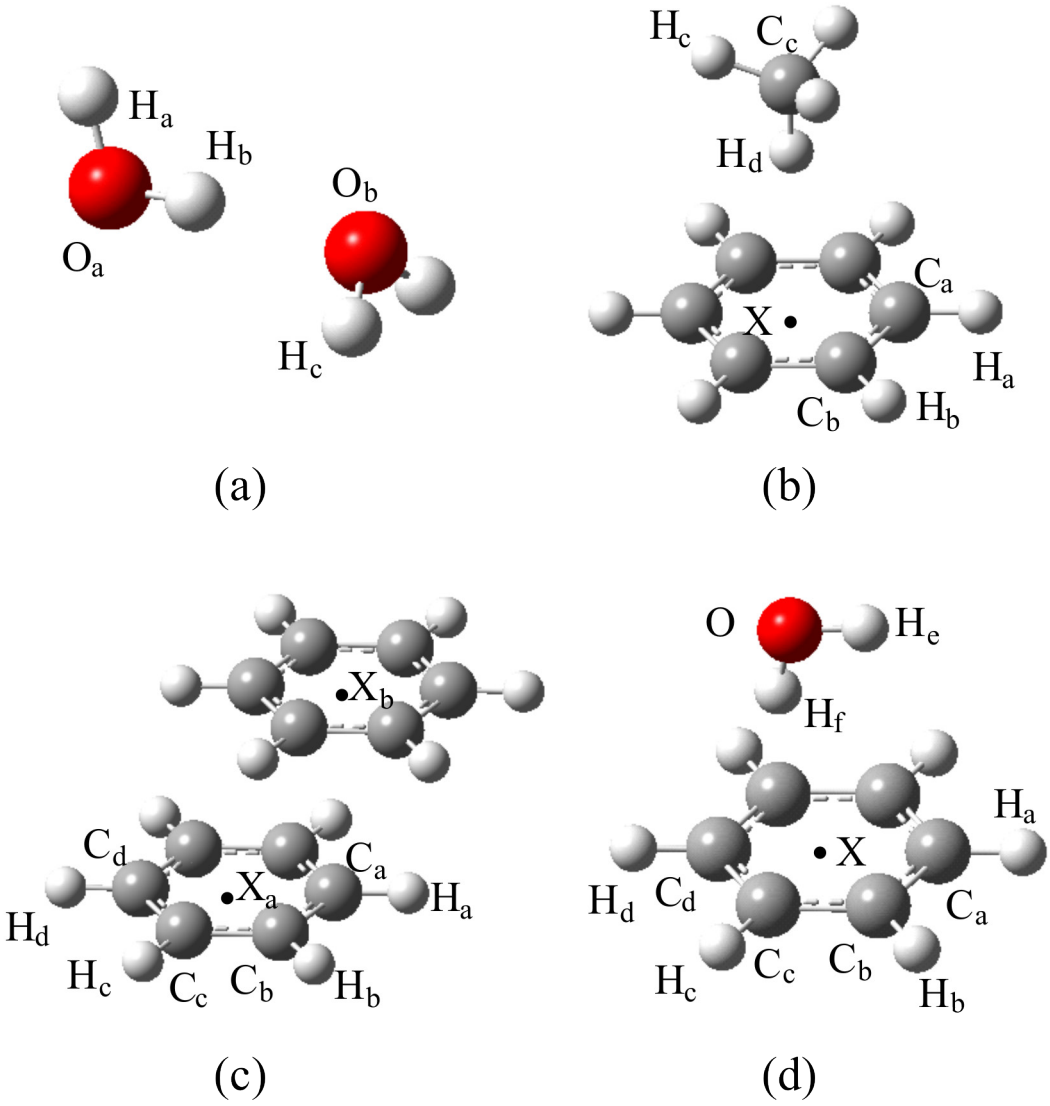

Figure 2.1. Geometries and labeling of (a) water dimer (C_s), (b) benzene-methane complex (C_3), (c) PD-benzene dimer (C_{2h}), and (d) benzene-water complex (C_s).

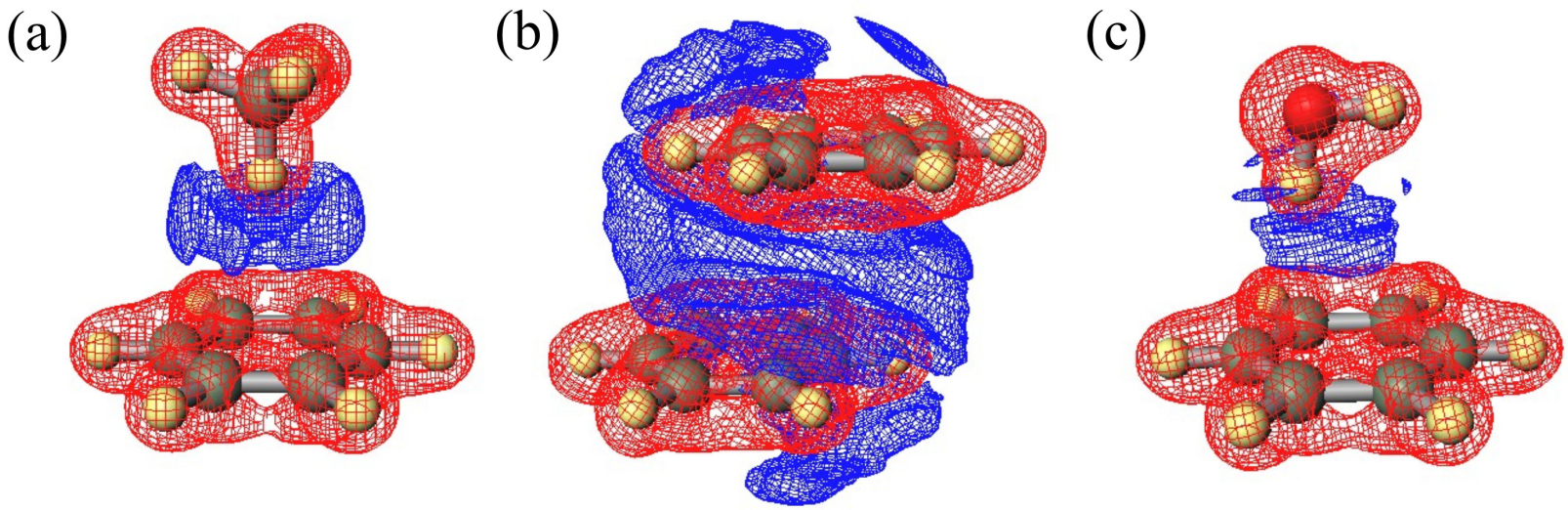

Figure 2.2. Density difference maps for (a) benzene-methane complex, (b) PD- benzene dimer, and (c) benzene-water complex. The maps are obtained by subtracting post-SCF electron density from SCF one. The iso-surfaces are taken at the values +0.00002 electron/Å^3 (blue) and −0.00002 electron/Å^3 (red).

2.4.3. Analytical energy gradient

Now, let us discuss the geometry optimization. Table 2.4 summarizes the optimized intermolecular geometric parameters of the same complexes considered in Table 2.3.

Table 2.4. Optimized geometric parameters obtained with and without the LRD method.

	LC-BOP		LC-BOP+LRD		Ref.
Water dimer					
$R(H_bO_b)$	1.900	(–0.052)	1.899	(–0.052)	1.952
$R(O_aO_b)$	2.866	(–0.044)	2.866	(–0.044)	2.910
$\theta(O_aH_bO_b)$	173.3	(0.5)	173.4	(0.6)	172.8
$\varphi(O_aH_bO_bH_c)$	61.9	(5.1)	61.8	(5.0)	56.8
Benzene-methane					
$R(XH_d)$	3.969	(1.339)	2.750	(0.120)	2.630
$R(XC_c)$	4.196	(0.480)	3.840	(0.124)	3.716
$\varphi(C_aXC_cH_c)$	174.3	(0.7)	173.5	(0.0)	173.5
PD-benzene dimer					
$R(X_aX_b)$	5.939	(2.174)	3.924	(0.159)	3.765
$R(C_aX_b)$	4.841	(1.467)	3.461	(0.087)	3.374
$\theta(C_aX_aX_b)$	33.3	(–29.9)	60.6	(–2.6)	63.2
Benzene-water					
$R(XH_f)$	2.673	(0.142)	2.519	(–0.012)	2.531
$R(XO)$	3.529	(0.093)	3.384	(–0.051)	3.436
$\theta(XH_fO)$	148.0	(–8.6)	149.3	(–7.3)	156.6
$\theta(XH_eO)$	82.0	(3.7)	80.4	(2.1)	78.3

* Units of distance R, angle θ, and dihedral φ are Å, deg, and deg, respectively.

** Deviations from reference values are shown in parentheses.

Here, X designates the center of an aromatic ring as shown in Figure 2.1. Reference geometries are taken from the S22 benchmark set [4], in which water dimer was optimized at the CCSD(T)/cc-pVQZ level, and the others were optimized at the CP-corrected MP2/cc-pVTZ level. Although MP2 is occasionally inaccurate to estimate

interaction energy especially in dispersion-dominated complexes, it well reproduces the CCSD(T) geometry according to the investigation about the geometry optimization of molecular complexes by Hobza *et al.* [20]. The LRD method does not change the geometry of the water dimer considerably. In the case of the benzene-methane complex and the PD-benzene dimer, the deviations of all geometric parameters from the reference are dramatically decreased by including the LRD contribution. As for the benzene-water complex, the deviations of the geometric parameters still remain to some extent in spite of a great improvement from the LC-BOP case. In conclusion, the analytic gradient of the LRD method becomes more important as the dispersion contribution increases.

2.5. Conclusion

This chapter has treated the SCF procedure based on the dispersion potential from the LRD method. The efficient scheme to evaluate the atomic pseudo-polarizability, which is required for the dispersion potential, was achieved by the iterative procedure. In analogy with conventional XC functionals, the analytic gradient of the LRD method was derived from the differentiation with respect to density in the dispersion potential.

The SCF effect on the energy and electronic structure was numerically assessed. The variations of LRD and total energies were considerably small comparing between the post-SCF and SCF treatments. Although atomic charges do not change significantly, the electron redistribution from intramolecules to intermolecular spaces was clearly observed. The efficiency, namely, SCF iterations and CPU times were extremely close to each other with and without dispersion potential in the SCF procedure. The geometry optimizations for weakly interacting systems were also examined. The LRD method greatly improved the intermolecular geometric parameters, especially for the dispersion-dominated complexes.

References

[1] T. Sato, H. Nakai, *J. Chem. Phys.* **131**, 224104 (2009).

[2] T. Sato, H. Nakai, *J. Chem. Phys.* **133**, 194101 (2010).

[3] J. F. Dobson, B. P. Dinte, *Phys. Rev. Lett.* **76**, 1780 (1996).

[4] P. Jurečka, J. Sponer, J. Černý, P. Hobza, *Phys. Chem. Chem. Phys.* **8**, 1985 (2006).

[5] J. Kong, Z. Gan, E. Proynov, M. Freindorf, T. R. Furlani, *Phys. Rev. A* **79**, 042510 (2009).

[6] T. Thonhauser, V. R. Cooper; S. Li, A. Puzder, P. Hyldgarrd, D. C. Langreth, *Phys. Rev. B* **76**, 125112 (2007).

[7] O. A. Vydrov, Q. Wu, T. Van Voorhis, *J. Chem. Phys.* **129**, 014106 (2008).

[8] O. A. Vydrov, T. Van Voorhis, *J. Chem. Phys.* **132**, 164113 (2010).

[9] O. A. Vydrov, T. Van Voorhis, *J. Chem. Phys.* **133**, 244103 (2010).

[10] B. G. Johnson, P. M. W. Gill, J. A. Pople, *J. Chem. Phys.* **98**, 5612 (1993).

[11] M. J. Frisch *et al*., Gaussian 09, Revision A.02, Gaussian, Inc, Wallingford, CT, 2009.

[12] R. E. Stratmann, G. E. Scuseria, M. J. Frisch, *Chem. Phys. Lett.* **257**, 213 (1996).

[13] H. Iikura, T. Tsuneda, T. Yanai, K. Hirao, *J. Chem. Phys.* **115**, 3540 (2001).

[14] A. D. Becke, *Phys. Rev. A* **38**, 3098 (1988).

[15] T. Tsuneda, T. Suzumura, K. Hirao, *J. Chem. Phys.* **110**, 10664 (1999).

[16] R. Krishnan, J. S. Binkley, R. Seeger, J. A. Pople, *J. Chem. Phys.* **72**, 650 (1980).

[17] M. J. Frisch, J. A. Pople, J. S. Binkley, *J. Chem. Phys.* **80**, 3265 (1984).

[18] T. Clark, J. Chandrasekhar, G. W. Spitznagel, P. V. R. Schleyer, *J. Comput. Chem.* **4**, 294 (1983).

[19] P. C. Hariharan, J. A. Pople, *Theor. Chim. Acta* **28**, 213 (1973).

[20] J. Černý, M. Pitoňák, K. E. Riley, P. Hobza, *J. Chem. Theory Comput.* **7**, 3924 (2011).

Chapter 3
Local response Dispersion Method for Open-Shell Systems

3.1. Introduction

The LRD method [1,2] has been developed as one of the dispersion correction methods for DFT. Similar to the nonlocal correlation functionals, this method computes dispersion correction energy non-empirically. Additional computational cost is low because of the local response approximation to the density response function [3] and the multicenter-multipole expansion of the Coulomb operator. The LRD method realized accurate calculation of interaction energy [1,2] and potential energy curve [2]. In addition to dispersion-dominated systems, numerical assessments in hydrogen-bonded systems [1,2] and charge-transfer complexes [4] also provided satisfactory results.

While all of these assessments were performed for closed-shell systems, a number of studies regarding open-shell intermolecular interactions have been reported. For example, open-shell van der Waals complexes have been theoretically studied from the viewpoint of precursor or intermediate of chemical reactions [5]. The intermolecular interaction between stable organic radicals that have delocalized SOMOs has also attracted attention [6]. However, the applicability of the LRD method to such systems is not obvious, because the effect of spin polarization is neglected.

The purpose of this chapter is to investigate the performance of the LRD method in open-shell systems. First, the dispersion coefficient of atoms and the atomic polarizability in carbon compounds are discussed. Then, interaction energies and magnetic coupling constants of open-shell complexes are calculated using the LRD method and the LC exchange functional.

3.2. Numerical assessment

3.2.1. Atomic dispersion coefficient and polarizability

First, the C_6 dispersion coefficients of open-shell atoms and atomic polarizabilities of carbon compounds were computed. LC [7] Becke-88 exchange [8] with one-parameter progressive correlation [9] functional (LC-BOP) was adopted to generate electron density. The range separation parameter μ for the LC scheme was 0.47. The HF density was used only for hydrogen because of no XC interaction. The dielectric model parameter of the LRD method was 0.232 au [2]. The GAMESS program package [10] was utilized for all calculations in this subsection.

The sixth-order dispersion coefficient between molecules A and B is given by

$$C_6^{AB} = \frac{3}{2\pi}\int_0^\infty \mathrm{d}u\,\alpha^A(\mathrm{i}u)\alpha^B(\mathrm{i}u), \tag{3.1}$$

where $\alpha^A(\mathrm{i}u)$ is the dynamic dipole polarizability of the molecule A. If A and B designate an identical atom, the LRD method gives the polarizability as follows:

$$\alpha^A(\mathrm{i}u) = \int \mathrm{d}\mathbf{r}\,\frac{\rho(\mathbf{r})}{\omega_{\mathbf{q}=0}^2(\mathbf{r}) + u^2}. \tag{3.2}$$

Table 3.1 summarizes C_6^{AA} coefficients of open-shell atoms estimated by the LRD method and the VV09 model [11]. The dispersion coefficients of alkali metals and gallium are severely underestimated. As for the LRD method, the dispersion coefficient of hydrogen, which is regarded as a completely spin-polarized system, is overestimated. Though MAPD from Ref. [12-14] is larger than previously reported error of C_6 coefficients by the LRD method for closed-shell molecules (6.0%) [2], the present treatment resulted in smaller MAPD than the VV09 model. Correlation between the spin multiplicity of atoms and percentage deviation of the dispersion coefficient is not confirmed. This result implies that the density dependency of the polarizability model is more important than the spin dependency for the accuracy of dispersion coefficients.

Table 3.1. C_6^{AA} coefficients of open-shell atoms estimated using the aug-cc-pVQZ basis set.

	Spin multiplicity	C_6^{AA} coefficient (a.u.)				
		LRD		VV09[a]		Ref.
N	4	26.07	(8.2)	27.65	(14.7)	24.10[b]
P	4	212	(14.4)	179	(−3.2)	185[c]
As	4	258	(4.8)	222	(−9.8)	246[c]
C	3	50.8	(9.1)	47.0	(0.9)	46.6[c]
O	3	15.77	(5.9)	18.19	(22.2)	14.89[b]
Si	3	342	(12.2)	253	(−17.0)	305[c]
S	3	137	(2.1)	130	(−3.0)	134[c]
Ge	3	321	(−9.2)	251	(−29.1)	354[c]
Se	3	201	(−4.2)	190	(−9.5)	210[c]
H	2	8.03	(23.6)	6.75	(3.8)	6.50[d]
Li	2	1100	(−20.8)	565	(−59.3)	1389[d]
B	2	112.6	(13.2)	87.6	(−12.0)	99.5[c]
F	2	9.72	(2.1)	12.21	(28.3)	9.52[c]
Na	2	1037	(−33.3)	669	(−57.0)	1556[d]
Al	2	545	(3.2)	353	(−33.1)	528[c]
Cl	2	89.3	(−5.6)	94.7	(0.1)	94.6[c]
Ga	2	350	(−29.8)	255	(−48.8)	498[c]
Br	2	153	(−5.6)	158	(−2.5)	162[c]
MPE (%)			(−0.6)		(−11.9)	
MAPE (%)			(11.5)		(19.7)	

* Percentage errors are shown in parentheses.
[a] Ref. [11]. [b] Ref. [12]. [c] Ref. [13]. [d] Ref. [14].

Table 3.2 shows static dipole polarizabilities of carbon atoms in several compounds. Note that the static atomic polarizability was calculated using Eq. (1.30). Though the aug-cc-pVQZ basis set provided larger values, both basis sets resulted in the same tendency. All polarizabilities of carbon in molecules are smaller than that of the free atom. Methane takes the smallest value due to the electron localization, in other words, lack of π electron. Carbon atoms belonging to CO and CN have larger polarizabilities than in the other molecules. This may be originated in the negative charge and unpaired electron at the carbon atoms. The carbon atoms in phenalenyl radical, which is known as a stable hydrocarbon radical illustrated in Figure 3.1, have four different polarizabilities because of different chemical environment. These values decrease in the order of C_a, C_b, C_c, and C_d, approaching to the polarizability of benzene. This is

interpreted as the larger electronic delocalization of the central carbon atom than that of outer ones. Thus, the atomic polarizability was found to reasonably reflect the electron distribution even in the case of spin-polarized systems.

Table 3.2. Static atomic polarizabilities of carbon atom estimated by Eq. (1.30).

	Spin multiplicity	Polarizability (a.u.)	
		6-31G(d,p)	Aug-cc-pVQZ
C (atom)	3	10.31	11.91
CN	2	8.14	8.79
C_a (Phenalenyl)	2	7.43	7.66 [a]
C_b (Phenalenyl)	2	7.34	7.66 [a]
C_c (Phenalenyl)	2	6.67	7.06 [a]
C_d (Phenalenyl)	2	6.57	6.99 [a]
CO	1	8.06	9.32
Benzene	1	6.57	6.99
Methane	1	3.56	3.63

[a] Calculated using the cc-pVQZ basis set.

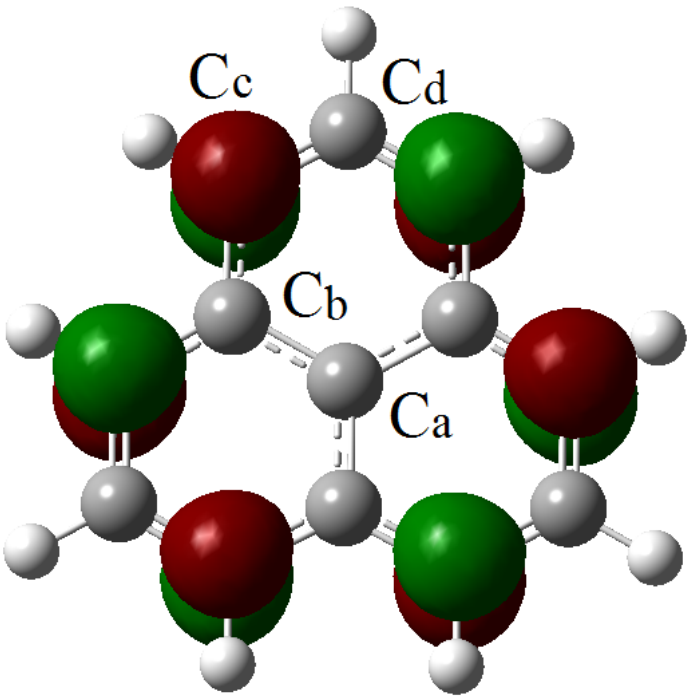

Figure 3.1. SOMO of phenalenyl radical by the LC-UBOP/6-31G(d,p) calculation.

3.2.2. Open-shell van der Waals complexes

Next, interaction energies and equilibrium geometries of open-shell van der Waals complexes are investigated using the LRD method combined with the LC-BOP functional. The summation of the LRD energy is truncated up to tenth order. The damping parameters were taken from the previous work [2], i.e., $\kappa = 0.600$ au and $R_0 = 3.22$ bohr. In the calculation of interaction energies, the BSSE was corrected by the CP method [15]. Hereafter, all calculations were performed in the unrestricted manner using the modified Gaussian 09 package [16].

The geometries were taken from Refs. [17-23]. For comparison, unrestricted DFT calculations on the basis of ωB97X-D [24] and M06-2X [25] functionals, which are highly parameterized to reproduce thermodynamic properties as well as noncovalent interactions, were also performed besides the UMP2 calculation. Here, the accuracy of these methods for closed-shell intermolecular interactions are denoted: MADs of the S22 benchmark set by LC-BOP+LRD, ωB97X-D, M06-2X, and MP2 are 0.29 [2], 0.22 [24], 0.40 [26], and 0.98 [26] in kcal/mol, respectively. The (99,590) and (75,302) grids were used for the M06-2X functional and the other XC functionals, respectively. The aug-cc-pVTZ basis set was adopted for UDFT and UMP2 calculations.

The interaction energy and its deviation from the reference, MD, and MAD are summarized in Table 3.3. The complexes are arranged with respect to interaction energies. As expected, the LC-BOP functional without dispersion correction failed to reproduce the interaction energy. In particular, the opposite sign was obtained in the five weakest complexes, i.e., $O_2\cdots O_2$, NO···Ar, CN···Ne, OH···He, and NH···He. The application of the LRD method significantly reduced the deviations. The ωB97X-D functional underestimated the interaction in all complexes, although it is highly accurate for the S22 benchmark set. The empirical dispersion correction (-D) may contribute to the underestimation because it cannot treat the increase of dispersion coefficients in open-shell systems. The M06-2X functional overestimated the interaction of the three weakest complexes. The complexes including helium or neon, i.e., CN···Ne, OH···He, and NH···He are difficult systems due to the small reference interaction energies less than 50 cm^{-1}. The performance of the UMP2 method for them was moderate compared

to DFT. However, it severely underestimated interaction energies of $HO_2\cdots H_2O$, $NO\cdots H_2O$, and $NO\cdots Ar$, indicating numerical instability of the perturbative approach. Overall, the MD and MAD of the LC-BOP+LRD method are smaller than those of the other approaches.

The optimized intermolecular geometric parameters of open-shell van der Waals complexes are summarized in Table 3.4. Note that all reference geometries correspond to global minimums of potential energy surfaces. Since $OH\cdots CO$, $NH\cdots NH$, $OH\cdots N_2$, and $SH\cdots N_2$ have linear geometries [17,18], only noncovalent bond distances are summarized. The global minimum of $O_2\cdots O_2$ has X-shaped geometry [21]. The geometric parameters of the other complexes [17,19,23] are defined in Figure 3.2, where X designates the center of mass of a diatomic radical. The LRD method scarcely changed the noncovalent bond lengths in the electrostatically stabilized systems. For more weakly bound complexes such as $NO\cdots H_2O$ and $SH\cdots N_2$, the LRD method improved the equilibrium geometries. In the case of dispersion-dominated complexes such as $O_2\cdots O_2$, $OH\cdots He$, and $NH\cdots He$, the LRD method significantly reduced the deviations of intermolecular distances. From Tables 3.3 and 3.4, the LC-BOP+LRD method is found to be useful to estimate interaction energies and equilibrium geometries of open-shell van der Waals complexes within the DFT framework.

Table 3.3. CP-corrected interaction energies of open-shell van der Waals complexes.

	Spin multiplicity	Interaction energy (cm^{-1})										
		LC-UBOP		LC-UBOP+LRD		UωB97X-D		UM06-2X		UMP2		Ref.
$HO_2\cdots H_2O$	2	−602	(150)	−801	(−49)	−634	(118)	−807	(−55)	−419	(333)	−752 [a]
OH···CO	2	−614	(109)	−704	(19)	−674	(49)	−630	(93)	−758	(−35)	−723 [b]
NH···NH	5	−647	(46)	−733	(−40)	−632	(61)	−648	(45)	−672	(21)	−693 [c]
$OH\cdots N_2$	2	−351	(129)	−448	(32)	−350	(130)	−375	(105)	−473	(7)	−480 [b]
$NO\cdots H_2O$	2	−291	(171)	−399	(63)	−383	(79)	−414	(48)	−240	(222)	−462 [d]
$SH\cdots N_2$	2	−80	(172)	−215	(37)	−137	(115)	−111	(141)	−272	(−20)	−252 [b]
OH···Ar	2	−3.9	(136.5)	−104.0	(36.4)	−24.0	(116.4)	−88.6	(51.8)	128.3	(268.7)	−140.4 [e]
$O_2\cdots O_2$	5	28.7	(159.9)	−158.4	(−27.1)	−2.1	(129.2)	−158.3	(−27.1)	−150.6	(−19.3)	−131.2 [f]
NO···Ar	2	32.6	(148.5)	−134.0	(−18.1)	−37.0	(78.9)	−111.9	(4.0)	−93.1	(22.8)	−115.9 [g]
CN···Ne	2	3.3	(42.7)	−56.1	(−16.6)	−0.6	(38.8)	−89.0	(−49.5)	−30.2	(9.2)	−39.4 [c]
OH···He	2	2.8	(32.9)	−42.6	(−12.6)	7.6	(37.6)	−85.6	(−55.6)	−13.4	(16.6)	−30.0 [h]
NH···He	3	5.7	(25.5)	−33.9	(−14.1)	2.9	(22.8)	−50.3	(−30.5)	−10.0	(9.8)	−19.8 [c]
MD			(110.2)		(0.8)		(81.3)		(22.5)		(69.6)	
MAD			(110.2)		(30.4)		(81.3)		(58.7)		(81.9)	

[a] RCCSD(T)/aug-cc-pVTZ + midbond function [17].
[b] Averaged value of the CCSD(T)/CBS limits predicted with different interpolation methods [18].
[c] RCCSD(T)/aug-cc-pVQZ + midbond function [17].
[d] RCCSD(T)/aug-cc-pVTZ + midbond function [19].
[e] RCCSD(T)/aug-cc-pVQZ + midbond function [20]
[f] RCCSD(T)/ANO[6s5p3d2f] + midbond function [21].
[g] UCCSD(T)/CBS limit [22].
[h] RCCSD(T)/aug-cc-pVTZ + midbond function [23].

Table 3.4. Optimized geometric parameters of three open-shell van der Waals complexes. The units for distance and angle are Å and deg, respectively.

		LC-UBOP		LC-UBOP+LRD		Ref.
OH···CO	R(H···C)	2.327	(−0.007)	2.316	(−0.017)	2.333 [a]
NH···NH	R(H···N)	2.453	(−0.003)	2.454	(−0.002)	2.456 [b]
OH···N_2	R(H···N)	2.354	(0.034)	2.338	(0.018)	2.320 [a]
NO···H_2O	R(X···O_b)	3.73	(0.07)	3.64	(−0.02)	3.66 [c]
	α	44.4	(−6.6)	51.1	(0.1)	51.0 [c]
	β	113.5	(5.0)	107.9	(−0.6)	108.5 [c]
SH···N_2	R(H···N)	2.838	(0.222)	2.776	(0.160)	2.616 [a]
O_2···O_2	R(O···O)	3.896	(0.494)	3.334	(−0.068)	3.402 [d]
OH···He	R(X···He)	3.35	(0.34)	2.97	(−0.04)	3.01 [e]
	α	70.8	(2.0)	70.4	(1.6)	68.7 [e]
NH···He	R(X···He)	3.97	(0.62)	3.21	(−0.14)	3.35 [b]
	α	63.4	(1.1)	64.9	(2.6)	62.3 [b]

[a] Ref. [18]. [b] Ref. [17]. [c] Ref. [19]. [d] Ref. [21]. [e] Ref. [23].

* Differences from the references are shown in parentheses.

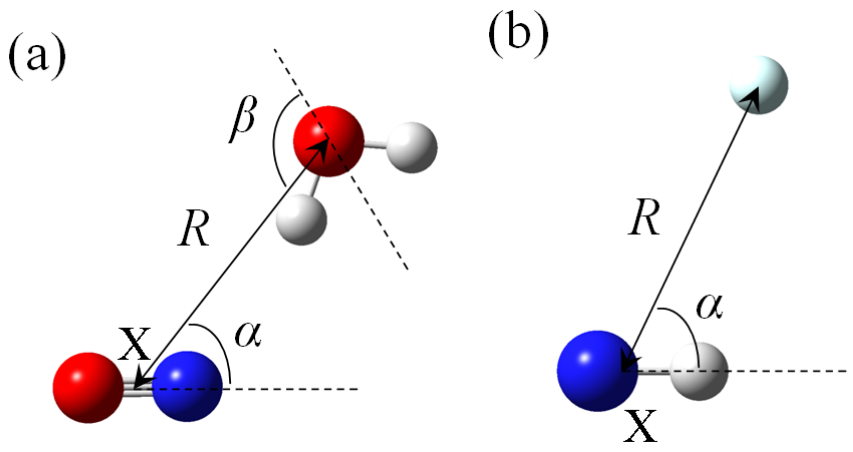

Figure 3.2. Geometric parameters of (a) NO···H_2O and (b) NH···He.

3.2.3 Nitroxide radical dimer

In this subsection, the magnetic coupling constant and singlet-triplet separation of nitroxide radical dimer $(H_2NO\cdot)_2$ are focused on as well as the interaction energy. This system is suitable for investigation of the applicability of the LC-BOP+LRD method to molecular magnetism, because it is the simplest model of nitroxide derivatives. The geometry of monomer is taken from an experimental study [27]: R(N-O) = 1.28 Å, R(N-H) = 1.01 Å, and ∠H-N-H = 122.7°. The geometric parameters of dimer are defined in Figure 3.3 (a).

The magnetic coupling constant J between radicals A and B is given by

$$J = \frac{E^{\mathrm{LS}} - E^{\mathrm{HS}}}{< S^2 >^{\mathrm{HS}} - < S^2 >^{\mathrm{LS}}}, \tag{3.3}$$

where E^{LS} and E^{HS} are total energies of low-spin (singlet) and high-spin (triplet) states, respectively [28]; J corresponds to the effective exchange integral in the Heisenberg model. Figures 3.3 (a) and (b) show the J values obtained using the cc-pVDZ basis set. Reported data calculated by the MkMRCC method [29] were adopted as reference. The results of the LC-BOP functional without dispersion correction are excluded because of a small difference in the J values: for example, the LRD energy contributed to J only by −1.4 cm^{-1} at R_x = 0.0 Å and R_z = 3.4 Å. In the case of R_x = 0.0 Å, negative (antiferromagnetic) values increased exponentially with decreasing R_z because of the SOMO-SOMO overlap. On the other hand, J became ferromagnetic with increasing R_x. In both cases, the LC-BOP+LRD and ωB97X-D functionals behaved similarly to the reference. The M06-2X functional resulted in more antiferromagnetic curves. In addition to the LC-BOP+LRD and ωB97X-D functionals, the CAM-B3LYP and LC-ωPBE functionals also evaluated accurate coupling constants [29]. This fact indicates the importance of the long-range correction.

The singlet-triplet separation $\Delta E_{\mathrm{S\text{-}T}}$ is defined as the difference between corresponding total energies,

$$\Delta E_{\mathrm{S-T}} = E_{\mathrm{singlet}} - E_{\mathrm{triplet}} . \tag{3.4}$$

Since the spin-unrestricted method yields open-shell singlet state including spin contamination, the AP method [28] was applied. According to the AP method, the total energy of the singlet state is corrected as follows:

$$E_{\mathrm{AP-singlet}} = E_{\mathrm{singlet}} + J \times < S^2 >_{\mathrm{singlet}} . \tag{3.5}$$

Calculated $\Delta E_{\mathrm{S-T}}$ is summarized in Figures 3.3 (c) and (d). Without the AP method, all functionals underestimated $\Delta E_{\mathrm{S-T}}$. The AP method approximately doubled $\Delta E_{\mathrm{S-T}}$. Similar to the J values, the LC-BOP+LRD and ωB97X-D functionals with the AP method provided reasonable curves of $\Delta E_{\mathrm{S-T}}$. The results explain the importance of eliminating spin contamination.

The singlet-state interaction energy ΔE_{int} is described in Figures 3.3 (e) and (f). The aug-cc-pVTZ basis set was adopted for UDFT calculations. The reference interaction energy was calculated at the APUCCSD(T)/CBS level, which is obtained using $<S^2>$ of the UMP1 wavefunction by the aug-cc-pVQZ basis set and the UCCSD(T)/CBS total energy evaluated by following formula:

$$E^{\mathrm{CBS}}_{\mathrm{UCCSD(T)}} = E^{\mathrm{aug-cc-pVQZ}}_{\mathrm{UHF}} + E^{\mathrm{CBS}}_{\mathrm{COR(UMP2)}} + (E^{\mathrm{aug-cc-pVTZ}}_{\mathrm{COR(UCCSD(T))}} - E^{\mathrm{aug-cc-pVTZ}}_{\mathrm{COR(UMP2)}}) , \tag{3.6}$$

where $E^{\mathrm{CBS}}_{\mathrm{COR(UMP2)}}$ was estimated by the Helgaker's extrapolation method [30]. ΔE_{int} is obtained by

$$\Delta E_{\mathrm{int}} = E_{\mathrm{singlet}} - 2E_{\mathrm{monomer}} , \tag{3.7}$$

or

$$\Delta E_{\mathrm{int}} = E_{\mathrm{AP\text{-}singlet}} - 2E_{\mathrm{monomer}} . \tag{3.8}$$

As shown in Figures 3.3 (e) and (f), ΔE_{int} obtained by Eq. (3.7) did not agree with the reference in the region of small R_x. The APLC-UBOP without dispersion correction underestimated ΔE_{int}. The APUωB97X-D also underestimated ΔE_{int}. Similar to the case of open-shell van der Waals complexes, this result may be originated in the empirical dispersion correction. The APLC-UBOP+LRD calculation was able to describe quantitatively accurate potential energy curve. Thus, the elimination of spin contamination, accurate long-range exchange, and density-dependent dispersion correction are required to reproduce the potential curve of open-shell singlet state of radical dimers.

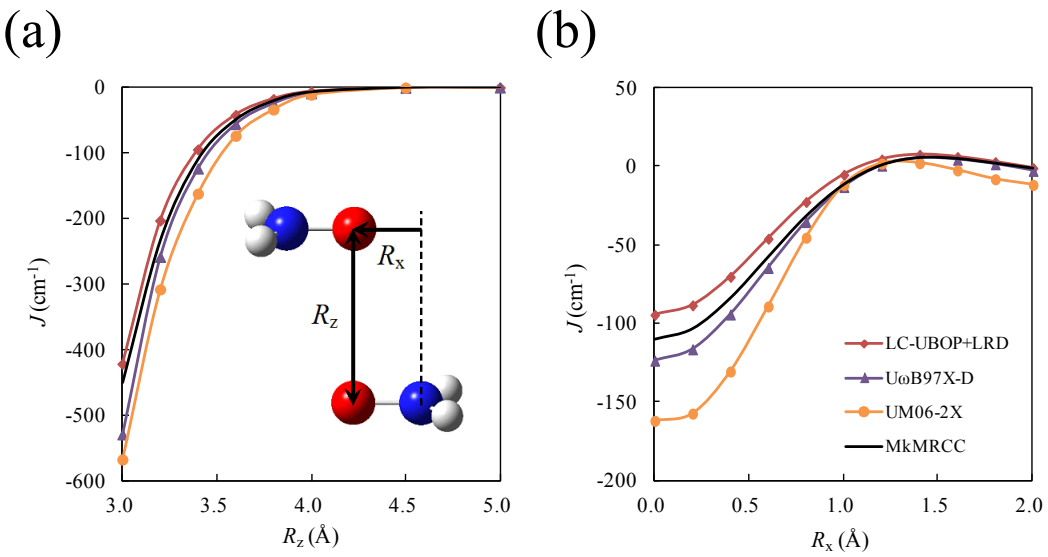

Figure 3.3. Magnetic coupling constants J, (a) and (b), singlet-triplet separation $\Delta E_{S\text{-}T}$, (c) and (d), and interaction energy ΔE_{int}, (e) and (f), of the nitroxide radical dimer. The distances of R_x and R_z are defined by an illustration in (a). R_z changes from 3.0 to 5.0 Å with fixing R_x = 0.0 Å in (a), (c), and (e). R_x changes from 0.0 to 2.0 Å with fixing R_z = 3.4 Å.

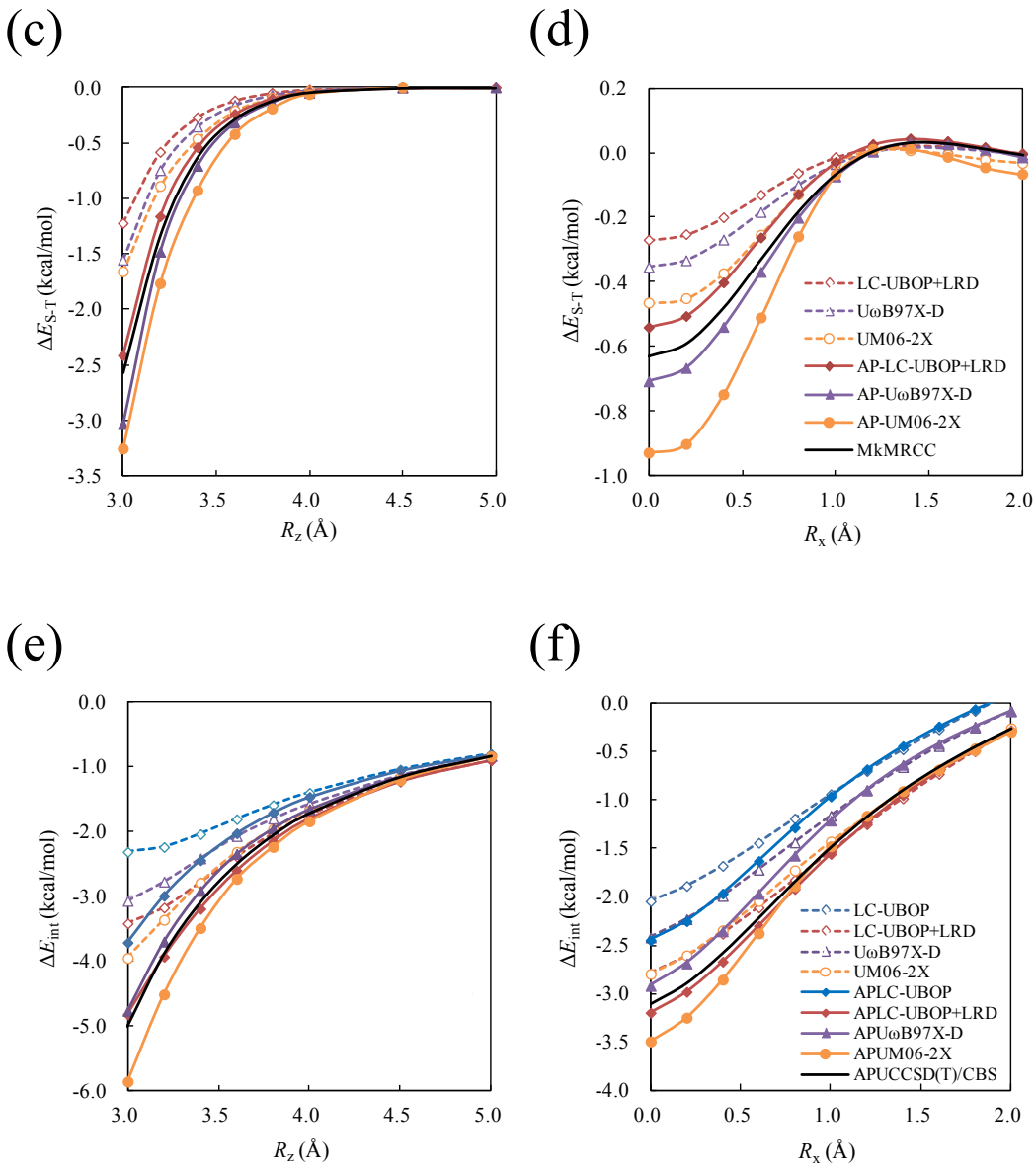

Figure 3.3. (continued.)

3.2.4. Phenalenyl radical dimer

Finally, π-stacked dimer of 2,5,8-tri-*tert*-butyl-phenalenyl radical illustrated in Figure 3.4 was investigated. The NMR study revealed an interplanar covalent bond called the 12-center 2-electron bond formed by delocalized SOMOs [31]. The distance between the central carbon atoms determined by X-ray diffraction was 3.201 Å [32], which was shorter than the sum of van der Waals radii of two carbon atoms but considerably longer than conventional C-C bond. Since covalent and noncovalent interactions are expected to contribute to the stabilization concertedly, the LC-UBOP+ LRD calculation was performed as an example of application to large systems.

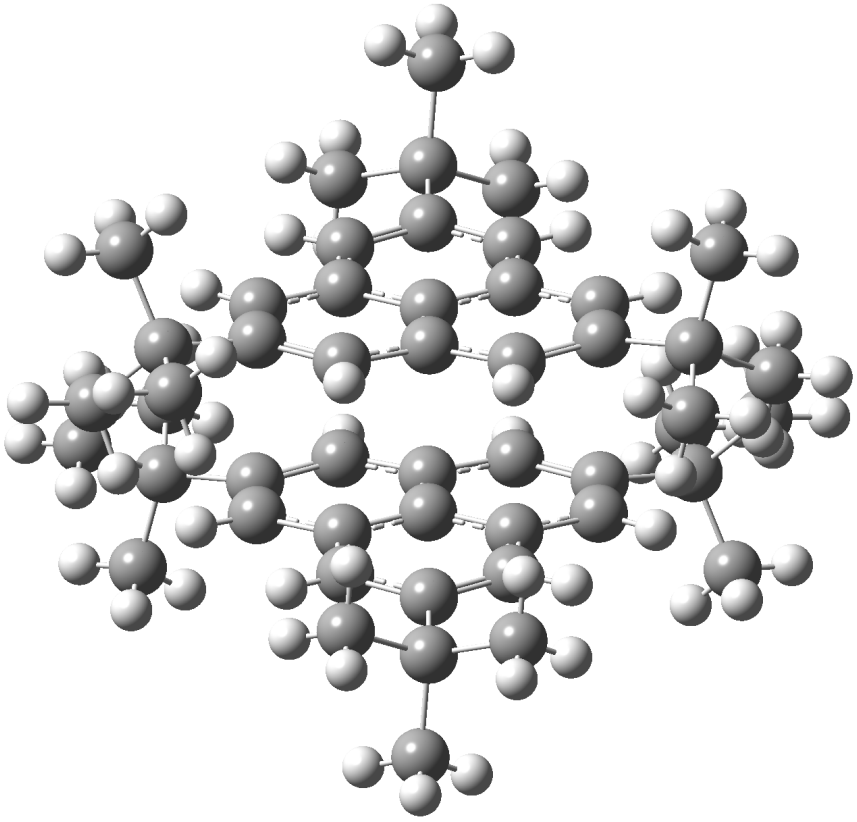

Figure 3.4. Geometry of the 2,5,8-tri-tert-butyl-phenalenyl radical dimer extracted from the crystal structure.

The geometry of the 2,5,8-tri-*tert*-butyl-phenalenyl radical dimer was extracted from the crystal structure [32]. The 6-31+G(d) basis set was adopted in all theoretical calculations. The PCM [33] was adopted to consider the electrostatic solvation effect. The solute-solvent dispersion and repulsion energy were considered through the FT model [34].

Table 3.5 summarizes the magnetic coupling constant J and interaction energy ΔE_{int}. In addition to the gas phase (i.e., no solvent effect) calculation, J and ΔE_{int} in dichloromethane was estimated using the PCM and FT model. The negative J values are consistent with the interplaner covalent interaction. The CASSCF method and M06-2X functional resulted in larger J values than the experimental value. The LC-UBOP provided similar J value to the MRMP method. The LRD method negatively increased the J value, which may be due to the interplanar distribution of the SOMO electrons in the singlet state. The solvent effect was small; the PCM and FT model slightly increased and decreased the absolute J values, respectively.

In terms of ΔE_{int} in the gas phase, LC-UBOP+LRD, UωB97X-D, and UM06-2X qualitatively agreed with the MRMP method [35]. These interaction energies are considerably larger than the experimental enthalpies [36,37], indicating large solvent effect. However, the PCM is not sufficient to estimate the decrease of $|\Delta E_{\mathrm{int}}|$. This is due to the small dielectric constant of dichloromethane. Including the solute-solvent dispersion interaction based on the FT model significantly decreased $|\Delta E_{\mathrm{int}}|$. The reason for this underestimation in the case of the M06-2X functional is speculated as the incorrect long-range asymptotic behavior. The LC-UBOP+LRD and UωB97X-D interaction energies with and without the AP method are consistent with the experimental enthalpy. The results encourage the application of the LC-BOP+LRD method to large systems.

Table 3.5. Magnetic coupling constants J and interaction energies ΔE_{int} of the 2,5,8-tri-*tert*-butyl-phenalenyl radical dimer.

	J (cm^{-1})			ΔE_{int} (kcal/mol)					
	Gas phase	PCM	PCM+FT	Gas phase		PCM		PCM+FT	
				w/o AP	w/ AP	w/o AP	w/ AP	w/o AP	w/ AP
LC-UBOP	−1488	−1495	−1455	6.4	0.9	8.1	2.8	22.5	17.2
LC-UBOP+LRD	−1518	−1543	−1502	−23.7	−29.3	−22.1	−27.6	−7.6	−13.1
UωB97X-D	−1737	−1767	−1723	−25.9	−30.3	−24.1	−28.6	−9.7	−14.1
UM06-2X	−2120	−2146	−2108	−19.2	−23.0	−17.4	−21.2	−2.9	−6.8
CASSCF(2,2) [a]	−2256			1.1					
MRMP [b]	−1451			−26.0					
Exp.	−1161 [c]							−8.8 [d], −9.5 [d]	

[a] Ref. [35]. The triplet state was calculated by the ROHF method.

[b] Ref. [35]. The triplet state was calculated by the MP2 method.

[c] Ref. [36].

[d] Enthalpy change of dimerization from Ref. [37].

3.3. Conclusion

The numerical assessment of the LRD method for open-shell systems was performed. The LRD method reproduced the dispersion coefficient of open-shell atoms accurately. Despite the lack of spin dependence, reasonable tendency of atomic polarizabilities was obtained because of the density dependence. As for the open-shell van der Waals complexes, the LRD method combined with the LC exchange functional evaluated the interaction energy accurately. The LC-BOP+LRD method also achieved reproduction of magnetic coupling constants and interaction energies of the radical dimers. These results support the availability of combination of the LRD method with the LC scheme to analyze and design magnetic materials based on organic radicals.

References

[1] T. Sato, H. Nakai, *J. Chem. Phys.* **131**, 224104 (2009).

[2] T. Sato, H. Nakai, *J. Chem. Phys.* **133**, 194101 (2010).

[3] J. F. Dobson, B. P. Dinte, *Phys. Rev. Lett.* **76**, 1780 (1996).

[4] S. N. Steinmann, C. Piemontesi, A. Delachat, C. Corminboeuf, *J. Chem. Theory Comput.* **8**, 1629 (2012).

[5] G. Chałasiński, M. M. Szczęśniak, *Chem. Rev.* **100**, 4227 (2000).

[6] R. G. Hicks, *Org. Biomol. Chem.* **5**, 1321 (2007).

[7] H. Iikura, T. Tsuneda, T. Yanai, K. Hirao, *J. Chem. Phys.* **115**, 3540 (2001).

[8] A. D. Becke, *Phys. Rev. A* **38**, 3098 (1988).

[9] T. Tsuneda, T. Suzumura, K. Hirao, *J. Chem. Phys.* **110**, 10664 (1999).

[10] M. W. Schmidt *et al.*, *J. Comput. Chem.* **14**, 1347 (1993).

[11] O. A. Vydrov, T. Van Voorhis, *Phys. Rev. A* **81**, 062708 (2010).

[12] D. J. Margoliash, W. J. Meath, *J. Chem. Phys.* **68**, 1426 (1978).

[13] X. Chu, A. Dalgarno, *J. Chem. Phys.* **121**, 4083 (2004).

[14] A. Derevianko, S. G. Porsev, J. F. Babb, *At. Data Nucl. Data Tables* **96**, 323 (2010).

[15] S. F. Boys, F. Bernardi, *Mol. Phys.* **19**, 553 (1970).

[16] M. J. Frisch *et al.*, Gaussian 09, Revision A.02, Gaussian, Inc, Wallingford, CT, 2009.

[17] P. S. Żuchowski, R. Podeszwa, R. Moszynski, B. Jeziorski, K. Szalewicz, *J. Chem. Phys.* **129**, 084101 (2008).

[18] S. Du, J. S. Francisco, *J. Chem. Phys.* **131**, 064307 (2009).

[19] H. Cybulski, P. S. Żuchowski, B. Fernández, J. Sadlej, *J. Chem. Phys.* **130**, 104303 (2009).

[20] G. Paterson, S. Marinakis, M. L. Costen, K. McKendrick, J. Kłos, R. Toboła, *J. Chem. Phys.* **129**, 074304 (2008).

[21] M. Bartolomei, E. Carmona-Novillo, M. I. Hernández, J. Campos-Martínez, R. Hernandez-Lamondea, *J. Chem. Phys.* **128**, 214304 (2008).

[22] M. H. Alexander, *J. Chem. Phys.* **111**, 7426 (1999).

[23] H. S. Lee, A. B. McCoy, R. R. Toczyłowski, S. M. Cybulski, *J. Chem. Phys.* **113**, 5736 (2000).

[24] J. -D. Chai, M. Head-Gordon, *Phys. Chem. Chem. Phys.* **10**, 6615 (2008).

[25] Y. Zhao, D. G. Truhlar, *Theor. Chem. Acc.* **120**, 215 (2008).

[26] L. Goerigk, S. Grimme, *Phys. Chem. Chem. Phys.* **13**, 6670 (2011).

[27] H. Mikami, S. Saito, S. Yamamoto, *J. Chem. Phys.* **94**, 3415 (1991).

[28] K. Yamaguchi, Y. Takahara, T. Fueno, *Appl. Quant. Chem.*, edited by V. H. Smith, H. F. Schaefer III, K. Morokuma, (D. Reidel, Boston, MA, 1986), p. 155.

[29] T. Saito, A. Ito, T. Watanabe, T. Kawakami, M. Okumura, K. Yamaguchi, *Chem. Phys. Lett.* **542**, 19 (2012).

[30] A. Halkier, T. Helgaker, P. Jørgensen, W. Klopper, H. Koch, J. Olsen, A. K. Wilson, *Chem. Phys. Lett.* **286**, 243 (1998).

[31] S. Suzuki, Y. Morita, K. Fukui, K. Sato, D. Shiomi, T. Takui, K. Nakasuji, *J. Am. Chem. Soc.* **128**, 2530 (2006).

[32] K. Goto *et al.*, *J. Am. Chem. Soc.* **121**, 1619 (1999).

[33] G. Scalmani, M. J. Frisch, *J. Chem. Phys.* **132**, 114110 (2010).

[34] F. Florsi, J. Tomasi, J. L. Pascual-Ahuir, *J. Comput. Chem.* **12**, 784 (1991).

[35] F. Mota, J. S. Miller, J. J. Novoa, *J. Am. Chem. Soc.* **131**, 7699 (2009).

[36] Y. Morita *et al.*, *Angew. Chem. Int. Ed.* **41**, 1793 (2002).

[37] J-M. Lü, S. V. Rosokha, J. K. Kochi, *J. Am. Chem. Soc.* **125**, 12161 (2003).

Chapter 4
Local Response Dispersion Method for Excited-State Calculation based on Time-Dependent Density Functional Theory

4.1. Introduction

TDDFT was developed to investigate response properties and electronic dynamics of molecules. The TDKS equation, which is a fundamental equation in TDDFT, can be solved in three ways: by an eigenvalue problem [1-3], by time-dependent coupled perturbed equations [4-6], and by real-time propagation [7-9]. The solution of the eigenvalue problem is utilized to obtain excitation energies. Although the underestimation of Rydberg [10,11], charge-transfer [12], and core [13,14] excitation energies was pointed out as a serious drawback of TDDFT, appropriate mixing of the HF exchange term eliminated the problem. The long-range correction to the exchange functional improves the accuracy of Rydberg and charge-transfer excitations [15,16]. The core-valence-Rydberg-B3LYP hybrid functional [17-19] provides accurate energies for Rydberg and core excitations. Nowadays, TDDFT is a popular choice for treating excited states because of the balance between computational cost and accuracy. Hereafter, the term TDDFT is used in the context of solving the eigenvalue problem.

TDDFT has been applied not only to single molecules but also to molecular complexes. For example, conformational changes of the pyridine-water complex [20] and its analogues [21,22], induced by π-π* and n-π* excitations, have been investigated. Geometries and interaction energies in the S_1 state of anisole-ammonia [23,24] and anisole-water [24,25] complexes have also been investigated. In addition to the interaction between π-conjugated systems and small molecules, TDDFT has been applied to π/π stacked excited-states of aromatic hydrocarbon dimers [26-28], DNA base clusters [29-34], and dye aggregates [35]. The excited state of π/π stacked dimers is termed aromatic excimer, where exciton localization and charge-transfer interaction increase the binding energy and decrease the intermolecular distance from the ground state.

In the field of time-independent DFT, a number of dispersion correction methods [36-46] have been developed to improve the description of weakly bound complexes due to the local nature of exchange-correlation functionals. Since the same functionals are used in TDDFT, the dispersion correction method should be applied to excited-state molecular complexes. However, most of the dispersion correction methods have not been applied to TDDFT. In particular, the widely used DFT-D method [37-39] was adopted in several studies [24,27,35] in which dispersion coefficients prepared for the ground state were straightforwardly applied to the excited state. In terms of reliability, state-specific dispersion correction is desired, in which the electron redistribution induced by electronic excitation is reflected.

The purpose of this chapter is to combine TDDFT and the LRD method [45,46] for the excited-state calculation of molecular complexes. The LRD method calculates dispersion correction energies using the electron density and gradient with low computational cost. First, the LRD treatment within the TDDFT framework is explained. Then, the proposed method is numerically tested for exciton-localized and exciton-resonance systems, namely, π-conjugated systems interacting with unconjugated molecules and aromatic excimers.

4.2. Theory

In this chapter, the state-specific dispersion correction within the TDDFT framework is examined on the basis of the LRD method. The dispersion correction energy E_{LRD} for the excited state is computed after calculating excitation energies. The dispersion-corrected total energy is estimated as the sum of the ground-state energy without dispersion correction E_{DFT}, the excitation energy ω_{TDDFT}, and E_{LRD}.

$$E_{\mathrm{TDDFT+LRD}} = E_{\mathrm{DFT}} + \omega_{\mathrm{TDDFT}} + E_{\mathrm{LRD}} \tag{4.1}$$

This *posteriori* treatment is thought to be reasonable because the self-consistent treatment of the LRD method developed in Chapter 2 did not change total energies and

electron distribution significantly.

Previously, the ground-state LRD energy was derived from the intermolecular dispersion energy between two molecules [45,46]. Here, the derivation of the excited-state LRD energy is discussed. Assuming a molecule A in the mth excited state and a molecule B in the ground state, the second-order perturbation theory gives the intermolecular dispersion energy as [47]

$$E_{\mathrm{disp}}[A^{*}\cdots B]=-\sum_{m'\neq m}^{A}\sum_{n\neq 0}^{B}\frac{\left|\left\langle m'^{A}n^{B}\left|\hat{V}_{AB}\right|m^{A}0^{B}\right\rangle\right|^{2}}{\omega_{m\to m'}^{A}+\omega_{0\to n}^{B}}, \tag{4.2}$$

where $\hat{V}_{AB}$ is the electrostatic interaction operator between two molecules. $\left|m^{A}\right\rangle$ and $\left|0^{B}\right\rangle$ are the mth excited and the ground states of the molecules A and B, respectively. $\omega_{m\to m'}^{A}$ is the change of energy with respect to molecule A between mth and m'th excited states. Applying the following integral transformation:

$$\frac{1}{a+b}=\frac{2}{\pi}\int_{0}^{\infty}\mathrm{d}u\,\frac{a}{a^{2}+u^{2}}\frac{b}{b^{2}+u^{2}}, \tag{4.3}$$

the intermolecular dispersion energy is expressed as

$$E_{\mathrm{disp}}[A^{*}\cdots B]=-\frac{1}{2\pi}\int d\mathbf{r}_{1}d\mathbf{r}_{1}'d\mathbf{r}_{2}d\mathbf{r}_{2}'\times\int_{0}^{\infty}du\,\frac{\chi^{A}(\mathbf{r}_{1},\mathbf{r}_{1}',iu)\chi^{B}(\mathbf{r}_{2},\mathbf{r}_{2}',iu)}{\left|\mathbf{r}_{1}-\mathbf{r}_{2}\right|\left|\mathbf{r}_{1}'-\mathbf{r}_{2}'\right|} \tag{4.4}$$

in terms of the dynamic density response functions χ^{A} and χ^{B} defined by

$$\chi^{A}(\mathbf{r}_{1},\mathbf{r}_{1}',\omega)=2\sum_{m'\neq m}^{A}\frac{\omega_{m\to m'}^{A}}{(\omega_{m\to m'}^{A})^{2}-\omega^{2}}\left\langle m^{A}\left|\hat{\rho}^{A}(\mathbf{r}_{1})\right|m'^{A}\right\rangle\left\langle m'^{A}\left|\hat{\rho}^{A}(\mathbf{r}_{1}')\right|m^{A}\right\rangle, \tag{4.5}$$

$$\chi^{B}(\mathbf{r}_{2},\mathbf{r}_{2}',\omega)=2\sum_{n\neq 0}^{B}\frac{\omega_{0\to n}^{B}}{(\omega_{0\to n}^{B})^{2}-\omega^{2}}\left\langle 0^{B}\left|\hat{\rho}^{B}(\mathbf{r}_{2})\right|n^{B}\right\rangle\left\langle n^{B}\left|\hat{\rho}^{B}(\mathbf{r}_{2}')\right|0^{B}\right\rangle, \tag{4.6}$$

where $\hat{\rho}^{A}(\mathbf{r})=\sum_{i}^{A}\delta^{3}(\mathbf{r}-\mathbf{r}')$ is the density operator. After the multicenter-multipole

expansion of the Coulomb operator, i.e.

$$\frac{1}{|\mathbf{r}_1-\mathbf{r}_2|}=\sum_a^A\sum_b^B w_a(\mathbf{r}_1)w_b(\mathbf{r}_2)\sum_{l_1=0}^{\infty}\sum_{l_2=0}^{\infty}R_{ab}^{-l_1-l_2-1}$$

$$\times\sum_{m_1m_2}S_{m_1m_2}^{ab(l_1l_2)}R_{l_1m_1}(\mathbf{r}_1-\mathbf{r}_a)R_{l_2m_2}(\mathbf{r}_2-\mathbf{r}_b)\,, \tag{4.7}$$

let us approximate the response functions as follows:

$$\chi(\mathbf{r},\mathbf{r}',\omega)=\nabla\cdot\nabla'\left[\frac{\rho^{\mathrm{es}}(\mathbf{r})}{\{\omega_{\mathbf{q}=0}^{\mathrm{es}}(\mathbf{r})\}^2-\omega^2}\delta^3(\mathbf{r}-\mathbf{r}')\right], \tag{4.8}$$

where ρ^{es} is the excited-state electron density of the whole system, and $\omega_{\mathbf{q}=0}^{\mathrm{es}}$ is the dispersion relation computed by ρ^{es} and its gradient. Eq. (4.8) is the application of the local response approximation, which was proposed by Dobson and Dinte [48] to the excited state. Similar to the ground state, the extension to the intramolecular interaction is possible by the multiplication of the damping function. Consequently, the LRD energy is obtained as

$$E_{\mathrm{LRD}}=-\frac{1}{2}\sum_{aa'}\sum_{tt'}\int_0^{\infty}\mathrm{d}u\,\alpha_{tt'}^{aa'}(\mathrm{i}u)\beta_{tt'}^{aa'}(\mathrm{i}u)\,, \tag{4.9}$$

$$\beta_{tt'}^{aa'}(\mathrm{i}u)=\sum_{bb'}\sum_{uu'}f_{tu,t'u'}^{ab,a'b'}T_{tu}^{ab}T_{t'u'}^{a'b'}\alpha_{uu'}^{bb'}(\mathrm{i}u)\,, \tag{4.10}$$

$$\alpha_{tt'}^{aa'}(\mathrm{i}u)=\int\mathrm{d}\mathbf{r}\;w_a(\mathbf{r})w_{a'}(\mathbf{r})\frac{\rho^{\mathrm{es}}(\mathbf{r})}{\{\omega_{\mathbf{q}=0}^{\mathrm{es}}(\mathbf{r})\}^2+u^2}\nabla R_t(\mathbf{r}-\mathbf{R}_a)\cdot\nabla R_{t'}(\mathbf{r}-\mathbf{R}_{a'})\,. \tag{4.11}$$

Here, the LRD energy is written in terms of composite variables $t,t',u,u'\in\{lm;-l\le m\le l;l\ge 1\}$. In this chapter, Becke-type partition function [49] was adopted for w_a in Eq. (4.11). Eqs. (4.9)-(4.11) are essentially the same formulas presented in the previous subsection except replacing the ground-state electron density and its gradient with excited-state ones.

To compute excited-state electron density, the relaxed difference density matrix **P**

$$\rho^{\mathrm{es}}(\mathbf{r}) = \rho^{\mathrm{gs}}(\mathbf{r}) + \sum_{\mu\nu} P_{\mu\nu}\chi_\mu(\mathbf{r})\chi_\nu(\mathbf{r}), \tag{4.12}$$

is required, where $\rho^{\mathrm{gs}}(\mathbf{r})$ is the ground-state electron density, and χ_μ is the atomic orbital. How to obtain the difference density matrix is explained hereafter. In TDDFT calculations, excitation energy ω and corresponding excitation vectors **X** and **Y** are obtained by solving a non-Hermitian eigenvalue equation [1],

$$\begin{pmatrix} \mathbf{A} & \mathbf{B} \\ \mathbf{B} & \mathbf{A} \end{pmatrix}\begin{pmatrix} \mathbf{X} \\ \mathbf{Y} \end{pmatrix} = \omega \begin{pmatrix} \mathbf{1} & \mathbf{0} \\ \mathbf{0} & -\mathbf{1} \end{pmatrix}\begin{pmatrix} \mathbf{X} \\ \mathbf{Y} \end{pmatrix}. \tag{4.13}$$

The elements of matrices **A** and **B** are given as follows [3]:

$$A_{ai,bj} = \delta_{ab}\delta_{ij}(\varepsilon_a - \varepsilon_i) + K_{ai,bj} \tag{4.14}$$

and

$$B_{ai,bj} = K_{ai,jb}, \tag{4.15}$$

where ε_p is the pth KS orbital energy. The above equations utilize the convention that $\{a, b, \ldots\}$ are virtual orbitals and $\{i, j, \ldots\}$ are occupied orbitals. Matrix element in Eqs. (4.14) and (4.15) is given by

$$K_{pq\sigma,rs\sigma'} = (pq\sigma \mid rs\sigma') - c_x\delta_{\sigma\sigma'}(pr\sigma \mid qs\sigma') + f^{\mathrm{xc}}_{pq\sigma rs\sigma'}, \tag{4.16}$$

where $\{p, q, \ldots\}$ indicate general KS orbitals, and σ and σ' are spin indices. $(pq\sigma \mid rs\sigma')$ is a two-electron integral in Mulliken notation, and c_x is a mixing rate of the HF exchange integral in hybrid functionals. $f^{\mathrm{xc}}_{\sigma\sigma'}$ is a Hessian matrix element of the exchange-correlation functional. Under the adiabatic approximation, $f^{\mathrm{xc}}_{\sigma\sigma'}$ is given as the second derivative with respect to electron density:

$$f_{\sigma\sigma'}^{\mathrm{xc}} = \frac{\delta^2 E_{\mathrm{xc}}}{\delta\rho_\sigma(\mathbf{r}_1)\delta\rho_{\sigma'}(\mathbf{r}_2)}. \tag{4.17}$$

According to previous studies [50,51], the relaxed one-particle difference density matrix **P** was derived for the computation of excited-state response properties and analytical gradients of excitation energies. The matrix **P** consists of two parts,

$$\mathbf{P} = \mathbf{T} + \mathbf{Z}, \tag{4.18}$$

where unrelaxed difference density matrix **T** contains three types of elements,

$$T_{ab\sigma} = \frac{1}{2}\sum_i \left\{(\mathbf{X}+\mathbf{Y})_{ia\sigma}(\mathbf{X}+\mathbf{Y})_{ib\sigma} + (\mathbf{X}-\mathbf{Y})_{ia\sigma}(\mathbf{X}-\mathbf{Y})_{ib\sigma}\right\}, \tag{4.19}$$

$$T_{ij\sigma} = -\frac{1}{2}\sum_a \left\{(\mathbf{X}+\mathbf{Y})_{ia\sigma}(\mathbf{X}+\mathbf{Y})_{ja\sigma} + (\mathbf{X}-\mathbf{Y})_{ia\sigma}(\mathbf{X}-\mathbf{Y})_{ja\sigma}\right\}. \tag{4.20}$$

and

$$T_{ia\sigma} = T_{ai\sigma} = 0. \tag{4.21}$$

The remaining part of the density matrix is obtained from the Z-vector equation:

$$\sum_{jb\sigma'} (\mathbf{A}+\mathbf{B})_{ia\sigma jb\sigma'} Z_{jb\sigma'} = -R_{ia\sigma}, \tag{4.22}$$

$$\begin{aligned} R_{ia\sigma} = &\sum_b \left\{(\mathbf{X}+\mathbf{Y})_{ib\sigma} H^+_{ab\sigma}[\mathbf{X}+\mathbf{Y}] + (\mathbf{X}-\mathbf{Y})_{ib\sigma} H^-_{ab\sigma}[\mathbf{X}-\mathbf{Y}]\right\} \\ &- \sum_j \left\{(\mathbf{X}+\mathbf{Y})_{ja\sigma} H^+_{ji\sigma}[\mathbf{X}+\mathbf{Y}] + (\mathbf{X}-\mathbf{Y})_{ja\sigma} H^-_{ji\sigma}[\mathbf{X}-\mathbf{Y}]\right\} \\ &+ H^+_{ia\sigma}[\mathbf{T}] + 2\sum_{jb\sigma' kc\sigma''} g^{\mathrm{xc}}_{ia\sigma jb\sigma' kc\sigma''} (\mathbf{X}+\mathbf{Y})_{ja\sigma'} (\mathbf{X}+\mathbf{Y})_{kc\sigma''}, \end{aligned} \tag{4.23}$$

where for arbitrary vectors **V**,

$$H^{+}_{ab\sigma}[\mathbf{V}] = \sum_{rs\sigma'} \Big\{ 2(pq\sigma \,|\, rs\sigma') + 2 f^{\mathrm{xc}}_{pq\sigma rs\sigma'} - c_x \delta_{\sigma\sigma'} [(ps\sigma \,|\, rq\sigma) + (pr\sigma \,|\, sq\sigma)] \Big\} V_{rs\sigma}, \tag{4.24}$$

$$H^{-}_{pq\sigma}[\mathbf{V}] = \sum_{rs\sigma'} \Big\{ c_x \delta_{\sigma\sigma'} [(ps\sigma \,|\, rq\sigma) - (pr\sigma \,|\, sq\sigma)] \Big\} V_{rs\sigma}, \tag{4.25}$$

and $g^{\mathrm{xc}}_{ia\sigma jb\sigma' kc\sigma''}$ is the third-order derivative of the exchange-correlation functional given as

$$g^{\mathrm{xc}}_{\sigma\sigma'\sigma''}(\mathbf{r},\mathbf{r}',\mathbf{r}'') = \frac{\delta^3 E_{\mathrm{xc}}}{\delta\rho_{\sigma}(\mathbf{r})\delta\rho_{\sigma'}(\mathbf{r}')\delta\rho_{\sigma''}(\mathbf{r}'')}. \tag{4.26}$$

4.3. Computational details

The LC [52] Becke-88 [53] exchange with the one-parameter progressive correlation [54] functional, as denoted by LC-BOP, was adopted in DFT and TDDFT calculations. The range separation parameter μ for the LC scheme is 0.33, which is suitable for describing the excited state [15]. In the LRD calculation, different ranks of polarizabilities were excluded, i.e., $l = l'$ in Eq. (4.11). The multipole expansion of the LRD energy is truncated up to sixth, eighth, and tenth order two-center and sixth order multicenter interactions. The dielectric model parameter λ and the damping parameters κ and R_0 were optimized to reproduce the C_6 dispersion coefficients of rare gas dimers [55] and their interaction energies at the equilibrium distances [56], respectively. The optimized parameters were λ = 0.234, κ = 0.59, and R_0 = 3.83, in atomic units. The TDDFT+LRD calculations are performed by modifying the GAMESS program package [57]. For comparison, the CIS(D) [58] and the EOM-CCSD [59] calculations were performed using the Gaussian 09 package [60].

4.4. Results and discussion

4.4.1. Exciton-localized systems

The author calculated molecular complexes consisting of single π-conjugated and single unconjugated molecules in the ground state and the lowest singlet n-π* and π-π* excited states. 16 systems, as shown in Figure 4.1, were taken from the S66 benchmark set [61,62]. Optimized geometries at the MP2/cc-pVTZ level were used in both ground- and excited-state calculations. The 6-311++G(2d,2p) basis set [63-65] was used in TDDFT(+LRD) and CIS(D) calculations. BSSE was eliminated by the Boys-Bernardi CP correction [66]. By using Xantheas notation [67], the CP-corrected interaction energy of the excited-state complex was described as follows:

$$\Delta E_{\mathrm{TDDFT(+LRD)}}[(AB)^*] = E^{\alpha\cup\beta}_{\mathrm{TDDFT(+LRD)}}[(AB)^*] - \{E^{\alpha\cup\beta}_{\mathrm{TDDFT(+LRD)}}[A^*] + E^{\alpha\cup\beta}_{\mathrm{DFT(+LRD)}}[B]\}, \quad (4.27)$$

$$\Delta E_{\mathrm{CIS(D)}}[(AB)^*] = E^{\alpha\cup\beta}_{\mathrm{CIS(D)}}[(AB)^*] - \{E^{\alpha\cup\beta}_{\mathrm{CIS(D)}}[A^*] + E^{\alpha\cup\beta}_{\mathrm{MP2}}[B]\}. \quad (4.28)$$

In Eqs. (4.27) and (4.28), A and B correspond to π-conjugated and unconjugated molecules, respectively. α and β are basis functions of molecules A and B. The asterisk designates the excited state. Since E means total energy, the difference ΔE corresponds to interaction energy.

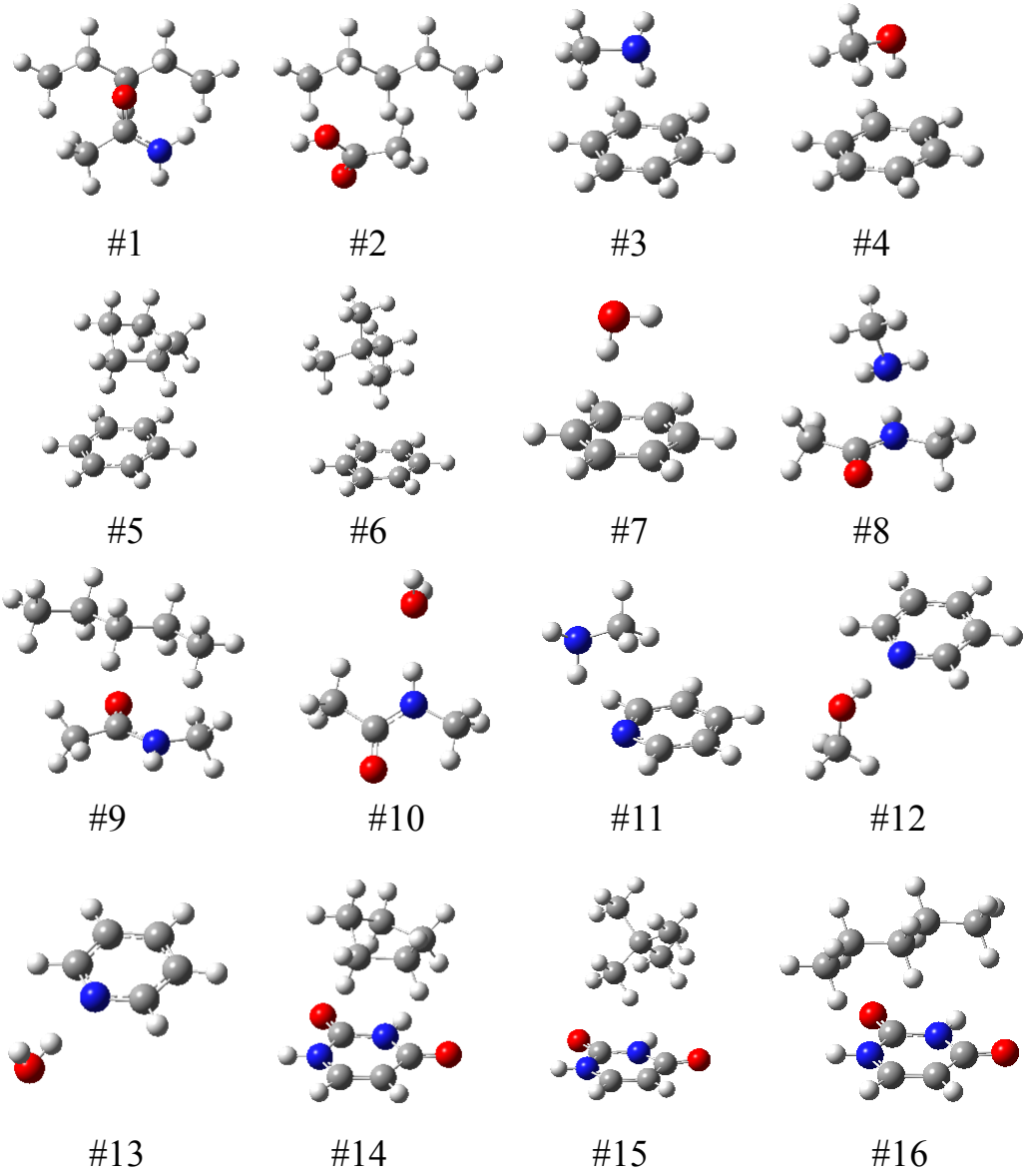

Figure 4.1. Structures of 16 complexes including a π-conjugated molecule taken from the S66 benchmark set.

The reference value of the interaction energy for the ground state was estimated at the CCSD(T)/CBS level [62]. For the excited-state reference, the author estimated the shift in the EOM-CCSD excitation energies induced by the intermolecular interaction, which is added to the ground-state reference:

$$\Delta E_{\text{Est.EOM-CCSD(T)}}[(AB)^*] = \Delta E^{\text{CBS}}_{\text{CCSD(T)}}[AB] + \{E^{\alpha\cup\beta}_{\text{EOM-CCSD}}[(AB)^*] - E^{\alpha\cup\beta}_{\text{CCSD}}[AB]\}$$
$$- \{E^{\alpha\cup\beta}_{\text{EOM-CCSD}}[A^*] - E^{\alpha\cup\beta}_{\text{CCSD}}[A]\}. \quad (4.29)$$

This procedure was previously adopted in highly accurate calculations of S_1-state potential energy surfaces of the benzene-argon complex [68] and its derivatives [69,70]. In the EOM-CCSD calculation, the 6-31+G(d) basis set [65,71,72] was adopted for benzene-cyclopropane, benzene-propane, and three complexes including uracil. The other systems were calculated using the 6-31++G(d,p) basis set [65,71,72].

First, the excited-state dispersion correction energies and atomic polarizabilities are compared with ground-state ones. Table 4.1 shows LRD energies of 16 molecular complexes. Both the π-π* and n-π* electronic excitations increase the LRD energy. The increase is small compared to the total LRD energy: the ratio is less than 2.5%.

Table 4.1. LRD energies of 16 complexes consisting of single π-conjugated and single unconjugated molecule taken from the S66 benchmark set (in mHartree).

		Ground state	π-π* excited state		n-π* excited state	
#1	$AcNH_2$-pentane	–7.710			–7.803	(–0.093)
#2	AcOH-pentane	–7.217			–7.251	(–0.034)
#3	Benzene-$MeNH_2$	–5.186	–5.287	(–0.101)		
#4	Benzene-MeOH	–4.921	–5.014	(–0.093)		
#5	Benzene-cyclopentane	–9.505	–9.627	(–0.123)		
#6	Benzene-neopentane	–10.107	–10.231	(–0.123)		
#7	Benzene-water	–3.602	–3.677	(–0.075)		
#8	Peptide-$MeNH_2$	–3.784			–3.870	(–0.086)
#9	Peptide-pentane	–9.368			–9.423	(–0.055)
#10	Peptide-water	–2.328			–2.378	(–0.050)
#11	Pyridine-$MeNH_2$	–4.524	–4.609	(–0.085)	–4.598	(–0.075)
#12	Pyridine-MeOH	–3.103	–3.158	(–0.056)	–3.149	(–0.046)
#13	Pyridine-water	–2.457	–2.490	(–0.033)	–2.504	(–0.047)
#14	Uracil-cyclopentane	–10.298	–10.460	(–0.163)	–10.335	(–0.037)
#15	Uracil-neopentane	–11.034	–11.185	(–0.152)	–11.063	(–0.029)
#16	Uracil-pentane	–11.022	–11.159	(–0.137)	–11.069	(–0.047)

* Differences from the ground state are shown in parentheses.

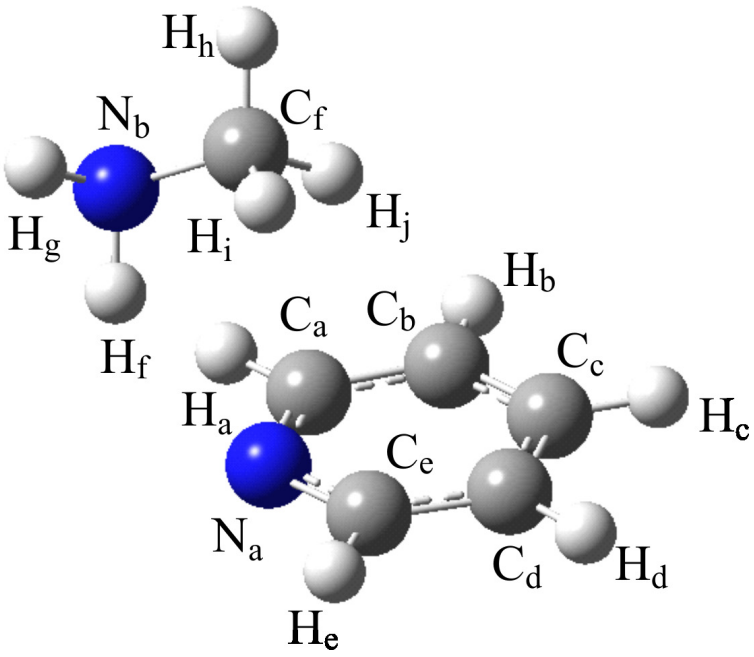

Figure 4.2. Geometry and labeling of the pyridine-$MeNH_2$ complex.

Table 4.2 represents static atomic polarizabilities of the pyridine-$MeNH_2$ complex obtained by Eq. (1.30). In the π-π* excitation, polarizabilities of all atoms belonging to pyridine increase. This tendency is consistent with the fact that the π-π* excited-state polarizability of benzene is larger than that of the ground state [73,74]. Polarizabilities of H_i and H_j also increase, which may reflect the diffusion of π electron density. The other atoms in $MeNH_2$ are nearly unchanged. In contrast, the n-π* excitation significantly decrease the polarizability of N_a atom while the other atomic polarizabilities in pyridine and those of H_i and H_j increase as in the π-π* excited state. These trends are consistent with the electron redistribution of the n-π* excitation. Although the change of LRD energies is not significant, the atomic polarizabilities indicates the robustness of the present treatment compared to applying a ground-state dispersion correction to the excited state.

Table 4.2. Static atomic polarizabilities of the pyridine-$MeNH_2$ complex calculated by Eq. (1.30) using ground-state, lowest π-π* excited-state, and lowest n-π* excited-state electron density (in a.u.).

		Ground state	π-π* excited state		n-π* excited state	
Pyridine	C_a	7.81	8.03	(0.22)	8.11	(0.30)
	C_b	7.31	7.42	(0.11)	7.52	(0.21)
	C_c	7.13	7.34	(0.21)	7.53	(0.40)
	C_d	7.24	7.32	(0.08)	7.47	(0.23)
	C_e	7.93	8.18	(0.25)	8.32	(0.39)
	H_a	4.22	4.43	(0.21)	4.50	(0.28)
	H_b	3.56	3.66	(0.09)	3.63	(0.07)
	H_c	3.49	3.90	(0.41)	4.02	(0.53)
	H_d	3.59	3.67	(0.09)	3.64	(0.05)
	H_e	3.56	3.75	(0.19)	3.85	(0.29)
	N_a	6.45	6.49	(0.05)	5.67	(–0.78)
$MeNH_2$	C_f	4.55	4.55	(–0.00)	4.54	(–0.01)
	H_f	6.32	6.35	(0.03)	6.11	(–0.20)
	H_g	3.34	3.33	(–0.01)	3.31	(–0.03)
	H_h	3.57	3.56	(–0.01)	3.53	(–0.04)
	H_i	4.33	4.48	(0.15)	4.52	(0.19)
	H_j	7.50	7.62	(0.12)	7.68	(0.18)
	N_b	4.71	4.74	(0.02)	4.68	(–0.03)

* Differences from the ground state are shown in parentheses.

Interaction energies in the π-π* and n-π* excited states are summarized in Tables 4.3 and 4.4, respectively. The LRD method improves the accuracy of interaction energies in dispersion-dominated systems. The TD-LC-BOP+LRD approach provides a small MD and MAD. In contrast, the CIS(D) method, which can be thought of as an analogue of MP2 for the excited state, severely overestimates the interaction energies of the uracil-cyclopentane and uracil-neopentane complexes in the π-π* excited state and underestimates those in the n-π* excited state. These deviations were interpreted as a breakdown of the perturbation due to nearly degenerated states at the CIS level. For example, the lowest singlet n-π* and π-π* CIS excitation energies of the uracil-neopentane complex were calculated to be 6.346 and 6.355 eV, respectively.

Table 4.3. Lowest singlet π-π* excited-state interaction energies of 11 molecular complexes from the S66 benchmark set (in kcal/mol).

		TD-LC-BOP		TD-LC-BOP+LRD		CIS(D)		Est. EOM-CCSD(T)
#3	Benzene-$MeNH_2$	–0.79	(2.01)	–2.74	(0.06)	–2.93	(–0.13)	–2.80
#4	Benzene-MeOH	–1.71	(1.77)	–3.55	(–0.06)	–3.49	(–0.01)	–3.49
#5	Benzene-cyclopentane	–0.05	(3.40)	–3.11	(0.34)	–4.02	(–0.57)	–3.45
#6	Benzene-neopentane	–0.12	(2.74)	–2.79	(0.07)	–3.21	(–0.35)	–2.86
#7	Benzene-water	–1.81	(0.86)	–2.88	(–0.21)	–2.48	(0.20)	–2.67
#11	Pyridine-$MeNH_2$	–2.35	(1.84)	–4.06	(0.13)	–3.96	(0.23)	–4.19
#12	Pyridine-MeOH	–7.45	(0.25)	–8.37	(–0.67)	–7.04	(0.66)	–7.70
#13	Pyridine-water	–7.40	(–0.25)	–7.96	(–0.80)	–6.48	(0.67)	–7.15
#14	Uracil-cyclopentane	–0.46	(4.06)	–3.85	(0.68)	–5.83	(–1.31)	–4.52
#15	Uracil-neopentane	–0.69	(3.50)	–3.77	(0.43)	–9.00	(–4.80)	–4.20
#16	Uracil-pentane	–0.73	(4.62)	–4.47	(0.88)	–5.47	(–0.12)	–5.35
	MD		(2.26)		(0.08)		(–0.50)	
	MAD		(2.30)		(0.39)		(0.82)	

* Differences from the ground state are shown in parentheses.

Table 4.4. Lowest singlet n-π* excited-state interaction energies of 11 molecular complexes from the S66 benchmark set (in kcal/mol).

		TD-LC-BOP		TD-LC-BOP+LRD		CIS(D)		Est. EOM-CCSD(T)
#1	$AcNH_2$-pentane	0.05	(2.81)	–2.48	(0.29)	–2.62	(0.14)	–2.76
#2	AcOH-pentane	–0.30	(2.73)	–2.67	(0.36)	–2.87	(0.17)	–3.03
#8	Peptide-$MeNH_2$	–5.67	(1.15)	–6.97	(–0.15)	–6.31	(0.51)	–6.82
#9	Peptide-pentane	–0.40	(3.66)	–3.52	(0.55)	–3.93	(0.13)	–4.07
#10	Peptide-water	–4.28	(0.35)	–4.81	(–0.19)	–4.09	(0.54)	–4.63
#11	Pyridine-$MeNH_2$	–0.77	(1.90)	–2.50	(0.17)	–3.17	(–0.50)	–2.67
#12	Pyridine-MeOH	–1.06	(0.51)	–2.01	(–0.44)	–1.77	(–0.20)	–1.57
#13	Pyridine-water	–0.74	(–0.12)	–1.31	(–0.70)	–0.88	(–0.27)	–0.62
#14	Uracil-cyclopentane	0.10	(4.16)	–3.26	(0.80)	–2.59	(1.47)	–4.06
#15	Uracil-neopentane	–0.24	(3.41)	–3.29	(0.36)	1.72	(5.37)	–3.65
#16	Uracil-pentane	–0.33	(4.63)	–4.06	(0.90)	–4.32	(0.65)	–4.96
	MD		(2.29)		(0.18)		(0.73)	
	MAD		(2.31)		(0.44)		(0.90)	

* Differences from the ground state are shown in parentheses.

Next, excitation-induced shifts of interaction energies in Table 4.5 are focused on. While the shifts of the π-π* interaction energies take both positive and negative values, most shifts of the n-π* interaction energies are positive. This is because the electron redistribution accompanied by the n-π* transition is considerably larger than that accompanied by the π-π* transition and it destabilizes the intermolecular interaction. Especially in the pyridine-MeOH and pyridine-water complexes, largely positive shifts were obtained due to the loss of an electron at the nitrogen atom, which serves as an acceptor in the hydrogen bond. The LRD method provides small negative effects on the interaction energy shifts. Satisfactory agreement between the TD-LC-BOP(+LRD) approach and the reference was confirmed. From these results, the TD-LC-BOP+LRD approach was found to be effective in describing excited-state interaction energies and their shifts from the ground state.

Table 4.5. π-π* and n-π* excitation-induced interaction energy shifts of 16 molecular complexes from the S66 benchmark set (in kcal/mol).

		π-π* excitation				n-π* excitation			
		TD-LC-BOP	TD-LC-BOP +LRD	CIS(D)	Est. EOM-CCSD(T)	TD-LC-BOP	TD-LC-BOP +LRD	CIS(D)	Est. EOM-CCSD(T)
#1	$AcNH_2$-pentane					0.68	0.67	0.17	0.77
#2	AcOH-pentane					–0.07	–0.08	–0.60	–0.12
#3	Benzene-$MeNH_2$	0.29	0.26	0.25	0.40				
#4	Benzene-MeOH	0.47	0.45	0.50	0.68				
#5	Benzene-cyclopentane	0.02	–0.01	–0.20	0.06				
#6	Benzene-neopentane	–0.05	–0.08	–0.22	–0.01				
#7	Benzene-water	0.44	0.43	0.52	0.62				
#8	Peptide-$MeNH_2$					0.65	0.62	0.62	0.74
#9	Peptide-pentane					0.19	0.18	–0.40	0.19
#10	Peptide-water					0.49	0.47	0.58	0.57
#11	Pyridine-$MeNH_2$	–0.29	–0.31	–0.15	–0.22	1.29	1.26	0.64	1.30
#12	Pyridine-MeOH	–0.39	–0.39	–0.15	–0.19	6.00	5.97	5.11	5.94
#13	Pyridine-water	–0.37	–0.37	–0.14	–0.18	6.29	6.27	5.45	6.35
#14	Uracil-cyclopentane	–0.43	–0.47	–2.08	–0.43	0.14	0.12	1.16	0.03
#15	Uracil-neopentane	–0.32	–0.36	–5.75	–0.51	0.13	0.12	4.98	0.04
#16	Uracil-pentane	–0.45	–0.46	–1.15	–0.54	–0.04	–0.06	0.01	–0.15

4.4.2 Exciton-resonance systems

The spectroscopic parameters shown in Figure 4.3 were calculated with respect to sandwich dimers of benzene, cytosine, and adenine using the LC-BOP functional and the LRD method.

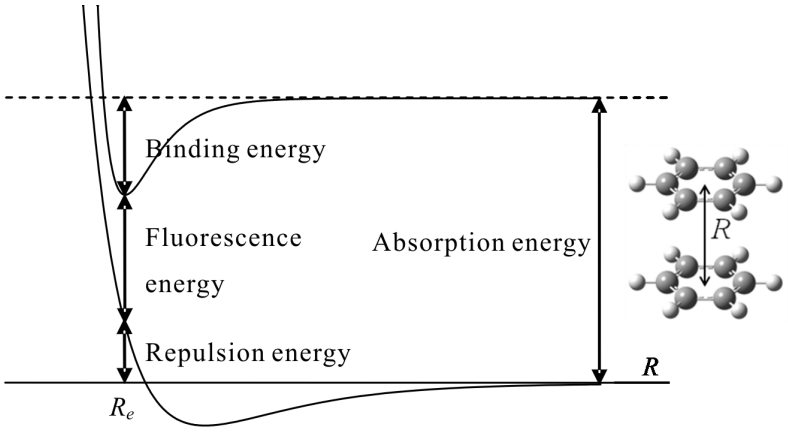

Figure 4.3. Schematic diagram of the potential energy curves of an aromatic dimer in the ground and excited states with spectroscopic parameters.

Note that at the dissociation limit, one molecule is in the lowest π-π* excited state and the other is in the ground state. Geometries of monomers were optimized at the LC-BOP/6-31G(d,p) level. D_{6h} symmetry was imposed on the benzene dimer, and C_s symmetry was imposed on the cytosine and adenine dimers. For all theoretical methods, BSSEs of the binding and repulsion energies were corrected by the CP method. The binding energy was calculated using the following formula:

$$\Delta E_{\mathrm{TDDFT(+LRD)}}[(AA)^*] = E^{\alpha\cup\beta}_{\mathrm{TDDFT(+LRD)}}[A^*] + E^{\alpha\cup\beta}_{\mathrm{DFT(+LRD)}}[A] - E^{\alpha\cup\beta}_{\mathrm{TDDFT(+LRD)}}[(AA)^*]. \quad (4.30)$$

This is equivalent to Eq. (4.27) in principle, except that the sign is reversed.

The results are summarized in Table 4.6. Previously reported values based on *ab initio* calculations [75-78] are also listed for comparison. In terms of the equilibrium distance R_e, TD-LC-BOP is similar to *ab initio* calculations, and the LRD method does not change R_e. Without the dispersion correction, the binding energy is underestimated, which was also confirmed in the previous TDDFT calculation of the cytosine excimer [29]. The LRD method increases the binding energy and decreases the repulsion energy. The accuracy of these quantities is improved by the dispersion correction, although the delocalization of an exciton and the charge-transfer interaction are thought to be dominant interaction components in aromatic excimers. It was found that the dispersion correction at a shorter intermolecular distance compared to the ground state was important in determining the binding and repulsion energies. The absorption and fluorescence energies decrease slightly because the dispersion correction energy in the excited state is larger than that in the ground state. This tendency was also observed in the exciton-localized systems. In conclusion, the LC-BOP+LRD approach is effective in describing not only ground-state molecular complexes but also excited-state ones including aromatic excimers.

Table 4.6. Spectroscopic parameters of aromatic excimers estimated by the TDDFT(+LRD) approach and high-level *ab initio* theories.

	Basis set	R_e (Å)	Binding (eV)	Repulsion (eV)	Absorption (eV)	Fluorescence (eV)	Ref.
Benzene dimer							
TD-LC-BOP	6-311++G(2d,2p)	3.06	0.31	0.64	5.46	4.51	this work
TD-LC-BOP+LRD	6-311++G(2d,2p)	3.06	0.54	0.42	5.46	4.50	this work
CASPT2	ANO (C[4s3d2p]/H[3s2p])	3.05	0.43	0.39	4.98	4.16	[71]
CCSDR(3)	extrapolated aug-cc-pVQZ	3.05	0.50	0.34	5.07	4.22	[72]
Cytosine dimer							
TD-LC-BOP	6-31++G(d,p)	3.06	0.17	0.76	5.04	4.11	this work
TD-LC-BOP+LRD	6-31++G(d,p)	3.06	0.44	0.50	5.03	4.09	this work
CASPT2	ANO (C,N,O[3s2d1p]/H[2s1p])	3.08	0.58	0.43	4.41	3.40	[73]
Adenine dimer							
TD-LC-BOP	6-31++G(d,p)	3.12	0.35	0.57	5.44	4.52	this work
TD-LC-BOP+LRD	6-31++G(d,p)	3.12	0.71	0.22	5.43	4.50	this work
CASPT2	ANO (C,N[3s2d1p]/H[2s1p])	3.06	0.83	0.28	5.25	4.14	[74]

* The CP correction is applied to the calculation of binding and repulsion energies.

4.5. Conclusion

In this chapter, the LRD method was extended to the TDDFT excited-state calculation. The state-specific dispersion correction energy was calculated using the difference density matrix, which is usually used to calculate excited-state response properties. Numerical assessments were performed for exciton-localized and exciton-resonance systems. For the exciton-localized systems, the TD-LC-BOP+LRD approach adequately reproduced the reference interaction energies and their shifts from the ground state. The LRD method was also required to reproduce the binding energy of the excimer state, even though the exciton delocalization and the charge-transfer interaction played a dominant role in stabilizing an aromatic excimer. In conclusion, the LC-BOP+LRD method is useful in describing not only ground-state molecular complexes but also those in the excited state.

References

[1] M. E. Casida, *Recent Advances in Density Functional Methods*, edited by D. P. Chong (World Scientific, Singapore, 1995), Vol. 1, p. 155.

[2] R. Bauernschmitt, R. Ahlrichs, *Chem. Phys. Lett.* **256**, 454 (1996).

[3] R. E. Stratmann, G. E. Scuseria, M. J. Frisch, *J. Chem. Phys.* **109**, 8218 (1998).

[4] H. Sekino, R. J. Bartlett, *J. Chem. Phys.* **85**, 976 (1986).

[5] S. J. A. van Gisbergen, J. G. Snijders, E. J. Baerends, *J. Chem. Phys.* **103**, 9347 (1995).

[6] S. J. A. van Gisbergen, J. G. Snijders, E. J. Baerends, *J. Chem. Phys.* **109**, 10644 (1998).

[7] K. Yabana, G. Bertsch, *Phys. Rev. B* **54**, 4484 (1996).

[8] O. Sugino, Y. Miyamoto, *Phys. Rev. B* **59**, 2579 (1999).

[9] K. Yabana, G. Bertsch, *Int. J. Quantum Chem.* **75**, 55 (1999).

[10] M. E. Casida, D. R. Salahub, *J. Chem. Phys.* **113**, 8918 (2000).

[11] F. Appel, E. K. U. Gross, K. Burke, *Phy. Rev. Lett.* **90**, 043005 (2003).

[12] A. Dreuw, J. L. Weisman, M. Head-Gordon, *J. Chem. Phys.* **119**, 2943 (2003).

[13] Y. Imamura, T. Otsuka, H. Nakai, *J. Comput. Chem.* **28**, 2067 (2007).

[14] Y. Imamura, H. Nakai, *Int. J. Quant. Chem.* **107**, 23 (2007).

[15] Y. Tawada, T. Tsuneda, S. Yanagisawa, T. Yanai, K. Hirao, *J. Chem. Phys.* **120**, 8425 (2004).

[16] T. Yanai, D. P. Tew, N. C. Handy, *Chem. Phys. Lett.* **393**, 51 (2004).

[17] A. Nakata, Y. Imamura, T. Otsuka, H. Nakai, *J. Chem. Phys.* **124**, 094105 (2006).

[18] A. Nakata, Y. Imamura, H. Nakai, *J. Chem. Phys.* **125**, 064109 (2006).

[19] A. Nakata, Y. Imamura, H. Nakai, *J. Chem. Theory Comput.* **3**, 1295 (2007).

[20] Z. Cai, J. R. Reimers, *J. Phys. Chem. A* **106**, 8769 (2002).

[21] Z. Cai, J. R. Reimers, *J. Phys. Chem. A* **109**, 1576 (2005).

[22] Z. Cai, J. R. Reimers, *J. Phys. Chem. A* **111**, 954 (2007).

[23] M. Biczysko, G. Piani, M. Pasquini, N. Schiccheri, G. Pietraperzia, M. Bucci, M. Pavone, V. Barone, *J. Chem. Phys.* **127**, 144303 (2007).

[24] V. Barone, M. Biczysko, M. Pavone, *Chem. Phys.* **346**, 247 (2008).

[25] M. Pasquini, N. Schiccheri, G. Piani, G. Pietraperzia, M. Becucci, M. Biczysko, M. Pavone, V. Barone, *J. Phys. Chem. A* **111**, 12363 (2007).

[26] J. C. Amicangelo, *J. Phys. Chem. A* **109**, 9174 (2005).

[27] R. Huenerbein, S. Grimme, *Chem. Phys.* **343**, 362 (2008).

[28] R. F. Fink, J. Pfister, H. M. Zhao, B. Engels, *Chem. Phys.* **346**, 275 (2008).

[29] F. Santoro, V. Barone, R. improta, *J. Comput. Chem.* **29**, 957 (2007).

[30] R. Improta, *Phys. Chem. Chem. Phys.* **10**, 2656 (2008).

[31] A. W. Lange, M. A. Rohrdanz, J. M. Herbert, *J. Phys. Chem. B* **112**, 6304 (2008).

[32] F. Santoro, V. Barone, R. Improta, *J. Am. Chem. Soc.* **131**, 15232 (2009).

[33] F. Santoro, V. Barone, A. Lami, R. Improta, *Phys. Chem. Chem. Phys.* **12**, 4934 (2010).

[34] M. Kamiya, *J. Comput. Aid. Chem.* **11**, 25 (2010).

[35] W. Liu, V. Settels, P. H. P. Harbach, A. Dreuw, R. F. Fink, B. Engels, *J. Comput. Chem.* **32**, 1971 (2011).

[36] Q. Wu, W. Yang, *J. Chem. Phys.* **116**, 515 (2002).

[37] S. Grimme, *J. Comput. Chem.* **25**, 1463 (2004).

[38] S. Grimme, *J. Comput. Chem.* **27**, 1787 (2006).

[39] S. Grimme, J. Antony, S. Ehrlich, H. Krieg, *J. Chem. Phys.* **132**, 154104 (2010).

[40] A. D. Becke, E. R. Johnson, *J. Chem. Phys.* **127**, 154108 (2007).

[41] S. N. Steinmann, C. Corminboeuf, *J. Chem. Theory Comput.* **7**, 3567 (2011).

[42] Y. Andersson, D. C. Langreth, B. I. Lundqvist, *Phys. Rev. Lett.* **76**, 102 (1996)

[43] M. Dion, H. Rydberg, E. Schröder, D. C. Langreth, B. I. Lundqvist, *Phys. Rev. Lett.* **92**, 246401 (2004).

[44] O. A. Vydrov, T. Van Voorhis, *J. Chem. Phys.* **133**, 244103 (2010).

[45] T. Sato, H. Nakai, *J. Chem. Phys.* **131**, 224104 (2009).

[46] T. Sato, H. Nakai, *J. Chem. Phys.* **133**, 194101 (2010).

[47] W. Barford, N. Paiboonvorachat, D. Yaron, *J. Chem. Phys.* **134**, 234101 (2011).

[48] J. F. Dobson, B. P. Dinte, *Phys. Rev. Lett.* **76**, 1780 (1996).

[49] A. D. Becke, *J. Chem. Phys.* **88**, 2547 (1988).

[50] C. Van Caillie, R. D. Amos, *Chem. Phys. Lett.* **317**, 159 (2000).

[51] F. Furche, R. Ahlrichs, *J. Chem. Phys.* **117**, 7433 (2002).

[52] H. Iikura, T. Tsuneda, T. Yanai, K. Hirao, *J. Chem. Phys.* **115**, 3540 (2001).

[53] A. D. Becke, *Phys. Rev. A* **38**, 3098 (1988).

[54] T. Tsuneda, T. Suzumura, K. Hirao, *J. Chem. Phys.* **110**, 10664 (1999).

[55] A. Kumur, W. J. Meath, *Mol. Phys.* **54**, 823 (1985).

[56] T. J. Giese, V. M. Audette, D. M. York, *J. Chem. Phys.* **119**, 2618 (2003).

[57] M. W. Schmidt *et al.*, *J. Comput. Chem.* **14**, 1347 (1993).

[58] M. Head-Gordon, R. J. Rico, M. Oumi, T. J. Lee, *Chem. Phys. Lett.* **219**, 21 (1994).

[59] J. F. Stanton, R. J. Bartlett, *J. Chem. Phys.* **98**, 7029 (1993).

[60] M. J. Frisch, G. W. Trucks, H. B. Schlegel *et al.*, Gaussian 09, Revision C.01, Gaussian, Inc., Wallingford, CT, 2010.

[61] J. Řezáč, K. E. Riley, P. Hobza, *J. Chem. Theory Comput.* **7**, 2427 (2011).

[62] J. Řezáč, K. E. Riley, P. Hobza, *J. Chem. Theory Comput.* **7**, 3466 (2011).

[63] R. Krishnan, J. S. Binkley, R. Seeger J. A. Pople, *J. Chem. Phys.* **72**, 650 (1980).

[64] M. J. Frisch, J. A. Pople J. S. Binkley, *J. Chem. Phys.* **80**, 3265 (1984).

[65] T. Clark, J. Chandrasekhar, G. W. Spitznagel, P. V. R. Schleyer, *J. Comput. Chem.* **4**, 294 (1983).

[66] S. F. Boys, F. Bernardi, *Mol. Phys.* **19**, 553 (1970).

[67] S. S. Xantheas, *J. Chem. Phys.* **104**, 8821 (1996).

[68] B. Fernández, H. Koch, J. Makarewicz, *J. Chem. Phys.* **111**, 5922 (1999).

[69] J. L. C. Fajín, B. Fernández, P. M. Felker, *J. Phys. Chem. A* **110**, 13259 (2006).

[70] J. L. Fajín, S. B. Capelo, B. Fernandez, P. M. Felker, *J. Phys. Chem. A* **111**, 7876 (2007).

[71] W. J. Hehre, R. Ditchfield, J. A. Pople, *J. Chem. Phys.* **56**, 2257 (1972).

[72] P. C. Hariharan, J. A. Pople, *Theor. Chim. Acta* **28**, 213 (1973).

[73] N. G. Barkhshiev, O. P. Girinand, I. V. Piterskaya, *Opt. Spectrosc.* **24**, 483 (1968).

[74] O. Christiansen, C. Hättig, P. Jørgensen, *Spectrochimica Acta Part A* **55**, 509 (1999).

[75] T. Rocha-Rinza, L. D. Vico, V. Veryazov, B. O. Roos, *Chem. Phys. Lett.* **426**, 268 (2006).

[76] T. Rocha-Rinza, O. Christiansen, *Chem. Phys. Lett.* **482**, 44 (2009).

[77] G. Olaso-González, D. Roca-Sanjuán, L. Serrano-Andrés, M. Merchán, *J. Chem. Phys.* **125**, 23112 (2006).

[78] G. Olaso-González, M. Merchán, L. Serrano-Andrés, *J. Am. Chem. Soc.* **131**, 4368 (2009).

Part 2

Non-Born-Oppenheimer Wave Function Theory Study on Isotope Effect in Noncovalent Interaction

Chapter 5
Theoretical Background

One of the problems in WFT is the difficulty in estimating nuclear quantum effects and isotope effects, which are important in protonic interactions such as the hydrogen bond. Almost all electronic structure calculations have been performed based on the BO approximation [1], which makes it difficult to obtain nuclear wavefunction. The NOMO method [2] has been developed as a computationally inexpensive non-BO WFT. In this Chapter, the treatment of electrons and nuclei under the BO approximation is explained besides the theory of the NOMO method.

5.1. Born-Oppenheimer approximation

A quantum mechanical theory for molecules deals with the (nonrelativistic) time-dependent and/or time-independent Schrödinger equations that involve the total .wavefunction of nuclei and electrons:

$$\hat{H}(\mathbf{r},\mathbf{R})\Psi(\mathbf{x},\mathbf{X},t) = i\frac{\partial}{\partial t}\Psi(\mathbf{x},\mathbf{X},t), \tag{5.1a}$$

$$\hat{H}(\mathbf{r},\mathbf{R})\Psi(\mathbf{x},\mathbf{X}) = E\Psi(\mathbf{x},\mathbf{X}), \tag{5.1b}$$

where $\mathbf{x}$ and $\mathbf{X}$ represent all coordinates of electrons and nuclei: $\{\mathbf{x}_1,\mathbf{x}_2,\cdots\} = \{\mathbf{r}_1,\omega_1,\mathbf{r}_2,\omega_2,\cdots\}$ and $\{\mathbf{X}_1,\mathbf{X}_2,\cdots\} = \{\mathbf{R}_1,\Omega_1,\mathbf{R}_2,\Omega_2,\cdots\}$, respectively. Here, $\mathbf{r} = \{\mathbf{r}_1,\mathbf{r}_2,\cdots\}$ and $\mathbf{R} = \{\mathbf{R}_1,\mathbf{R}_2,\cdots\}$ correspond to the spatial coordinates of electrons and nuclei, and $\boldsymbol{\omega} = \{\omega_1,\omega_2,\cdots\}$ and $\boldsymbol{\Omega} = \{\Omega_1,\Omega_2,\cdots\}$ to their spin coordinates.

The Hamiltonian is described as follows:

$$\hat{H}(\mathbf{r},\mathbf{R}) = -\sum_{P}^{N^{\mathrm{n}}}\frac{1}{2M_P}\nabla^2(\mathbf{R}_P) - \sum_{p}^{N^{\mathrm{e}}}\frac{1}{2}\nabla^2(\mathbf{r}_P) + \sum_{P<Q}^{N^{\mathrm{n}}}\frac{Z_P Z_Q}{R_{PQ}} - \sum_{P}^{N^{\mathrm{n}}}\sum_{p}^{N^{\mathrm{e}}}\frac{Z_P}{r_{Pp}} + \sum_{p<q}^{N^{\mathrm{e}}}\frac{1}{r_{pq}}$$

$$\equiv \sum_{P}^{N^{\mathrm{n}}} \hat{t}_P^{\mathrm{n}} + \sum_{p}^{N^{\mathrm{e}}} \hat{t}_p^{\mathrm{e}} + \sum_{P<Q}^{N^{\mathrm{n}}} \hat{v}_{PQ}^{\mathrm{nn}} + \sum_{P}^{N^{\mathrm{n}}} \sum_{p}^{N^{\mathrm{e}}} \hat{v}_{Pp}^{\mathrm{ne}} + \sum_{p<q}^{N^{\mathrm{e}}} \hat{v}_{pq}^{\mathrm{ee}}$$

$$\equiv \hat{T}^{\mathrm{n}}(\mathbf{R}) + \hat{T}^{\mathrm{e}}(\mathbf{r}) + \hat{V}^{\mathrm{nn}}(\mathbf{R}) + \hat{V}^{\mathrm{ne}}(\mathbf{r},\mathbf{R}) + \hat{V}^{\mathrm{ee}}(\mathbf{r}), \tag{5.2}$$

where $\hat{T}^{\mathrm{n}}$ and $\hat{T}^{\mathrm{e}}$ are nuclear and electronic kinetic operators, and $\hat{V}^{\mathrm{nn}}$, $\hat{V}^{\mathrm{ne}}$, and $\hat{V}^{\mathrm{ee}}$ are n-n, n-e, and e-e Coulomb operators, respectively. N^{e} and N^{n} mean the numbers of electrons and nuclei. The subscripts of $\{p,q\}$ and $\{P,Q\}$ run over all electrons and nuclei, respectively.

In the BO treatment, the electronic Hamiltonian is first defined by,

$$\hat{H}^{\mathrm{e}}(\mathbf{r},\mathbf{R}) = \hat{T}^{\mathrm{e}}(\mathbf{r}) + \hat{V}^{\mathrm{nn}}(\mathbf{R}) + \hat{V}^{\mathrm{ne}}(\mathbf{r},\mathbf{R}) + \hat{V}^{\mathrm{ee}}(\mathbf{r}). \tag{5.3}$$

Note that $\hat{V}^{\mathrm{nn}}$ and $\hat{V}^{\mathrm{ne}}$ include the nuclear coordinates. Since the time scale of the nuclear motion is assumed to be sufficiently slower than that of electronic motion due to the remarkable difference of their masses, the electronic .wavefunction might be determined by solving the time-independent electronic Schrödinger equation with a fixed nuclear configuration,

$$\hat{H}^{\mathrm{e}}(\mathbf{r};\mathbf{R})\Phi_m^{\mathrm{e}}(\mathbf{x};\mathbf{X}) = E_m^{\mathrm{e}}(\mathbf{R})\Phi_m^{\mathrm{e}}(\mathbf{x};\mathbf{X}), \tag{5.4}$$

where the subscript *m* identifies the electronic state.

The total .wavefunction, $\Psi(\mathbf{x},\mathbf{X},t)$ or $\Psi(\mathbf{x},\mathbf{X})$ in Eq. (5.1) can be expanded in terms of the eigenfunctions of $\hat{H}^{\mathrm{e}}$ as follows:

$$\Psi(\mathbf{x},\mathbf{X},t) = \sum_m \Phi_m^{\mathrm{e}}(\mathbf{x};\mathbf{X})\Phi_m^{\mathrm{n}}(\mathbf{X},t), \tag{5.5a}$$

$$\Psi(\mathbf{x},\mathbf{X}) = \sum_m \Phi_m^{\mathrm{e}}(\mathbf{x};\mathbf{X})\Phi_m^{\mathrm{n}}(\mathbf{X}). \tag{5.5b}$$

The function for the expansion, $\Phi_m^{\mathrm{n}}(\mathbf{X},t)$ or $\Phi_m^{\mathrm{n}}(\mathbf{X})$, corresponds to the nuclear .wavefunction.

Inserting Eq. (5.5) into Eq. (5.1), a set of coupled differential equations for the nuclear .wavefunction is derived:

$$[\hat{T}^{\mathrm{n}}(\mathbf{R})+E_m^{\mathrm{e}}(\mathbf{R})]\Phi_m^{\mathrm{n}}(\mathbf{X},t)+\sum_n C_{mn}\Phi_n^{\mathrm{n}}(\mathbf{X},t)=i\frac{\partial}{\partial t}\Phi_m^{\mathrm{n}}(\mathbf{X},t)\,, \tag{5.6a}$$

$$[\hat{T}^{\mathrm{n}}(\mathbf{R})+E_m^{\mathrm{e}}(\mathbf{R})]\Phi_m^{\mathrm{n}}(\mathbf{X})+\sum_n C_{mn}\Phi_n^{\mathrm{n}}(\mathbf{X})=E_m^{\mathrm{n}}\Phi_m^{\mathrm{n}}(\mathbf{X})\,. \tag{5.6b}$$

Here, C_{mn} is a coupling term defined as follows:

$$C_{mn}=\left\langle\Phi_m^{\mathrm{e}}(\mathbf{x};\mathbf{X})\middle|\hat{T}^{\mathrm{n}}(\mathbf{R})\middle|\Phi_n^{\mathrm{e}}(\mathbf{x};\mathbf{X})\right\rangle-2\sum_P\left\langle\Phi_m^{\mathrm{e}}(\mathbf{x};\mathbf{X})\middle|\hat{\tau}_P^{\mathrm{n}}\middle|\Phi_n^{\mathrm{e}}(\mathbf{x};\mathbf{X})\right\rangle\cdot\hat{\tau}_P^{\mathrm{n}}\,, \tag{5.7}$$

where

$$\hat{\tau}_P^{\mathrm{n}}=\sqrt{\frac{1}{2M_P}}\nabla(\boldsymbol{R}_P)\,. \tag{5.8}$$

Then,

$$\hat{\tau}_P^{\mathrm{n}}\cdot\hat{\tau}_P^{\mathrm{n}}=-\hat{t}_P^{\mathrm{n}}\,. \tag{5.9}$$

Note that no approximation is introduced to derive Eq. (5.6).

When neglecting all the coupling terms C_{mn}, namely,

$$C_{mn}=0\,, \tag{5.10}$$

Eq. (5.6) becomes

$$[\hat{T}^{\mathrm{n}}(\mathbf{R})+E_m^{\mathrm{e}}(\mathbf{R})]\Phi_m^{\mathrm{n}}(\mathbf{X},t)=i\frac{\partial}{\partial t}\Phi_m^{\mathrm{n}}(\mathbf{X},t)\,, \tag{5.11a}$$

$$[\hat{T}^{\mathrm{n}}(\mathbf{R})+E_m^{\mathrm{e}}(\mathbf{R})]\Phi_m^{\mathrm{n}}(\mathbf{X})=E_m^{\mathrm{n}}\Phi_m^{\mathrm{n}}(\mathbf{X})\,. \tag{5.11b}$$

In this case, the total .wavefunction is given by

$$\Psi(\mathbf{x},\mathbf{X},t) = \Phi_m^{\mathrm{e}}(\mathbf{x};\mathbf{X})\Phi_m^{\mathrm{n}}(\mathbf{X},t)\,, \tag{5.12a}$$

$$\Psi(\mathbf{x},\mathbf{X}) = \Phi_m^{\mathrm{e}}(\mathbf{x};\mathbf{X})\Phi_m^{\mathrm{n}}(\mathbf{X})\,. \tag{5.12b}$$

The approximation in Eq. (5.10) corresponds to the BO approximation. In this treatment, the nuclear motion can be determined by a single electronic state.

If the diagonal term C_{mm} is taken into account,

$$C_{mn} = 0 \quad (m \neq n), \quad C_{mm} = \left\langle \Phi_m^{\mathrm{e}}(\mathbf{x};\mathbf{X}) \middle| \hat{T}^{\mathrm{n}}(\mathbf{R}) \middle| \Phi_m^{\mathrm{e}}(\mathbf{x};\mathbf{X}) \right\rangle \equiv U_m^{\mathrm{n}}(\mathbf{R})\,, \tag{5.13}$$

the following equations are derived:

$$[\hat{T}^{\mathrm{n}}(\mathbf{R}) + E_m^{\mathrm{e}}(\mathbf{R}) + U_m^{\mathrm{n}}(\mathbf{R})]\Phi_m^{\mathrm{n}}(\mathbf{X},t) = i\frac{\partial}{\partial t}\Phi_m^{\mathrm{n}}(\mathbf{X},t)\,, \tag{5.14a}$$

or

$$[\hat{T}^{\mathrm{n}}(\mathbf{R}) + E_m^{\mathrm{e}}(\mathbf{R}) + U_m^{\mathrm{n}}(\mathbf{R})]\Phi_m^{\mathrm{n}}(\mathbf{X}) = E_m^{\mathrm{n}}\Phi_m^{\mathrm{n}}(\mathbf{X})\,. \tag{5.14b}$$

The treatment in Eq. (5.13) is called the adiabatic approximation in distinction from the BO approximation. The total wavefunction is given by the same formula as Eq. (5.12). The energy contribution due to $U_m^{\mathrm{n}}(\boldsymbol{R})$ is occasionally called the diagonal BO correction term, which represents the coupling between the electronic and nuclear motions within the adiabatic approximation.

The BO approximation derives the individual working equation for the electronic and nuclear motions, i.e. Eqs. (5.4) and (5.11), respectively. The electronic structure theory such as WFT and DFT handles Eq. (5.4). Furthermore, this separation enables to treat the nuclear motion classically. For example, one can solve the Newton's

equation-of-motion,

$$-\frac{\partial E_m^{\mathrm{n}}(\mathbf{R})}{\partial \mathbf{R}_P} = M_P \frac{\partial^2 \mathbf{R}_P}{\partial t^2}, \tag{5.15}$$

instead of the nuclear Schrödinger equation (5.11a). This treatment corresponds to the molecular dynamics simulation, in which nuclei are expressed by classical charged particles.

5.2. Nuclear orbital plus molecular orbital method

Here, one-particle .wavefunctions of a nucleus and an electron are introduced. In the standard quantum chemistry, the one-particle .wavefunction of an electron in a molecule is called MO. Similarly, the one-particle .wavefunction of a nucleus is named NO. Since electrons are fermionic particles, N^{e}-electron .wavefunction is given by antisymmetric product of the MOs. On the contrary, N^{n}-nucleus .wavefunctions are given by antisymmetric and symmetric products of the NOs for fermionic and bosonic nucleus, respectively. For example, a reference state Φ_0 can be described by a simple product of N^{e}-electron and N^{n}-nucleus .wavefunctions as follows:

$$\Phi_0 = \Phi_0^{\mathrm{n}} \cdot \Phi_0^{\mathrm{e}}, \tag{5.16}$$

$$\Phi_0^{\mathrm{n}} = \left\| \varphi_I \varphi_J \cdots \varphi_K \right\|, \tag{5.17}$$

$$\Phi_0^{\mathrm{e}} = \left\| \varphi_i \varphi_j \cdots \varphi_k \right\|. \tag{5.18}$$

The subscripts $\{I, J, \ldots, K\}$ and $\{i, j, \ldots, k\}$ are the labels for expressing occupied NOs and MOs, respectively. The notations $\{A, B, \ldots, C\}$ and $\{a, b, \ldots, c\}$ are used for unoccupied NOs and MOs, respectively.

This section introduces the NOMO/HF method [2,3], which gives the HF

equations to determine both NOs and MOs for the Hamiltonian in Eq. (5.2). Using Lagrange's method of undetermined multipliers, one therefore minimizes the following functional,

$$\mathcal{L} = \langle \Phi_0 | \hat{H} | \Phi_0 \rangle - \sum_{I,J}^{N^{\mathrm{n}}} \varepsilon_{IJ} \left(\langle \varphi_I | \varphi_J \rangle - \delta_{IJ} \right) - \sum_{i,j}^{N^{\mathrm{e}}} \varepsilon_{ij} \left(\langle \varphi_i | \varphi_j \rangle - \delta_{ij} \right). \tag{5.19}$$

As a result, NOMO/HF equations are derived as follows:

$$\hat{f}^{\mathrm{n}}_{\mathrm{NOMO}} \varphi_I = \varepsilon_I \varphi_I , \tag{5.20}$$

$$\hat{f}^{\mathrm{e}}_{\mathrm{NOMO}} \varphi_i = \varepsilon_i \varphi_i , \tag{5.21}$$

$$\hat{f}^{\mathrm{n}}_{\mathrm{NOMO}} = \hat{t}^{\mathrm{n}} + \sum_{I}^{\mathrm{nuc}} \left(\hat{J}_I \mp \hat{K}_I \right) + \sum_{i}^{\mathrm{elec}} \hat{J}_i \equiv \hat{t}^{\mathrm{n}} + \hat{v}^{\mathrm{n}} , \tag{5.22}$$

$$\hat{f}^{\mathrm{e}}_{\mathrm{NOMO}} = \hat{t}^{\mathrm{e}} + \sum_{i}^{\mathrm{elec}} \left(\hat{J}_i - \hat{K}_i \right) + \sum_{I}^{\mathrm{nuc}} \hat{J}_I \equiv \hat{t}^{\mathrm{e}} + \hat{v}^{\mathrm{e}} . \tag{5.23}$$

Here, $\hat{J}$ and $\hat{K}$ are Coulomb and exchange operators, respectively. In Eq. (5.22), the minus and plus signs are used for fermionic and bosonic nuclei, respectively. The Fock operator includes mean-field type of coupling between NOs and MOs. This is similar to the unrestricted HF scheme. The extension from the MO/HF method to the NOMO/HF method is straightforward. Actually, the NOMO/HF .wavefunction satisfies Koopmans' theorem and Brillouin's theorem. Therefore, various correlated methods developed within the BO approximation are applicable to the NOMO model.

Next, let us discuss the expansion of NOs. In the conventional MO method, the usage of GTFs for expanding MOs has been accepted since Boys' proposal [4] because it has computational merits such as evaluation of four-center integrals. It is opposite to the fact that the exact .wavefunctions of hydrogen-like atoms are STFs. Then, how should the NOs be expanded? Most parts of nuclear .wavefunctions correspond to the vibrational motion: that is, $3N^{\mathrm{n}}$-6 degrees of freedom. The exact .wavefunction of the

harmonic oscillator is the product of a hermitian polynomial and a GTF. Thus, it might be reasonable to think that the GTFs are used as the basis functions to expand the NOs. In particular, the exponents of the GTFs are directly connected with the vibrational frequencies. A simple scheme has been proposed in order to determine the NBFs by this relationship [3].

In the conventional MO method, the deviation between the HF and full-CI calculations is due to the electron correlation effect. On the other hand, in the NOMO formalism, the deviation is originated from electron-electron (*e*-*e*), electron-nucleus (*e*-*n*) and nucleus-nucleus (*n*-*n*) correlations. The MP2 perturbation theory for the NOMO method was formulated to consider these correlations [2,5,6].

As in the case of conventional perturbation theory, the Hamiltonian $\hat{H}$ is partitioned into the unperturbed part $\hat{H}^0$, for which the HF Hamiltonian is used, and the perturbation $\hat{\Omega}$.

$$\hat{H} = \hat{H}^0 + \hat{\Omega}, \tag{5.24}$$

$$\begin{aligned}\hat{H}^0 &= \sum_P \hat{f}^{\mathrm{n}}(\mathbf{r}_P) + \sum_p \hat{f}^{\mathrm{e}}(\mathbf{r}_p) \\ &= \sum_P \hat{t}^{\mathrm{n}}(\mathbf{r}_P) + \sum_p \hat{t}^{\mathrm{e}}(\mathbf{r}_p) + \sum_\mu \hat{v}(\mathbf{r}_\mu),\end{aligned} \tag{5.25}$$

$$\hat{\Omega} = \sum_{\mu<\nu} r_{\mu\nu}^{-1} - \sum_\mu \hat{v}(\mathbf{r}_\mu) \quad . \tag{5.26}$$

where $\hat{v}(\mathbf{r}_\mu)$ in Eq. (5.26) represents NOMO/HF potential for μth particle.

By the definition of Møller-Plesset perturbation theory, the NOMO/MP2 energy expression is written by

$$\Delta E_{\mathrm{corr}} = \Delta E_{\mathrm{ee}} + \Delta E_{\mathrm{en}} + \Delta E_{\mathrm{nn}}, \tag{5.27}$$

where

$$\Delta E_{\mathrm{ee}} = \sum_{i<j,a<b} \frac{\left| \left\langle \Phi_0 \left| \hat{\Omega}_{\mathrm{ee}} \right| \Phi_{ij}^{ab} \right\rangle \right|^2}{\varepsilon_i + \varepsilon_j - \varepsilon_a - \varepsilon_b}, \tag{5.28}$$

$$\Delta E_{\mathrm{en}} = \sum_{i,I,a,A} \frac{\left|\left\langle \Phi_0 \left| \hat{\Omega}_{\mathrm{en}} \right| \Phi_{iI}^{aA} \right\rangle\right|^2}{\varepsilon_i + \varepsilon_I - \varepsilon_a - \varepsilon_A}, \tag{5.29}$$

$$\Delta E_{\mathrm{nn}} = \sum_{I<J,A<B} \frac{\left|\left\langle \Phi_0 \left| \hat{\Omega}_{\mathrm{nn}} \right| \Phi_{IJ}^{AB} \right\rangle\right|^2}{\varepsilon_I + \varepsilon_J - \varepsilon_A - \varepsilon_B}. \tag{5.30}$$

Here, ΔE_{ee}, ΔE_{en}, and ΔE_{nn} correspond to *e-e*, *e-n*, and *n-n* many-body effects. The subscripts *i*, *j* (*I*, *J*) and *a*, *b* (*A*, *B*) represent electronic (nuclear) occupied and virtual orbitals, respectively. While Φ_0 denotes the NOMO/HF .wavefunction, Φ_{ij}^{ab}, Φ_{iI}^{aA}, and Φ_{IJ}^{AB} correspond to the two-particle excitation configurations. The NOMO/MP1 .wavefunction $\Psi_{\mathrm{NOMO/MP1}}$ is defined as follows:

$$\left|\Psi_{\mathrm{NOMO/MP1}}\right\rangle = \left|\Phi_0\right\rangle + \sum_{i<j,a<b} \left|\Phi_{ij}^{ab}\right\rangle \frac{\left\langle \Phi_{ij}^{ab} \left| \hat{\Omega}_{\mathrm{ee}} \right| \Phi_0 \right\rangle}{\varepsilon_i + \varepsilon_j - \varepsilon_a - \varepsilon_b} + \sum_{i,I,a,A} \left|\Phi_{iI}^{aA}\right\rangle \frac{\left\langle \Phi_{iI}^{aA} \left| \hat{\Omega}_{\mathrm{en}} \right| \Phi_0 \right\rangle}{\varepsilon_i + \varepsilon_I - \varepsilon_a - \varepsilon_A}$$

$$+ \sum_{I<J,A<B} \left|\Phi_{IJ}^{AB}\right\rangle \frac{\left\langle \Phi_{IJ}^{AB} \left| \hat{\Omega}_{\mathrm{nn}} \right| \Phi_0 \right\rangle}{\varepsilon_I + \varepsilon_J - \varepsilon_A - \varepsilon_B}. \tag{5.31}$$

References

[1] M. Born, R. Oppenheimer, *R. Ann. Phys.* **84**, 457 (1927).

[2] H. Nakai, *Int. J. Quant. Chem.* **86**, 511 (2002).

[3] H. Nakai, *Int. J. Quant. Chem.* **107**, 2849 (2007).

[4] S. F. Boys, *Proc. R. Soc. London Ser. A* **200**, 542 (1950).

[5] H. Nakai, K. Sodeyama, *J. Chem. Phys.* **118**, 1119 (2003).

[6] M. Hoshino, H. Nakai, *J. Chem. Phys.* **124**, 194110 (2006).

Chapter 6
Interpretation of Geometric Isotope Effect in Hydrogen Bond

6.1. Introduction

The GIE, defined as geometric changes caused by isotopic substitution, has been investigated for various hydrogen-bonded systems. The GIE plays an essential role in the hydrogen bond because it may affect the entire bond structure and physical properties. In solid-state physics, shifts in the hydrogen bond length induced by deuteration have long been known as the Ubbelohde effect [1]. Ichikawa [2-5] and Sokolov [6] examined geometries of hydrogen-bonded ferroelectric materials in detail and discovered relations between the GIEs and drastic increases in phase-transition temperatures induced by deuteration. The GIEs in the liquid and gas phases have also been investigated by NMR [7-9], X-ray and neutron diffraction [10], and microwave spectroscopy [11-13]. Recently, the GIEs in hydrogen-bonded molecules were theoretically investigated with quantum-chemical calculations [14-23] and path-integral molecular dynamics [24].

Both theoretical and experimental studies [7-24] demonstrated the following trend of the GIE: in the hydrogen bond A-X···B (X = H and D), the intramolecular bond A-X shrinks and the intermolecular bond X···B elongates when X is changed from hydrogen to deuterium. The intramolecular bond shrinkage is ascribed to the fact that the anharmonicity of the adiabatic potential is reduced by the decrease in zero-point energy, whereas the origin of the intermolecular bond elongation has remained unclear. Because the intermolecular elongation cannot be explained by the anharmonicity, it is natural to consider the elongation as a secondary effect owing to the isotope effect in the proton-donor molecule.

The intermolecular elongation is expected to be interpreted by decomposing the intermolecular interaction into physical energy components such as electrostatic, exchange-repulsion, polarization, and charge-transfer interactions by using the energy decomposition methods [25-34]. For the energy analysis, the nuclear quantum effects need to be incorporated; the NOMO theory [35-40], which introduces the NO as well as

the MO, can be employed to estimate nuclear quantum effects. Similar or equivalent approaches have been reported [20,41-43], and these theories have been utilized successfully to study the isotope effect in intermolecular interactions [14-18,20-23,44].

In this chapter, the isotope effect on interaction energy components in hydrogen-bonded systems are investigated by the NOMO theory. The RVS-SCF method [29] is adopted as the energy decomposition method. The organization of this chapter is as follows. In the following section, the extension of the RVS-SCF method to the NOMO scheme is described. The computational details are then discussed, and the intermolecular bond elongation is interpreted according to the energy components. Finally, conclusions are presented.

6.2. Theoretical aspects

The RVS-SCF method based on the conventional MO procedure decomposes the interaction energy at the HF level $E_{\mathrm{INT}}^{\mathrm{MO/HF}}$ as follows:

$$E_{\mathrm{INT}}^{\mathrm{MO/HF}} = E_{\mathrm{ES}}^{\mathrm{RVS}} + E_{\mathrm{EX}}^{\mathrm{RVS}} + E_{\mathrm{PL}}^{\mathrm{RVS}} + E_{\mathrm{CT}}^{\mathrm{RVS}} + E_{\mathrm{RES}}^{\mathrm{RVS}}, \tag{6.1}$$

where E_{ES}, E_{EX}, E_{PL}, E_{CT}, and E_{RES} represent the energy components of electrostatic, exchange repulsion, polarization, charge-transfer interactions, and residual term, respectively. Although $E_{\mathrm{ES}}^{\mathrm{RVS}}$ and $E_{\mathrm{EX}}^{\mathrm{RVS}}$ are integrated in the original paper [29], it is convenient to treat them separately when analyzing hydrogen-bonded systems. Similarly, the interaction energy obtained by the NOMO/HF method [35,36], in which MOs and NOs are determined by the SCF procedure, can be decomposed into the same components as the MO method:

$$E_{\mathrm{INT}}^{\mathrm{NOMO/HF}} = E_{\mathrm{ES}}^{\mathrm{RVS}} + E_{\mathrm{EX}}^{\mathrm{RVS}} + E_{\mathrm{PL}}^{\mathrm{RVS}} + E_{\mathrm{CT}}^{\mathrm{RVS}} + E_{\mathrm{RES}}^{\mathrm{RVS}}. \tag{6.2}$$

Before defining each interaction component, an orbital interaction scheme is

introduced. As shown in Figure 6.1, the Fock matrix is constructed in the MO and NO spaces of constituent fragments and partitioned into ES, EX, PL, CT, and NR blocks. For simplicity, two fragments, namely, fragments I and II, with one quantum nucleus for each fragment are considered. The Fock matrix is expressed on the basis of occupied and virtual orbitals of fragments I and II, i.e., occ. (I), occ. (II), vir. (I), and vir. (II). Each energy component is obtained by zeroing out nonrelated off-diagonal blocks of the Fock matrix.

$E_{\mathrm{INT}}^{\mathrm{NOMO/HF}}$ is obtained by subtracting the sum of fragment energies $E_{\mathrm{I}} + E_{\mathrm{II}}$ from the energy of the combined system $E_{\mathrm{I+II}}$:

$$E_{\mathrm{INT}}^{\mathrm{NOMO/HF}} = E_{\mathrm{I+II}} - \{E_{\mathrm{I}} + E_{\mathrm{II}}\}. \tag{6.3}$$

$E_{\mathrm{ES}}^{\mathrm{RVS}}$ is obtained in the manner described by the KM analysis [25-27]:

$$E_{\mathrm{ES}}^{\mathrm{RVS}} = E_{\mathrm{I+II}}[\mathrm{ES}] - \{E_{\mathrm{I}} + E_{\mathrm{II}}\}. \tag{6.4}$$

In Eq. (6.4), only the diagonal blocks of the Fock matrix, namely, ES blocks, are retained to calculate $E_{\mathrm{I+II}}[\mathrm{ES}]$. Because ES blocks contain exchange integral terms, the differential overlap between the atomic orbitals of fragments I and II is set to zero in the calculation of $E_{\mathrm{I+II}}[\mathrm{ES}]$:

$$\chi_{\mu\in\mathrm{I}}^{\mathrm{e}}(\mathbf{r})\chi_{\nu\in\mathrm{II}}^{\mathrm{e}}(\mathbf{r}) = 0\,, \tag{6.5}$$

where χ_{μ}^{e} is the atomic orbital for electrons. $E_{\mathrm{EX}}^{\mathrm{RVS}}$ is defined as the energy shift induced by the inclusion of EX blocks:

$$E_{\mathrm{EX}}^{\mathrm{RVS}} = E_{\mathrm{I+II}}[\mathrm{ES+EX}] - E_{\mathrm{I+II}}[\mathrm{ES}]\,. \tag{6.6}$$

<table>
<tr><td></td><td colspan="4">Molecular orbital</td><td colspan="4">Nuclear orbital</td></tr>
<tr><td></td><td>occ. (I)</td><td>occ. (II)</td><td>vir. (I)</td><td>vir. (II)</td><td>occ. (I)</td><td>vir. (I)</td><td>occ. (II)</td><td>vir. (II)</td></tr>
<tr><td>occ. (I)</td><td>ES</td><td>EX</td><td>PL(I)</td><td>CT(I→II)</td><td colspan="4" rowspan="4">0</td></tr>
<tr><td>occ. (II)</td><td>EX</td><td>ES</td><td>CT(II→I)</td><td>PL(II)</td></tr>
<tr><td>vir. (I)</td><td>PL(I)</td><td>CT(II→I)</td><td>ES</td><td>0</td></tr>
<tr><td>vir. (II)</td><td>CT(I→II)</td><td>PL(II)</td><td>0</td><td>ES</td></tr>
<tr><td>occ. (I)</td><td colspan="4" rowspan="4">0</td><td>ES</td><td>NR(I)</td><td colspan="2" rowspan="2">0</td></tr>
<tr><td>vir. (I)</td><td>NR(I)</td><td>ES</td></tr>
<tr><td>occ. (II)</td><td colspan="2" rowspan="2">0</td><td>ES</td><td>NR(II)</td></tr>
<tr><td>vir. (II)</td><td>NR(II)</td><td>ES</td></tr>
</table>

Figure 6.1. Reduced spaces of the Fock matrix for the RVS-SCF energy decomposition in the NOMO scheme. Basis of the Fock matrices are occupied and virtual orbitals of fragments I and II, as denoted by occ. (I), occ. (II), vir. (I), and vir. (II), respectively. Elements of 0 (zero) subspaces are set to zero.

In evaluating $E_{\mathrm{ES}}^{\mathrm{RVS}}$ and $E_{\mathrm{EX}}^{\mathrm{RVS}}$, the SCF procedure is not performed to preserve the .wavefunction of the isolated fragments. $E_{\mathrm{PL}}^{\mathrm{RVS}}$ is formulated as the stabilization induced by mixing the occupied and virtual MOs within each fragment. In the NOMO calculation, virtual NOs of the polarized fragment are mixed with the occupied NO for the purpose of nuclear relaxation:

$$\begin{aligned} E_{\mathrm{PL}}^{\mathrm{RVS}} &= E_{\mathrm{I+II}}[\mathrm{ES}+\mathrm{EX}+\mathrm{PL(I)}+\mathrm{NR(I)}]-E_{\mathrm{I+II}}[\mathrm{ES}+\mathrm{EX}] \\ &\quad + E_{\mathrm{I+II}}[\mathrm{ES}+\mathrm{EX}+\mathrm{PL(II)}+\mathrm{NR(II)}]-E_{\mathrm{I+II}}[\mathrm{ES}+\mathrm{EX}]. \end{aligned} \tag{6.7}$$

$E_{\mathrm{CT}}^{\mathrm{RVS}}$ is formulated as the stabilization energy obtained by delocalization from occupied MOs of one fragment to virtual MOs of the other. In the NOMO calculation, all virtual NOs are mixed to relax the nuclear wavefunctions:

$$\begin{aligned} E_{\mathrm{CT}}^{\mathrm{RVS}} &= E_{\mathrm{I+II}}[\mathrm{ES}+\mathrm{EX}+\mathrm{PL(I)}+\mathrm{CT(I}\rightarrow\mathrm{II)}+\mathrm{NR(I)}+\mathrm{NR(II)}] \\ &\quad - E_{\mathrm{I+II}}[\mathrm{ES}+\mathrm{EX}+\mathrm{PL(I)}+\mathrm{NR(I)}] \\ &\quad + E_{\mathrm{I+II}}[\mathrm{ES}+\mathrm{EX}+\mathrm{PL(II)}+\mathrm{CT(II}\rightarrow\mathrm{I)}+\mathrm{NR(I)}+\mathrm{NR(II)}] \\ &\quad - E_{\mathrm{I+II}}[\mathrm{ES}+\mathrm{EX}+\mathrm{PL(II)}+\mathrm{NR(II)}]. \end{aligned} \tag{6.8}$$

In order to correct the BSSE, the following CP correction [45] is subtracted from $E_{\mathrm{INT}}^{\mathrm{NOMO/HF}}$ and $E_{\mathrm{CT}}^{\mathrm{RVS}}$:

$$\Delta E_{\mathrm{INT(CP)}}^{\mathrm{RVS}} = E_{\mathrm{I}} - E_{\mathrm{I}}(\mathrm{occ.(II)},\mathrm{vir.(II)}) + E_{\mathrm{II}} - E_{\mathrm{II}}(\mathrm{occ.(I)},\mathrm{vir.(I)}), \tag{6.9}$$

$$\Delta E_{\mathrm{CT(CP)}}^{\mathrm{RVS}} = E_{\mathrm{I}} - E_{\mathrm{I}}(\mathrm{vir.(II)}) + E_{\mathrm{II}} - E_{\mathrm{II}}(\mathrm{vir.(I)}). \tag{6.10}$$

In Eqs. (6.9) and (6.10), the MOs treated as ghost orbitals are shown in parentheses.

In the post-HF interaction energy based on the conventional MO method, another component, which originates in the correlation energy, appears because the RVS-SCF

method can be applied only to the HF interaction energy:

$$E_{\mathrm{INT}}^{\mathrm{MO/post\text{-}HF}} = E_{\mathrm{INT}}^{\mathrm{MO/HF}} + E_{\mathrm{INT}}^{\mathrm{COR}} \ . \tag{6.11}$$

In the NOMO/MP2 method [37,38], which is the second-order Møller-Plesset perturbation theory based on the NOMO/HF wavefunction and is adopted in this chapter, the correlated wavefunction is expressed as a summation of two-electron excited configurations, one-electron and one-nucleus excited configurations, and two-nucleus excited configurations. Therefore, $E_{\mathrm{INT}}^{\mathrm{COR}}$ in Eq. (6.11) can be divided into electron-electron (ee), electron-nucleus (en), and nucleus-nucleus (nn) contributions.

$$E_{\mathrm{INT}}^{\mathrm{NOMO/MP2}} = E_{\mathrm{INT}}^{\mathrm{NOMO/HF}} + E_{\mathrm{INT}}^{\mathrm{COR(ee)}} + E_{\mathrm{INT}}^{\mathrm{COR(en)}} + E_{\mathrm{INT}}^{\mathrm{COR(nn)}} . \tag{6.12}$$

6.3. Computational details

In this chapter, $HOX\cdots OH_2$, $HOX\cdots NH_3$, $H_2CNX\cdots OH_2$, $H_2CNX\cdots NH_3$, $H_3CX\cdots OH_2$, and $H_3CX\cdots NH_3$ complexes were calculated using the NOMO/MP2 method [37,38]. Their geometries are schematically illustrated in Figure 6.2.

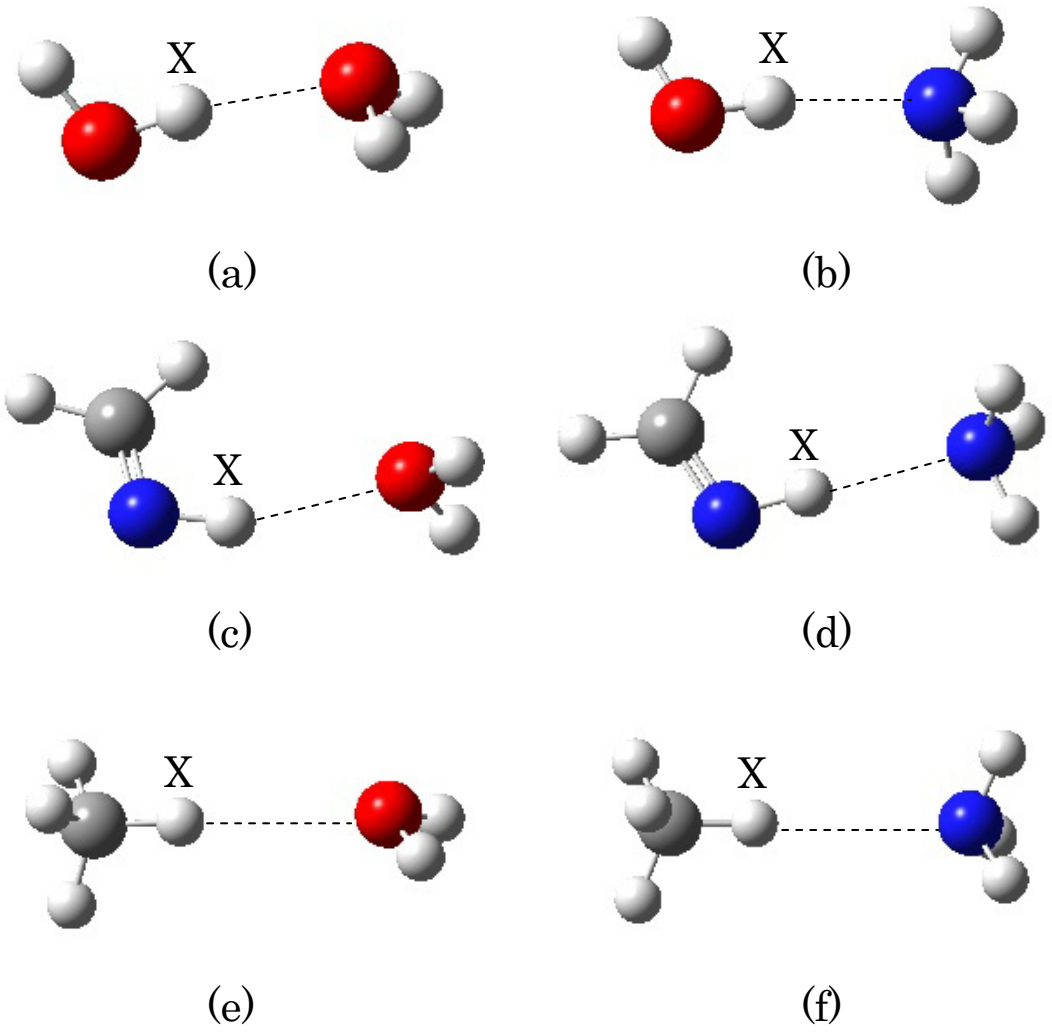

Figure 6.2. Hydrogen-bonded systems considered in this chapter: (a) $HOX\cdots OH_2$, (b) $HOX\cdots NH_3$, (c) $H_2CNX\cdots OH_2$, (d) $H_2CNX\cdots NH_3$, (e) $H_3CX\cdots OH_2$, and (f) $H_3CX\cdots NH_3$. Note that nuclei of atom X are treated as the wavefunction of proton and deuteron.

Here, the nuclei of atom X were treated as the wavefunction of proton or deuteron, and the others were treated classically, i.e., as point charges. These complexes contain typical examples of the hydrogen bond between second-row atoms and hydrogen. In the correlation energy calculation, core electrons were not frozen. The 6-311++G(3d,3p) basis set [46-48] and (5s5p5d) primitive Gaussian functions are adopted as EBFs and NBFs, respectively. Exponents of the NBFs are determined by the even-tempered scheme [49]. For geometry optimization, the gradient of the NOMO/MP2 energy with respect to each basis center was calculated numerically. It is worth noting that the orbital centers of the EBFs were set to the positions of corresponding nuclei or the orbital centers of the NBFs. Bond distances are estimated using the averaged positions of quantum nuclei $\mathbf{R}_0$, which can be evaluated as the expectation value of the nuclear position operator as follows:

$$\mathbf{R}_0 = \frac{\left\langle \Psi_{\text{NOMO/MP1}} \middle| \hat{\mathbf{R}} \middle| \Psi_{\text{NOMO/MP1}} \right\rangle}{\left\langle \Psi_{\text{NOMO/MP1}} \middle| \Psi_{\text{NOMO/MP1}} \right\rangle}. \tag{6.13}$$

All calculations are performed by modifying the GAMESS program package [50].

6.4. Results and discussion

First, the geometries of the hydrogen-bonded systems mentioned in the previous section were optimized at the NOMO/MP2 level. After the full optimization based on the numerical gradient calculation, the intermolecular distance, i.e., distance between hydrogen (deuterium) and proton- (deuteron-) acceptor atom, was reoptimized by scanning the CP-corrected interaction energy. Optimized distances of the intramolecular bond A−X and the intermolecular bond X···B in the hydrogen bond A−X···B (X = H and D) are listed in Table 6.1. Bond distance shifts induced by deuteration are shown in parentheses.

Table 6.1. Optimized bond distances of hydrogen-bonded systems obtained by the NOMO/MP2 method (in Å).

	Bond	X = H	X = D	
Intramolecular distance				
$HOX\cdots OH_2$	O−X	0.9657	0.9612	(–0.0045)
$HOX\cdots NH_3$	O−X	0.9711	0.9664	(–0.0047)
$H_2CNX\cdots OH_2$	N−X	1.0230	1.0182	(–0.0048)
$H_2CNX\cdots NH_3$	N−X	1.0258	1.0207	(–0.0051)
$H_3CX\cdots OH_2$	C−X	1.0982	1.0912	(–0.0070)
$H_3CX\cdots NH_3$	C−X	1.0984	1.0911	(–0.0074)
Intermolecular distance				
$HOX\cdots OH_2$	X···O	1.9920	2.0003	(0.0083)
$HOX\cdots NH_3$	X···N	1.9953	2.0065	(0.0112)
$H_2CNX\cdots OH_2$	X···O	2.2816	2.2842	(0.0026)
$H_2CNX\cdots NH_3$	X···N	2.2566	2.2649	(0.0083)
$H_3CX\cdots OH_2$	X···O	2.7242	2.7327	(0.0085)
$H_3CX\cdots NH_3$	X···N	2.8622	2.8760	(0.0138)

* Changes from X = H to D are shown in parentheses.

** The CP correction is applied to the optimization of the intermolecular distance.

The GIEs in the hydrogen bond, namely, the intramolecular bond shrinkage and the intermolecular bond elongation, are reproduced qualitatively. The bond length shifts except for A−X and X···B are significantly small, i.e., less than 3×10^{-4} Å.

Interaction energies and their components at the optimized geometries are summarized in Table 6.2. Here, negative (positive) values correspond to attractive (repulsive) interactions. The CP correction is applied to the calculation of $E_{\mathrm{CT}}^{\mathrm{RVS}}$, $E_{\mathrm{INT}}^{\mathrm{NOMO/HF}}$, $E_{\mathrm{INT}}^{\mathrm{COR(ee)}}$, $E_{\mathrm{INT}}^{\mathrm{COR(en)}}$, and $E_{\mathrm{INT}}^{\mathrm{NOMO/MP2}}$.

Table 6.2. Decomposition of the NOMO/MP2 interaction energy at optimized geometries (in kcal/mol).

		NOMO/HF interaction energy component						Correlation effect		$E_{INT}^{NOMO/MP2}$
		E_{ES}^{RVS}	E_{EX}^{RVS}	E_{PL}^{RVS}	E_{CT}^{RVS}	E_{RES}^{RVS}	$E_{INT}^{NOMO/HF}$	$E_{INT}^{COR(ee)}$	$E_{INT}^{COR(en)}$	
$HOX\cdots OH_2$	X = H	–8.194	5.769	–1.019	–0.773	0.092	–4.125	–0.899	0.162	–4.862
	X = D	–8.013	5.656	–0.969	–0.753	0.080	–3.998	–0.879	0.100	–4.778
	Δ	0.180	–0.113	0.050	0.020	–0.012	0.126	0.020	–0.062	0.084
$HOX\cdots NH_3$	X = H	–11.503	9.683	–1.734	–1.610	0.063	–5.102	–1.545	0.215	–6.432
	X = D	–11.214	9.451	–1.644	–1.566	0.052	–4.920	–1.502	0.130	–6.292
	Δ	0.290	–0.232	0.090	0.045	–0.010	0.182	0.043	–0.085	0.140
$H_2CNX\cdots OH_2$	X = H	–4.432	2.937	–0.507	–0.314	0.040	–2.276	–0.824	0.090	–3.010
	X = D	–4.362	2.894	–0.493	–0.305	0.036	–2.230	–0.824	0.069	–2.985
	Δ	0.070	–0.043	0.014	0.009	–0.004	0.046	–0.001	–0.020	0.025
$H_2CNX\cdots NH_3$	X = H	–6.424	5.539	–0.953	–0.802	0.027	–2.613	–1.324	0.170	–3.767
	X = D	–6.242	5.396	–0.913	–0.774	0.023	–2.510	–1.312	0.112	–3.710
	Δ	0.182	–0.143	0.040	0.028	–0.004	0.103	0.012	–0.057	0.057
$H_3CX\cdots OH_2$	X = H	–0.745	0.777	–0.163	–0.076	0.023	–0.185	–0.454	0.061	–0.578
	X = D	–0.688	0.741	–0.157	–0.071	0.022	–0.154	–0.447	0.042	–0.559
	Δ	0.057	–0.036	0.006	0.005	–0.001	0.030	0.007	–0.019	0.018
$H_3CX\cdots NH_3$	X = H	–1.003	1.135	–0.219	–0.154	0.031	–0.210	–0.561	0.075	–0.695
	X = D	–0.925	1.076	–0.210	–0.144	0.029	–0.174	–0.546	0.051	–0.669
	Δ	0.078	–0.059	0.009	0.010	–0.002	0.036	0.015	–0.025	0.026

* Changes from X = H to D are denoted as Δ.

Note that $E_{\mathrm{INT}}^{\mathrm{COR(nn)}}$ does not appear because only one nucleus is treated quantum-mechanically at the same time. According to $E_{\mathrm{INT}}^{\mathrm{NOMO/MP2}}$, the calculated systems are classified into strongly interacting systems ($HOX\cdots OH_2$, $HOX\cdots NH_3$, $H_2CNX\cdots OH_2$, and $H_2CNX\cdots NH_3$) and weakly interacting systems ($H_3CX\cdots OH_2$ and $H_3CX\cdots NH_3$). In all systems, the total interaction energy $E_{\mathrm{INT}}^{\mathrm{NOMO/MP2}}$ is less negative in X = D than in X = H, which is in agreement with the results of previously reported quantum-chemical calculations [18,22]. $E_{\mathrm{INT}}^{\mathrm{COR(ee)}}$ is usually less negative than $E_{\mathrm{ES}}^{\mathrm{RVS}}$. However, it plays an important role in $H_3CX\cdots OH_2$ and $H_3CX\cdots NH_3$ because of its comparability to $E_{\mathrm{INT}}^{\mathrm{NOMO/MP2}}$. The small positive values of $E_{\mathrm{INT}}^{\mathrm{COR(en)}}$ can be attributed to the electronic delocalization around a proton or deuteron because of the formation of a hydrogen bond. In terms of the isotope effect, the negative components shift toward the positive direction, and vice versa. In other words, the absolute values of all components become small owing to deuteration. It is worth mentioning that the absolute values of all components and their isotopic shifts in the NH_3 complexes are larger than those in the H_2O complexes.

Now, the RVS-SCF energy components are focused on. $E_{\mathrm{ES}}^{\mathrm{RVS}}$ and $E_{\mathrm{EX}}^{\mathrm{RVS}}$ are dominant attractive and repulsive components in all systems, respectively. For $H_3CX\cdots OH_2$ and $H_3CX\cdots NH_3$, the absolute value of $E_{\mathrm{ES}}^{\mathrm{RVS}}$ is smaller than that of $E_{\mathrm{EX}}^{\mathrm{RVS}}$, which indicates the weakness of the electrostatic interaction in $\in X\cdots O$ and $C-X\cdots N$ hydrogen bonds. $E_{\mathrm{PL}}^{\mathrm{RVS}}$ and $E_{\mathrm{CT}}^{\mathrm{RVS}}$ are considerably less negative than $E_{\mathrm{ES}}^{\mathrm{RVS}}$, and $E_{\mathrm{RES}}^{\mathrm{RVS}}$ is less than 0.1 kcal/mol in all systems. The above analysis reveals that the interaction energies $E_{\mathrm{INT}}^{\mathrm{NOMO/HF}}$ are approximately determined by $E_{\mathrm{ES}}^{\mathrm{RVS}}$ and $E_{\mathrm{EX}}^{\mathrm{RVS}}$. Because these results are consistent with the results of intermolecular perturbation theory [51], it is inferred that the RVS-SCF method in the NOMO scheme appropriately describes the property of the hydrogen bond.

The isotopic shifts of energy components can be analyzed by introducing an intermediate model to describe intermolecular and intramolecular scenarios. In the intermediate model, atom X is deuterium, and the intermolecular distance is fixed at the optimized value for X = H. The other geometric parameters agree with the optimized values for X = D. The intermediate model denoted by geometry (b) in the case of $HOX\cdots OH_2$ is illustrated in Figure 6.3 (b). As shown in Figure 6.3, geometries (a) and

(c) correspond to the optimized geometries with X = H and X = D, respectively. The process of geometry (a) to (b) corresponds to the isotope substitution with fixed intermolecular distance. Because the wavefunction of a proton-acceptor molecule is supposed to be almost invariant by deuteration, the difference in energy components between geometries (a) and (b) is regarded as the isotope effect in the proton-donor molecule. In contrast, the process of geometry (b) to (c) corresponds to the structural relaxation. The effect of the intermolecular bond elongation can be analyzed by comparing energy components in geometry (b) with those in (c).

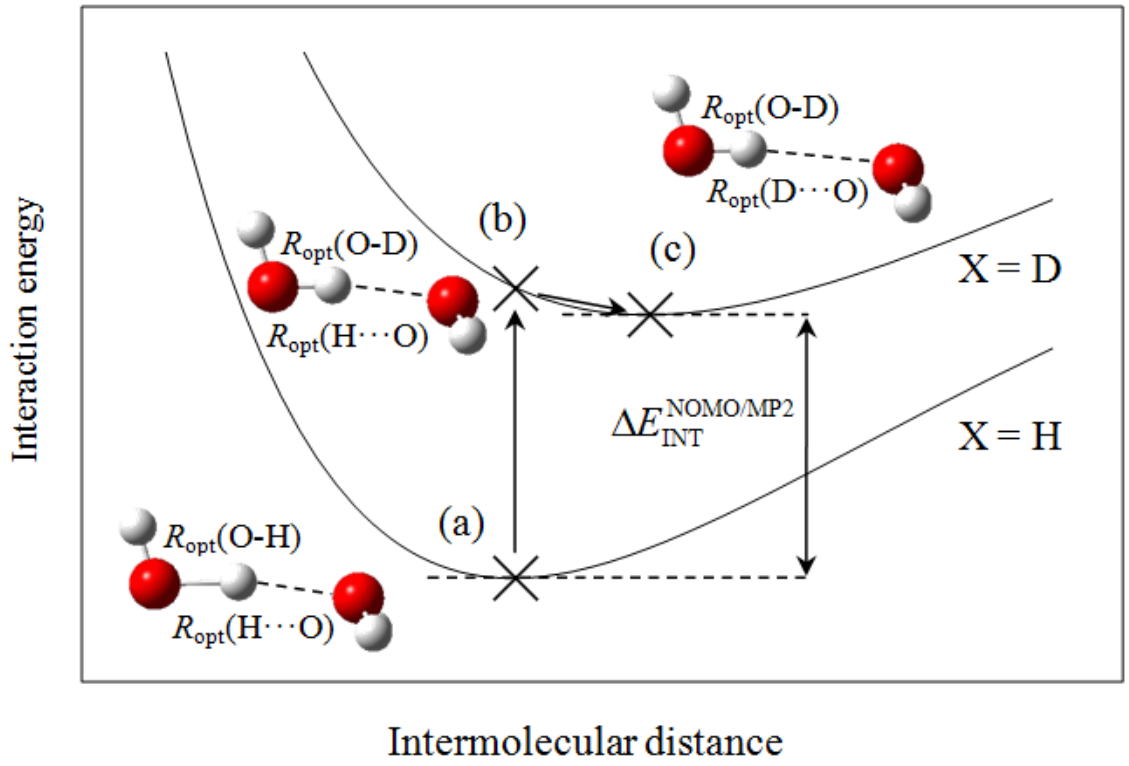

Figure 6.3. Geometric and energetic relations of three conditions: (a) optimized geometry with X = H, (b) intermediate model, and (c) optimized geometry with X = D. The illustration of bond distance shifts is exaggerated.

Energy component shifts from geometry (a) to (b) are listed in Table 6.3. Note that the data are given in cal/mol. $\Delta E_{\mathrm{ES}}^{\mathrm{RVS}}$ is constantly positive, which is consistent with the decrease in atomic charge in proton- (deuteron-) donor molecules [15,20,22,23]. Although $E_{\mathrm{ES}}^{\mathrm{RVS}}$ is small in $H_3CX\cdots OH_2$ and $H_3CX\cdots NH_3$, it is interesting that $\Delta E_{\mathrm{ES}}^{\mathrm{RVS}}$ in those systems is comparable to that in more strongly interacting systems. $\Delta E_{\mathrm{EX}}^{\mathrm{RVS}}$ has large positive values in $HOX\cdots OH_2$ and $HOX\cdots NH_3$, while it is negative in $H_2CNX\cdots OH_2$, $H_3CX\cdots OH_2$, and $H_3CX\cdots NH_3$. $\Delta E_{\mathrm{PL}}^{\mathrm{RVS}}$ is positive and correlates with $\Delta E_{\mathrm{INT}}^{\mathrm{NOMO/MP2}}$. Although $\Delta E_{\mathrm{PL}}^{\mathrm{RVS}}$ is always smaller than $\Delta E_{\mathrm{ES}}^{\mathrm{RVS}}$, the contribution of $\Delta E_{\mathrm{PL}}^{\mathrm{RVS}}$ to the destabilization of total interaction is not negligible in strongly interacting systems. $\Delta E_{\mathrm{CT}}^{\mathrm{RVS}}$ and $\Delta E_{\mathrm{INT}}^{\mathrm{COR(ee)}}$ are considerably small, though their sign is dependent on the element of proton- (deuteron-) donor atom. $\Delta E_{\mathrm{INT}}^{\mathrm{COR(en)}}$ is negative because $E_{\mathrm{INT}}^{\mathrm{COR(en)}}$ must converge to zero along with the increase in nuclear mass. From the results obtained, various trends of energy component shift caused by the intramolecular isotope effect can be observed. In addition, it can be seen that the electrostatic interaction plays an important role in the destabilization of total intermolecular interaction in any systems.

Energy component shifts from geometry (b) to (c) are listed in Table 6.4. $\Delta E_{\mathrm{EX}}^{\mathrm{RVS}}$ has a large negative value, reflecting the short-range nature of the exchange-repulsion, whereas $\Delta E_{\mathrm{ES}}^{\mathrm{RVS}}$, $\Delta E_{\mathrm{PL}}^{\mathrm{RVS}}$, $\Delta E_{\mathrm{CT}}^{\mathrm{RVS}}$, and $\Delta E_{\mathrm{INT}}^{\mathrm{COR(ee)}}$ are positive. These trends correctly reflect the intermolecular bond elongation. In all systems, $\Delta E_{\mathrm{ES}}^{\mathrm{RVS}}$ is larger than $\Delta E_{\mathrm{PL}}^{\mathrm{RVS}}$, $\Delta E_{\mathrm{CT}}^{\mathrm{RVS}}$, and $\Delta E_{\mathrm{INT}}^{\mathrm{COR(ee)}}$. $\Delta E_{\mathrm{INT}}^{\mathrm{COR(en)}}$ is negligibly small. Owing to the cancellation of $\Delta E_{\mathrm{EX}}^{\mathrm{RVS}}$ and other components, $\Delta E_{\mathrm{INT}}^{\mathrm{NOMO/MP2}}$ is considerably small. The negativity of $\Delta E_{\mathrm{INT}}^{\mathrm{NOMO/MP2}}$ indicates that the stabilization energy due to the decrease in exchange-repulsion interaction exceeds the loss of attractive interactions. From a quantitative point of view, the isotopic shifts of interaction energy components are rather different for each system. The absolute values of them are affected by the strength of intermolecular interaction and the width of intermolecular bond elongation. From the results mentioned above, the bond elongation was found to be determined by the sensitive balance between the exchange-repulsion interaction and other components.

Table 6.3. Energy component shifts from geometry (a) to (b) (in cal/mol), which are regarded as the effect of the intramolecular bond shrinkage in proton-donor molecule.

	NOMO/HF interaction energy component						Correlation effect		$\Delta E_{INT}^{NOMO/MP2}$
	ΔE_{ES}^{RVS}	ΔE_{EX}^{RVS}	ΔE_{PL}^{RVS}	ΔE_{CT}^{RVS}	ΔE_{RES}^{RVS}	$\Delta E_{INT}^{NOMO/HF}$	$\Delta E_{INT}^{COR(ee)}$	$\Delta E_{INT}^{COR(en)}$	
$HOX\cdots OH_2$	62.3	61.7	25.4	0.1	–11.0	138.5	7.4	-61.4	84.5
$HOX\cdots NH_3$	70.3	120.8	36.6	-6.2	–9.8	211.6	13.5	–83.7	141.4
$H_2CNX\cdots OH_2$	52.4	–16.1	10.5	6.3	–3.8	49.5	–4.3	–20.0	25.2
$H_2CNX\cdots NH_3$	91.2	1.1	20.3	10.5	–4.2	118.8	–4.9	–56.4	57.5
$H_3CX\cdots OH_2$	44.6	-14.0	2.9	3.4	–0.8	36.1	1.1	–18.7	18.4
$H_3CX\cdots NH_3$	52.1	–10.9	3.4	4.5	–1.4	47.7	2.9	–24.0	26.7

Table 6.4. Energy component shifts from geometry (b) to (c) (in cal/mol), which are regarded as the effect of the intermolecular bond elongation.

	NOMO/HF interaction energy component						Correlation effect		$\Delta E_{INT}^{NOMO/MP2}$
	ΔE_{ES}^{RVS}	ΔE_{EX}^{RVS}	ΔE_{PL}^{RVS}	ΔE_{CT}^{RVS}	ΔE_{RES}^{RVS}	$\Delta E_{INT}^{NOMO/HF}$	$\Delta E_{INT}^{COR(ee)}$	$\Delta E_{INT}^{COR(en)}$	
$HOX\cdots OH_2$	117.9	–174.8	24.9	20.3	–0.6	–12.2	12.5	–1.0	–0.7
$HOX\cdots NH_3$	219.5	–353.0	53.4	50.7	–0.4	–29.7	29.7	–1.4	–1.3
$H_2CNX\cdots OH_2$	17.9	–26.8	3.1	2.5	–0.1	–3.4	3.6	–0.2	0.0
$H_2CNX\cdots NH_3$	90.8	–144.2	19.8	17.5	–0.2	–16.2	16.8	–1.1	–0.5
$H_3CX\cdots OH_2$	12.1	–22.3	2.7	1.8	–0.3	-6.0	6.2	–0.4	–0.1
$H_3CX\cdots NH_3$	25.9	–47.6	5.6	5.5	–0.7	–11.3	11.7	–0.7	–0.3

Now, let us summarize the intramolecular and intermolecular effects. In weakly interacting systems such as $H_3CX\cdots OH_2$ and $H_3CX\cdots NH_3$, the decrease of electrostatic interaction by deuterization causes the intermolecular GIE to reduce the exchange-repulsion interaction. In more strongly interacting systems, the destabilization obtained by the intramolecular effect originates in the exchange-repulsion and polarization interactions as well as the electrostatic interaction.

6.5. Conclusion

In this chapter, the isotopic shift of interaction energy components in hydrogen-bonded systems was investigated in order to interpret the intermolecular GIE by the RVS-SCF method extended to the NOMO scheme. The total GIE was divided into two processes: namely, the intramolecular bond shrinkage and the intermolecular bond elongation. The RVS-SCF analysis on the GIEs clarified that the isotope effect in proton-donor molecule led to the decrease in the electrostatic interaction in all systems and the exchange-repulsion interaction for two strongly interacting systems. In contrast, the intermolecular bond elongation stabilizes the hydrogen-bonded systems because the stabilization obtained by the exchange-repulsion interaction always exceeded the destabilization by the other energy components. As shown in the appendix, the results obtained with the KM + NOMO approach are close to the RVS-SCF + NOMO ones. Consequently, the intermolecular GIE is approximately interpreted as a process reducing the exchange-repulsion interaction after the decrease of electrostatic interaction.

Appendix

The KM analysis [25-27] is also extended to the NOMO scheme in addition to the RVS-SCF method. In the original KM analysis [25,26], the HF interaction energy is decomposed as

$$E_{\mathrm{INT}}^{\mathrm{MO/HF}} = E_{\mathrm{ES}}^{\mathrm{KM}} + E_{\mathrm{EX}}^{\mathrm{KM}} + E_{\mathrm{PL}}^{\mathrm{KM}} + E_{\mathrm{CT}}^{\mathrm{KM}} + E_{\mathrm{MIX}}^{\mathrm{KM}}. \tag{6.A1}$$

$E_{\mathrm{PL}}^{\mathrm{KM}}$ and $E_{\mathrm{CT}}^{\mathrm{KM}}$ do not converge at the basis set limit because the exchange interaction is neglected in their calculation. The refined KM energy decomposition can be written as follows [27]:

$$E_{\mathrm{INT}}^{\mathrm{MO/HF}} = E_{\mathrm{ES}}^{\mathrm{KM}} + E_{\mathrm{EX}}^{\mathrm{KM}} + E_{\mathrm{CTPLX}}^{\mathrm{KM}} + E_{\mathrm{RES}}^{\mathrm{KM}}. \tag{6.A2}$$

Here, Eq. (6.A2) is extended to the NOMO/HF method:

$$E_{\mathrm{INT}}^{\mathrm{NOMO/HF}} = E_{\mathrm{ES}}^{\mathrm{KM}} + E_{\mathrm{EX}}^{\mathrm{KM}} + E_{\mathrm{CTPLX}}^{\mathrm{KM}} + E_{\mathrm{RES}}^{\mathrm{KM}}. \tag{6.A3}$$

$E_{\mathrm{ES}}^{\mathrm{KM}}$ and $E_{\mathrm{EX}}^{\mathrm{KM}}$ are calculated in the same manner as the corresponding components in the RVS-SCF scheme:

$$E_{\mathrm{ES}}^{\mathrm{KM}} = E_{\mathrm{I+II}}[\mathrm{ES}] - \{E_{\mathrm{I}} + E_{\mathrm{II}}\}, \tag{6.A4}$$

$$E_{\mathrm{EX}}^{\mathrm{KM}} = E_{\mathrm{I+II}}[\mathrm{ES+EX}] - E_{\mathrm{I+II}}[\mathrm{ES}]. \tag{6.A5}$$

The polarization and charge transfer interactions are integrated into $E_{\mathrm{CTPLX}}^{\mathrm{KM}}$. In the NOMO calculation, all NOs are optimized by including NR blocks.

$$E_{\mathrm{CTPLX}}^{\mathrm{KM}} = E_{\mathrm{I+II}}[\mathrm{ES+EX+CTPLX(I)+NR}] - E_{\mathrm{I+II}}[\mathrm{ES+EX}]$$

$$+ E_{\mathrm{I+II}}[\mathrm{ES} + \mathrm{EX} + \mathrm{CTPLX(II)} + \mathrm{NR}] - E_{\mathrm{I+II}}[\mathrm{ES} + \mathrm{EX}]\,. \tag{6.A6}$$

The following CP correction is subtracted from $E_{\mathrm{EX}}^{\mathrm{KM}}$ and $E_{\mathrm{EX}}^{\mathrm{KM}}$ to remove the BSSE:

$$\Delta E_{\mathrm{EX(CP)}}^{\mathrm{KM}} = E_{\mathrm{I}} - E_{\mathrm{I}}(\mathrm{occ.(II)}) + E_{\mathrm{II}} - E_{\mathrm{II}}(\mathrm{occ.(I)})\,, \tag{6.A7}$$

$$\Delta E_{\mathrm{CTPLX(CP)}}^{\mathrm{KM}} = E_{\mathrm{I}} - E_{\mathrm{I}}(\mathrm{vir.(II)}) + E_{\mathrm{II}} - E_{\mathrm{II}}(\mathrm{vir.(I)})\,. \tag{6.A8}$$

<table>
<tr><td></td><td colspan="4">Molecular orbital</td><td colspan="4">Nuclear orbital</td></tr>
<tr><td></td><td>occ. (I)</td><td>occ. (II)</td><td>vir. (I)</td><td>vir. (II)</td><td>occ. (I)</td><td>vir. (I)</td><td>occ. (II)</td><td>vir. (II)</td></tr>
<tr><td>occ. (I)</td><td>ES</td><td>EX</td><td>CTPLX(I)</td><td>CTPLX(I)</td><td colspan="4" rowspan="4">0</td></tr>
<tr><td>occ. (II)</td><td>EX</td><td>ES</td><td>CTPLX(II)</td><td>CTPLX(II)</td></tr>
<tr><td>vir. (I)</td><td>CTPLX(I)</td><td>CTPLX(II)</td><td>ES</td><td>0</td></tr>
<tr><td>vir. (II)</td><td>CTPLX(I)</td><td>CTPLX(II)</td><td>0</td><td>ES</td></tr>
<tr><td>occ. (I)</td><td colspan="4" rowspan="4">0</td><td>ES</td><td>NR</td><td colspan="2" rowspan="2">0</td></tr>
<tr><td>vir. (I)</td><td>NR</td><td>ES</td></tr>
<tr><td>occ. (II)</td><td colspan="2" rowspan="2">0</td><td>ES</td><td>NR</td></tr>
<tr><td>vir. (II)</td><td>NR</td><td>ES</td></tr>
</table>

Figure 6.A1. Reduced spaces of the Fock matrix for the KM energy decomposition in the NOMO scheme. Basis of the Fock matrices are occupied and virtual orbitals of fragments I and II, similar to the RVS-SCF method shown in Figure 6.1.

Table 6.A1. Interaction energy components of the KM analysis at NOMO/MP2 optimized geometries (in kcal/mol).

	E_{ES}^{KM}	E_{EX}^{KM}	E_{CTPLX}^{KM}	E_{RES}^{KM}
$HOX\cdots OH_2$				
X = H	–8.194	5.781	–2.119	0.407
X = D	–8.013	5.665	–2.030	0.380
Δ	0.180	–0.116	0.089	–0.027
$HOX\cdots NH_3$				
X = H	–11.503	9.697	–4.145	0.849
X = D	–11.214	9.462	–3.957	0.789
Δ	0.290	–0.236	0.136	–0.032
$H_2CNX\cdots OH_2$				
X = H	–4.432	2.942	–0.951	0.165
X = D	–4.362	2.899	–0.925	0.158
Δ	0.070	–0.043	0.026	–0.007
$H_2CNX\cdots NH_3$				
X = H	-6.424	5.550	–2.066	0.328
X = D	-6.242	5.406	–1.992	0.319
Δ	0.182	–0.144	0.074	–0.009
$H_3CX\cdots OH_2$				
X = H	–0.745	0.778	–0.265	0.047
X = D	–0.688	0.741	–0.252	0.045
Δ	0.057	–0.036	0.012	–0.002
$H_3CX\cdots NH_3$				
X = H	–1.003	1.137	–0.398	0.054
X = D	–0.925	1.078	–0.378	0.051
Δ	0.078	–0.059	0.020	–0.003

* Changes from X = H to D are denoted as Δ.

Energy components of the KM analysis are shown in Table 6.A1. Here, the CP correction is applied to the calculation of E_{EX}^{KM} and E_{EX}^{KM}. E_{ES}^{KM} is equivalent to E_{ES}^{RVS} by definition, and E_{EX}^{KM} is close in value to E_{EX}^{KM}. E_{CTPLX}^{KM} is slightly more negative than the sum of E_{PL}^{RVS} and E_{CT}^{RVS}. Energy component shifts are summarized in Table 6.A2. In the process of geometry (a) to (b), ΔE_{ES}^{KM} is the dominant component that approximately contributes to the destabilization of intermolecular interaction although ΔE_{CTPLX}^{KM} exceeds the sum of ΔE_{PL}^{RVS} and ΔE_{CT}^{RVS} in Table 6.3. In the process of geometry (b) to (c), ΔE_{CTPLX}^{KM} is less negative than ΔE_{ES}^{KM} though ΔE_{CTPLX}^{KM} exceeds the sum of ΔE_{PL}^{RVS} and ΔE_{CT}^{RVS} in Table 6.4. Thus, the KM analysis was found to give the same conclusion as the RVS-SCF method with respect to the interpretation of the GIE in the hydrogen bond.

Table 6.A2. Energy component shifts of the KM analysis (in cal/mol).

	ΔE_{ES}^{KM}	ΔE_{EX}^{KM}	ΔE_{CTPLX}^{KM}	ΔE_{RES}^{KM}
Geometry (a) to (b)				
$HOX\cdots OH_2$	62.3	58.8	31.8	–14.5
$HOX\cdots NH_3$	70.3	117.3	51.7	–27.8
$H_2CNX\cdots OH_2$	52.4	–16.4	19.1	–5.6
$H_2CNX\cdots NH_3$	91.2	0.4	26.1	1.2
$H_3CX\cdots OH_2$	44.6	–14.1	7.1	–1.6
$H_3CX\cdots NH_3$	52.1	–11.0	8.4	–1.8
Geometry (b) to (c)				
$HOX\cdots OH_2$	117.9	–174.9	56.9	–12.2
$HOX\cdots NH_3$	219.5	–353.0	136.4	–31.9
$H_2CNX\cdots OH_2$	17.9	–26.9	6.9	–1.4
$H_2CNX\cdots NH_3$	90.8	–144.4	48.0	–10.6
$H_3CX\cdots OH_2$	12.1	–22.3	5.1	–0.9
$H_3CX\cdots NH_3$	25.9	–47.6	12.0	–1.5

References

[1] A. R. Ubbelohde, *Proc. R. Soc. A* **170**, 417 (1939).

[2] M. Ichikawa, *Acta Cryst. B* **34**, 2074 (1978).

[3] M. Ichikawa, *Chem. Phys. Lett.* **79**, 583 (1981).

[4] M. Ichikawa, K. Motida, N. Yamada, *Phys. Rev. B* **36**, 874 (1987).

[5] M. Ichikawa, *J. Mol. Struct.* **552**, 63 (2000).

[6] N. D. Sokolov, M. V. Vener, V. A. Savel'ev, *J. Mol. Struct.* **177**, 93 (1988).

[7] I. G. Shenderovich, H. H. Limbach, S. N. Smirnov, P. M. Tolstoy, G. S. Denisov, N. S. Golubev, *Phys. Chem. Chem. Phys.* **4**, 5488 (2002).

[8] P. M. Tolstoy, P. Schah-Mohammedi, S. N. Smirnov, N. S. Golubev, G. S. Denisov, H. H. Limbach, *J. Am. Chem. Soc.* **126**, 5621 (2004).

[9] M. Pietrzak, M. F. Shibl, M. Bröring, O. Kühn, H. H. Limbach, *J. Am. Chem. Soc.* **129**, 296 (2007).

[10] A. K. Soper, C. J. Benmore, *Phys. Rev. Lett.* **101**, 066502 (2008).

[11] A. C. Legon, C. A. Rego, A. L. Wallwork, *J. Chem. Phys.* **97**, 3050 (1992).

[12] P. W. Fowler, A. C. Legon, S. A. Peebles, *Chem. Phys. Lett.* **226**, 501 (1994).

[13] A.C. Legon, P. Ottavian, *Phys. Chem. Chem. Phys.* **4**, 4103 (2002).

[14] M. F. Shibl, M. Tachikawa, O. Kühn, *Phys. Chem. Chem. Phys.* **7**, 1368 (2005).

[15] A. Reyes, M. V. Pak, S. Hammes-Schiffer, *J. Chem. Phys.* **123**, 064104 (2005).

[16] T. Ishimoto, M. Tachikawa, U. Nagashima, *J. Chem. Phys.* **124**, 014112 (2006).

[17] T. Udagawa, T. Ishimoto, H. Tokiwa, M. Tachikawa, U. Nagashima, *J. Phys. Chem. A* **110**, 7279 (2006).

[18] T. Ishimoto, M. Tachikawa, U. Nagashima, *J. Chem. Phys.* **125**, 144103 (2006).

[19] M. F. Shibl, M. Pietrzak, H. H. Limbach, O. Kühn, *Chem. Phys. Chem.* **8**, 315 (2007).

[20] S. A. González, N. F. Aguirre, A. Reyes, *Int. J. Quant. Chem.* **108**, 1742 (2008).

[21] Y. Kikuta, T. Ishimoto, U. Nagashima, *Bull. Chem. Soc. Jpn.* **81**, 820 (2008).

[22] Y. Kikuta, T. Ishimoto, U. Nagashima, *Chem. Phys.* **354**, 218 (2008).

[23] T. Udagawa, M. Tachikawa, *J. Mol. Struct.(THEOCHEM)* **912**, 63 (2009).

[24] T. Takayanagi, T. Yoshikawa, H. Motegi, M. Shiga, *Chem. Phys. Lett.* **482**, 195

(2009).

[25] K. Morokuma, *J. Chem. Phys.* **55**, 1236 (1971).

[26] K. Kitaura, K. Morokuma, *Int. J. Quant. Chem.* **10**, 325 (1976).

[27] K. Morokuma, K. Kitaura, *Chemical Applications of Atomic and Molecular Electrostatic Potentials*, edited by P. Politzer, D. G. Truhlar (Plenum Press, New York, 1981).

[28] P. S. Bagus, K. Hermann, J. C. W. Bauschlicher, *J. Chem. Phys.* **80**, 4378 (1984).

[29] W. J. Stevens, W. H. Fink, *Chem. Phys. Lett.* **139**, 15 (1987).

[30] E. D. Glendening, A. J. Streitwieser, *Chem. Phys.* **100**, 2900 (1994).

[31] Y. R. Mo, J. L. Gao, S. D. Peyerimhoff, *J. Chem. Phys.* **112**, 5530 (2000).

[32] Y. Kawamura, H. Nakai, *J. Comput. Chem.* **25**, 1882 (2004).

[33] R. Z. Khaliullin, E. A. Cobar, R. C. Lochan, A. T. Bell, M. Head-Gordon, *J. Phys. Chem. A* **111**, 8753 (2007).

[34] P. Su, H. Li, *J. Chem. Phys.* **131**, 014102 (2009).

[35] M. Tachikawa, K. Mori, H. Nakai, K. Iguchi, *Chem. Phys. Lett.* **290**, 437 (1998).

[36] H. Nakai, *Int. J. Quant. Chem.* **86**, 511 (2002).

[37] H. Nakai, K. Sodeyama, *J. Chem. Phys.* **118**, 1119 (2003).

[38] M. Hoshino, H. Nakai, *J. Chem. Phys.* **124**, 194110 (2006).

[39] M. Hoshino, Y. Tsukamoto, H. Nakai, *Int. J. Quant. Chem.* **107**, 2575 (2007).

[40] H. Nakai, *Int. J. Quant. Chem.* **107**, 2849 (2007).

[41] Y. Shigeta, Y. Ozaki, K. Kodama, H. Nagao, H. Kawabe, K. Nishikawa, *Int. J. Quant. Chem.* **69**, 629 (1998).

[42] M. Tachikawa, *Chem. Phys. Lett.* **360**, 494 (2002).

[43] S. P. Webb, T. Iordanov, S. Hammes-Schiffer, *J. Chem. Phys.* **117**, 4106 (2002).

[44] D. V. Moreno, S. A. González, A. Reyes, *J. Phys. Chem. A*, **114**, 9231 (2010).

[45] S. F. Boys, F. Bernardi, *Mol. Phys.* **19**, 553 (1970).

[46] R. Krishnan, J. S. Binkley, R. Seeger, J. A. Pople, *J. Chem. Phys.* **72**, 650 (1980).

[47] M. J. Frisch, J. A. Pople, J. S. Binkley, *J. Chem. Phys.* **80**, 3265 (1984).

[48] T. Clark, J. Chandrasekhar, G. W. Spitznagel, P. V. R. Schleyer, *J. Comput. Chem.* **4**, 294 (1983).

[49] R. D. Bardo, K. Ruedenberg, *J. Chem. Phys.* **60**, 918 (1974).

[50] M. W. Schmidt *et al.*, *J. Comput. Chem.* **14**, 1347 (1993).

[51] A. J. Stone, *Chem. Phys. Lett.* **211**, 101 (1993).

Chapter 7
Investigation of Geometric Isotope Effect in Dihydrogen Bond

7.1. Introduction

A new type of hydrogen bond named dihydrogen bond has been actively studied from experimental point of view since 2000s [1,2]. Dihydrogen-bonded systems possess $A-H^{+\delta}\cdots{}^{-\delta}H-B$, where A designates more electronegative atoms than hydrogen and B designates less electronegative ones. Typically, nitrogen and oxygen are selected as A and boron, transition metals, and alkali metals are as B. As shown by the polarization δ, H−B acts as a proton acceptor and A as a proton donor. This completely differs from a typical behavior of conventional hydrogen-bonded systems in terms of the fact that the negatively charged H accepts a proton.

Although a number of *ab initio* quantum chemical calculations [3-5] on the dihydrogen bond have been carried out, they do not consider nuclear quantum effects. In addition to the approach based on the path-integral molecular dynamic simulation [6], it is fruitful to adopt the NOMO method [7-20], which simultaneously determines nuclear and electronic .wavefunctions quantum-mechanically. Using analytic energy gradients in the HF calculation of the NOMO theory [16], geometric isotope effects by substituting H···H with D···D or T···T are examined to elucidate how quantum effect affects bond distances.

7.2. Theoretical aspects

In this section, the analytic energy gradients of the NOMO/HF energy are formulated. The total Hamiltonian for nuclei and electrons is given by

$$\hat{H}_{\mathrm{NOMO/HF}} = -\sum_{p}\frac{1}{2}\nabla(\mathbf{x}_p)^2 - \sum_{P}\frac{1}{2m_P}\nabla(\mathbf{x}_P)^2 + \sum_{p<q}\frac{1}{r_{pq}} - \sum_{p,P}\frac{Z_P}{r_{pP}} + \sum_{P<Q}\frac{Z_P Z_Q}{r_{PQ}}. \qquad (7.1)$$

Here, the first and the second terms are electronic and nuclear kinetic operators, respectively. The other terms represent two-particle interactions. Note that the summation of p and q runs over electrons, and P and Q runs over nuclei. The NOMO/HF equations can be derived when the total HF .wavefunction Φ_0 is constructed by antisymmetric (or symmetric) products of the NOs and MOs. The NOMO/HF equation is derived by the usual variational technique. As a result, the NOMO/HF energy is described by,

$$E_{\mathrm{NOMO/HF}} = \sum_{\mu\nu}^{\mathrm{elec}} P^{\mathrm{e}}_{\mu\nu} T^{\mathrm{e}}_{\mu\nu} + \sum_{\mu\nu}^{\mathrm{nuc}} P^{\mathrm{n}}_{\mu\nu} T^{\mathrm{n}}_{\mu\nu} + \frac{1}{2}\sum_{\mu\nu\lambda\sigma}^{\mathrm{elec}} P^{\mathrm{e}}_{\mu\nu} P^{\mathrm{e}}_{\lambda\sigma} \langle \mu\lambda \| \nu\sigma \rangle$$

$$+ \sum_{\mu\nu}^{\mathrm{elec}}\sum_{\lambda\sigma}^{\mathrm{nuc}} P^{\mathrm{e}}_{\mu\nu} P^{\mathrm{n}}_{\lambda\sigma} \langle \mu\lambda | \nu\sigma \rangle + \frac{1}{2}\sum_{\mu\nu\lambda\sigma}^{\mathrm{nuc}} P^{\mathrm{n}}_{\mu\nu} P^{\mathrm{n}}_{\lambda\sigma} \langle \mu\lambda \| \nu\sigma \rangle, \qquad (7.2)$$

where

$$P^{\mathrm{e}}_{\mu\nu} = \sum_{i}^{occ} C^{*}_{\mu i} C_{\nu i}, \qquad (7.3)$$

$$P^{\mathrm{n}}_{\mu\nu} = \sum_{I}^{occ} C^{*}_{\mu I} C_{\nu I}, \qquad (7.4)$$

$$\mathbf{P} = \begin{bmatrix} \mathbf{P}^{\mathrm{e}} & \mathbf{0} \\ \mathbf{0} & \mathbf{P}^{\mathrm{n}} \end{bmatrix}. \qquad (7.5)$$

μ, ν, λ, and σ represent nuclear or electronic basis functions. Eq. (7.5) consists of the elements of electronic and nuclear density matrices given by Eqs. (7.3) and (7.4), respectively.

The analytic energy gradient for the NOMO/HF method with respect to a center $\mathbf{X}$ of a basis function is formulated by,

$$\frac{\partial E_{\mathrm{NOMO/HF}}}{\partial \mathbf{X}} = \sum_{\mu\nu}^{\mathrm{elec}} P^{\mathrm{e}}_{\mu\nu} \frac{\partial T^{\mathrm{e}}_{\mu\nu}}{\partial \mathbf{X}} + \sum_{\mu\nu}^{\mathrm{nuc}} P^{\mathrm{n}}_{\mu\nu} \frac{\partial T^{\mathrm{n}}_{\mu\nu}}{\partial \mathbf{X}}$$

$$+ \frac{1}{2} \sum_{\mu\nu\lambda\sigma}^{\mathrm{elec}} P^{\mathrm{e}}_{\mu\nu} P^{\mathrm{e}}_{\lambda\sigma} \frac{\partial \langle \mu\lambda \| \nu\sigma \rangle}{\partial \mathbf{X}} + \sum_{\mu\nu}^{\mathrm{elec}} \sum_{\lambda\sigma}^{\mathrm{nuc}} P^{\mathrm{e}}_{\mu\nu} P^{\mathrm{n}}_{\lambda\sigma} \frac{\partial \langle \mu\lambda | \nu\sigma \rangle}{\partial \mathbf{X}}$$

$$+ \frac{1}{2} \sum_{\mu\nu}^{\mathrm{nuc}} \sum_{\lambda\sigma}^{\mathrm{nuc}} P^{\mathrm{n}}_{\mu\nu} P^{\mathrm{n}}_{\lambda\sigma} \frac{\partial \langle \mu\lambda \| \nu\sigma \rangle}{\partial \mathbf{X}}$$

$$- \sum_{\mu\nu}^{\mathrm{elec}} \sum_{i}^{\mathrm{occ}} \varepsilon_i C^*_{\mu i} C_{\nu i} \frac{\partial S_{\mu\nu}}{\partial \mathbf{X}} - \sum_{\mu\nu}^{\mathrm{nuc}} \sum_{I}^{\mathrm{occ}} \varepsilon_I C^*_{\mu I} C_{\nu I} \frac{\partial S_{\mu\nu}}{\partial \mathbf{X}}. \qquad (7.6)$$

Here, $S_{\mu\nu}$ is overlap matrix between the μth and νth basis sets.

7.3. Computational details

This chapter examines the isotope effect in dihydrogen-bonded systems, $NH_4^+\cdots BeH_2$, $LiH\cdots C_2H_2$, and $BH_3\cdots HF$ as shown in Figure 7.1: namely, H_a and H_b are substituted by deuterium or tritium. Since the isotope effect is normally caused by the nuclear motion such as zero-point vibration, which is the largest nuclear quantum effect in energy, at least H_a and H_b should be treated quantum-mechanically. For this purpose, the NOMO/HF calculations were performed in this chapter. In the NOMO calculations, the nuclei H_a, H_b and their isotope substitutions were treated as nuclear orbitals and the

others were classically treated as point charges. Strictly, the present calculations correspond to the semi-quantal (or semi-classical) approach. One of the main reasons for the usage of this approach is that the quantum effects of the heavier atoms are negligibly small. Another reason is that the many-body effect, in particular, electron-nucleus correlation, becomes stronger as the heavier atoms are treated. If the fully quantal approach is adopted, the accuracy of the NOMO/HF calculations should deteriorate. As a comparison, the conventional MO/HF calculations were carried out as well.

The 6-311++G(d,p) set [21,22] was adopted as the EBFs. (5s5p5d) primitive Gaussian functions were used for the NBFs, of which the exponents were determined by the even-tempered scheme [8,23].

Geometry optimizations, which determine the positions of classical nuclei and the orbital centers of the NBFs, were performed by using the analytical energy gradient method in the NOMO theory as described in section 7.2. The averaged positions of quantal nuclei were evaluated as expectation values of nuclear position operator as follows:

$$\boldsymbol{R}_0 = \left\langle \Phi_0 \middle| \hat{\boldsymbol{R}} \middle| \Phi_0 \right\rangle = \left\langle \Phi_0^{\mathrm{n}} \middle| \hat{\boldsymbol{R}} \middle| \Phi_0^{\mathrm{n}} \right\rangle . \tag{7.7}$$

The NOMO/HF calculations and geometry optimizations were performed by modifying the GAMESS program package [24]. In the geometry optimizations, Hessian was numerically calculated using the BFGS method [25-28].

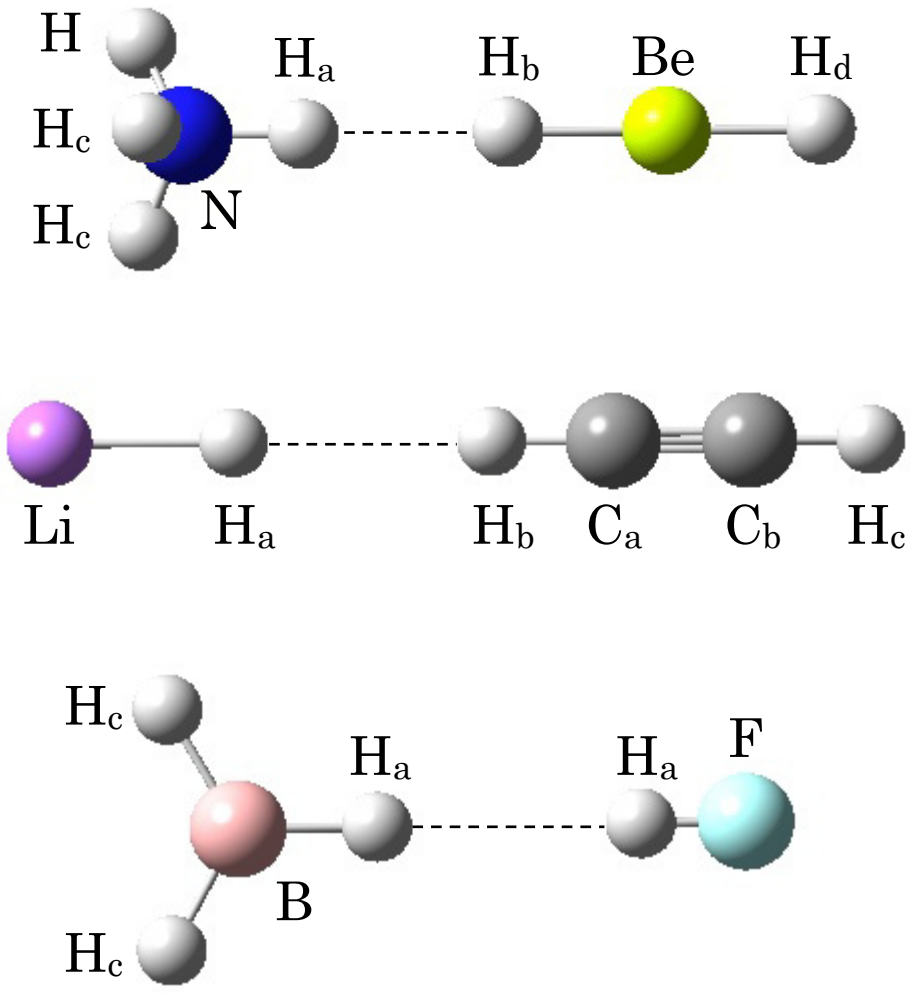

Figure 7.1. Geometries of $NH_4^+\cdots BeH_2$, $LiH\cdots C_2H_2$, and $BH_3\cdots HF$.

7.4. Results and discussion

First, bond distances of $H_3NX^+\cdots XBeH$ (X = H, D, and T) were evaluated by the NOMO/HF method as well as the conventional MO/HF method. The results are summarized in Tables 7.1-7.3. Here, X_a, X_b, H_c, and H_d correspond to the labels described in Figure 7.1.

Since the bond distances calculated by the MO/HF method correspond to the equilibrium distances, reflecting potential minima, the values are the same for X = H, D, and T. In other words, the values correspond to the classical limit of isotope substitutions: that is, nuclear mass $m_p \rightarrow \infty$. On the other hand, the bond distances calculated by the NOMO/HF method reflect the quantum effect of two hydrogen atoms, namely, the zero-point vibration. Therefore, the difference given by

$$\Delta R = R(\text{NOMO/HF}) - R(\text{MO/HF}) \tag{7.8}$$

corresponds to the vibrational averaging shift, which originates from the nuclear quantum effect and the anharmonicity. In Table 7.1, the values of ΔR are given in parentheses.

As is well-known in the conventional MO method, the evaluations of equilibrium distances are strongly affected by many-body effect, i.e. electron correlation. On the other hand, important factors for computing averaged distances are not only many-body effect but also vibrational averaging. The present chapter adopted the energy gradient technique at the NOMO/HF level as the first step. Thus, the many-body effect is not included in the present calculations. The NOMO/HF method can effectively take the vibrational averaging into account. Suppose that the many-body effect cancels out, the difference ΔR should be suitable in discussing the vibrational averaging, namely, the GIE.

Table 7.1. Bond distances (Å) of $H_3NX^+\cdots XBeH$ by the NOMO/HF and MO/HF methods.

Bond	NOMO/HF						MO/HF
	X = H		X = D		X = T		
R(N-X_a)	1.0492	(0.0280)	1.0406	(0.0193)	1.0368	(0.0156)	1.0212
R(X_a-X_b)	1.7260	(–0.0187)	1.7316	(–0.0131)	1.7342	(–0.0105)	1.7447
R(X_b-Be)	1.3790	(0.0276)	1.3709	(0.0195)	1.3674	(0.0159)	1.3514
R(H_c-N)	1.0103	(–0.0003)	1.0104	(–0.0002)	1.0104	(–0.0001)	1.0105
R(Be-H_c)	1.3164	(–0.0004)	1.3166	(–0.0003)	1.3166	(–0.0002)	1.3169

* Vibrational averaging shifts defined by Eq. (7.8) are shown in parentheses.

As shown in Table 7.1, the absolute values of ΔR decrease for $H_3NX^+\cdots XBeH$ as a heavier isotope is treated, that is, H → D → T. The shifts are small in the N−H_c and Be−H_d bonds because these atoms are treated classically. ΔR decrease in the N−X_a and X_b−Be bonds for the heavier isotope substitutions. It is natural to interpret that the negative shifts are brought by the anharmonicity of the N−X_a and X_b−Be potential curves. On the other hand, ΔR of the X_a−X_b bond increase as the heavier isotope is treated. It can be called an inverse isotope effect in the sense that the isotope effect shortens bond distances although normal isotope effect stretches bond distances.

The potential energy curve of the H_a−H_b bond, which was calculated by the MO/HF method fixing the other geometric parameters, has a normal shape involving the anharmonicity [29]. Thus, the inverse isotope effect is not the primary effect. It can be speculated as follows: The heavier isotope substitution primarily brings about the smaller polarization of the N−X_a and X_b−Be bonds, as seen in the shrinkage of these bonds. The smaller polarization secondarily leads to weakening the dihydrogen bond between X_a−X_b.

Let us focus on bond distances of $LiX\cdots XC_2H$ and $H_2BX\cdots XF$ (X = H, D, and T). The distances of both complexes are shown in Tables 7.2 and 7.3, respectively. Here, the labels correspond to the description in Figure 7.1. The differences ΔR corresponding to the vibrational averaging shifts are given in parentheses.

Table 7.2. Bond distances (Å) of $LiX\cdots XC_2H$ by the NOMO/HF and MO/HF methods.

Bond	NOMO/HF						MO/HF
	X = H		X = D		X = T		
R(Li-X_a)	1.6327	(0.0285)	1.6243	(0.0201)	1.6206	(0.0163)	1.6043
R(X_a-X_b)	2.2266	(–0.0240)	2.2324	(–0.0183)	2.2350	(–0.0157)	2.2507
R(X_b-C_a)	1.0856	(0.0232)	1.0785	(0.0161)	1.0754	(0.0130)	1.0624
R(C_a-C_b)	1.1859	(0.0008)	1.1857	(0.0006)	1.1856	(0.0005)	1.1851
R(C_b-H_c)	1.0555	(0.0001)	1.0555	(0.0000)	1.0555	(0.0000)	1.0555

* Vibrational averaging shifts are shown in parentheses.

Table 7.3. Bond distances (Å) of $H_2BX\cdots XF$ by the NOMO/HF and MO/HF methods.

Bond	NOMO/HF						MO/HF
	X = H		X = D		X = T		
R(B-X_a)	1.2172	(0.0259)	1.2095	(0.0182)	1.2061	(0.0148)	1.1913
R(X_a-X_b)	2.2247	(–0.0336)	2.2319	(–0.0264)	2.2347	(–0.0236)	2.2583
R(X_b-F)	0.9183	(0.0202)	0.9124	(0.0143)	0.9098	(0.0116)	0.8981
R(H_c-B)	1.1863	(–0.0003)	1.1864	(–0.0002)	1.1864	(–0.0002)	1.1866

* Vibrational averaging shifts are shown in parentheses.

Generally, both systems exhibit a similar tendency of $H_3NX^+\cdots XBeH$: The absolute values of ΔR decrease as a heavier isotope is treated, that is, H→ D → T. Specifically, Li−X_a and X_b−C_a bonds in $LiX_a\cdots X_bC_2H$ and B−X_a and X_b−F bonds in $H_2BX_a\cdots X_bF$ are shortened because of the anharmonicity and X_a−X_b bond in both systems are slightly stretched because of the secondary isotope effect, i.e., the inverse isotope effect.

Figure 7.2 illustrates the vibrational averaging shifts ΔR directly related to X_a and X_b in the three dihydrogen-bonded systems. Absolute shifts of X_a−X_b are in the order of $H_2BX\cdots XF$, $LiX\cdots XC_2H$, and $H_3NX^+\cdots XBeH$. ΔR decreases for heavier isotopes and seem to approach zero for a large nuclear mass. This is consistent with the previous discussion on the classical limit $m_p\rightarrow\infty$. The gradients with respect to the isotope substitutions H→ D → T are positive for X_a−X_b and negative for the others, which correspond to inverse and normal isotope effects, respectively.

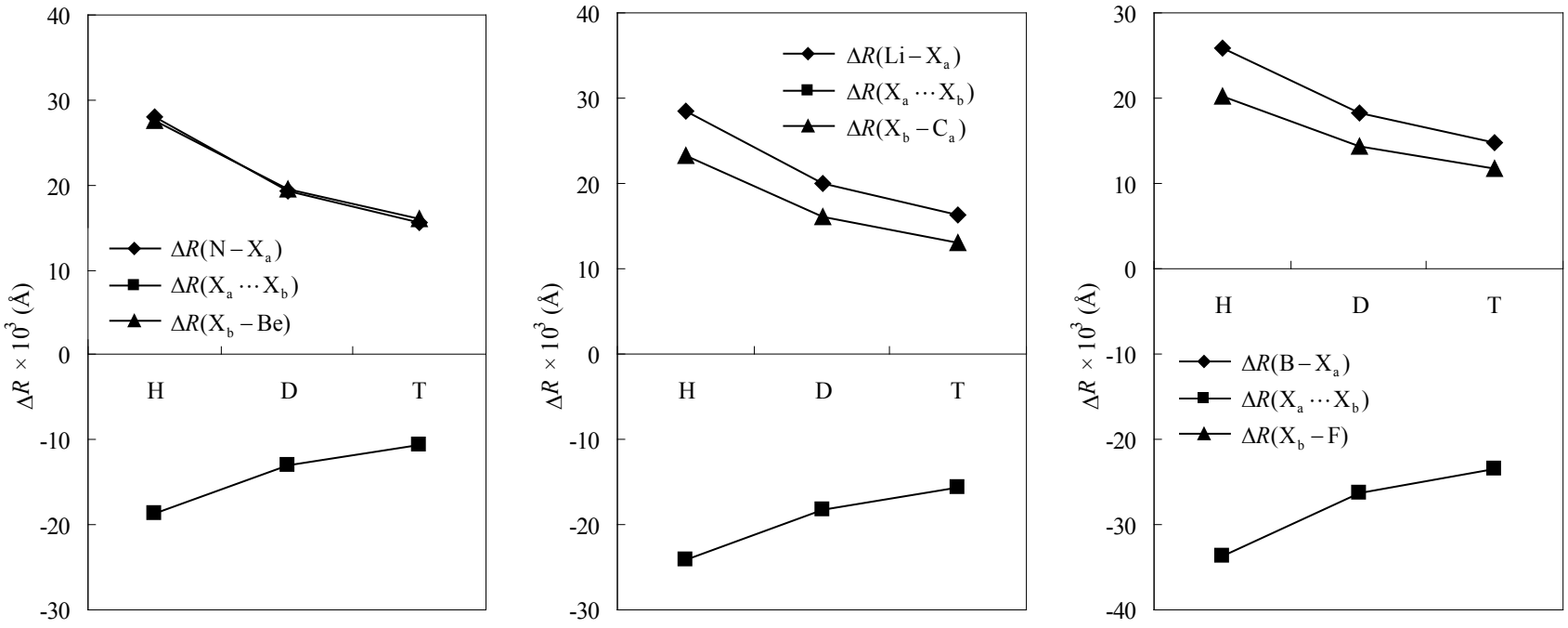

Figure 7.2. Vibrational averaging shifts ΔR in the dihydrogen-bonded systems, $H_3NX^+\cdots$ XBeH, $LiX\cdots XC_2H$, and $H_2BX\cdots XF$, which are the results of the NOMO/HF and MO/HF calculations.

7.5. Conclusion

This chapter investigated geometric isotope effects of the dihydrogen bond by using the analytical energy gradients in the HF calculations of the NOMO theory. The optimized structures of $H_3NX^+\cdots XBeH$, $LiX\cdots XC_2H$, and $H_2BX\cdots XF$ for X = H, D, and T demonstrated that the X···X bond distances are correlated with the weight of X, namely, H···H distance is shorter than D···D and T···T. It indicated that heavier isotope substitution weakens the dihydorogen bond. The bond shortening of typical covalent bonds with respect to the isotope substitution of X was also confirmed.

References

[1] R. Custelcean, J. E. Jackson, *Chem. Rev.* **101**, 1963 (2001).

[2] L. M. Epstein, E. S. Shubina, *Coord. Chem. Rev.* **231**, 165 (2002).

[3] S. J. Grabpwski, W. A. Sokalski, J. Leszezynski, *J. Phys. Chem. A* **109**, 4331 (2005).

[4] H. Cybulski, M. Pecul, J. Sadlej, T. Helgaker, *J. Chem. Phys.* **119**, 5094 (2003).

[5] S. J. Grabowski, W. A. Sokalski, *J. Phys. Org. Chem.* **18**, 779 (2005).

[6] A. Hayashi, M. Shiga, M. Tachikawa, *J. Chem. Phys.* **125**, 204310 (2006).

[7] M. Tachikawa, K. Mori, H. Nakai, K. Iguchi, *Chem. Phys. Lett.* **290**, 437 (1998).

[8] H. Nakai, *Int. J. Quantum Chem.* **86**, 511 (2002).

[9] H. Nakai, K. Sodeyama, M. Hoshino, *Chem. Phys. Lett.* **345**, 118 (2001).

[10] H. Nakai, K. Sodeyama, *J. Chem. Phys.* **118**, 1119 (2003).

[11] K. Sodeyama, K. Miyamoto, H. Nakai, *Chem. Phys. Lett.* **421**, 72 (2006).

[12] H. Nakai, M. Hoshino, K. Miyamoto, S. Hyodo, *J. Chem. Phys.* **122**, 164101 (2005).

[13] H. Nakai, M. Hoshino, K. Miyamoto, S. Hyodo, *J. Chem. Phys.* **123**, 237102 (2005).

[14] M. Hoshino, H. Nakai, *J. Chem. Phys.* **124**, 194110 (2006).

[15] K. Miyamoto, M. Hoshino, H. Nakai, *J. Chem. Theory Comput.* **2**, 1544 (2006).

[16] M. Hoshino, Y. Tsukamoto, H. Nakai, *Int. J. Quantum Chem.* **107**, 2575 (2007).

[17] K. Sodeyama, H. Nishizawa, M. Hoshino, M. Kobayashi, H. Nakai, *Chem. Phys. Lett.* **433**, 409-415 (2007).

[18] H. Nakai, *Int. J. Quantum Chem.* **107**, 2849 (2007).

[19] Y. Imamura, H. Kiryu, H. Nakai, *J. Comput. Chem.* **29**, 735 (2008).

[20] S. P. Webb, T. Iordanov, S. Hammes-Schiffer, *J. Chem. Phys.* **117**, 4106 (2002).

[21] R. Krishnan, J. S. Binkley, R. Seeger, J. A. Pople, *J. Chem. Phys.* **72**, 650 (1980).

[22] T. Clark, J. Chandrasekhar, P. V. R. Schleyer, *J. Comput. Chem.* **4**, 294 (1983).

[23] R. D. Bardo, K. Ruedenberg, *J. Chem. Phys.* **60**, 918 (1974).

[24] M. W. Schmidt *et al.*, *J. Comput. Chem.* **14**, 1347 (1993).

[25] C. G. Broyden, *Math. Comput.* **21**, 368 (1967).

[26] R. Fletcher, *Comput. J.* **13**, 317 (1970).

[27] D. Goldfarb, *Math. Comput.* **24**, 23 (1970).

[28] D. F. Shanno, *Math. Comput.* **24**, 647 (1970).

[29] K. Miyamoto, M. Hoshino, H. Nakai, unpublished data.

General conclusion

In Part I of this thesis, the author performed the theoretical extension and numerical assessment of the LRD method. In Chapter 2, the LRD method was extended to the SCF treatment. An efficient algorithm enabled us to compute the differentiation of atomic polarizabilities with respect to electron density. Although total energy and electronic distribution changed negligibly from those by the post-SCF approach, the analytical gradient based on the SCF treatment enabled the geometry optimization of dispersion-dominated complexes. In Chapter 3, the performance of the LRD method for open-shell systems was numerically assessed. Dispersion coefficients and atomic polarizabilities by the LRD method behaved reasonably in open-shell atoms and molecules. The results of open-shell van der Waals complexes and radical dimers showed the usefulness of the LC-BOP+LRD method for open-shell noncovalent interactions. In Chapter 4, the LRD method was extended to the excited-state calculation. The difference density matrix of TDDFT enabled state-specific dispersion correction. The LRD method combined with the LC-BOP functional accurately reproduced interaction energies of π-π*/n-π* excited molecular complexes and their shifts from the ground state. Furthermore, the LRD method improved the binding energy of aromatic excimers even though the exciton delocalization and charge-transfer interaction are dominant components of intermolecular attraction forces.

The results of Part I broadened the applicability of the LRD method to various phenomena: for example, the geometry searching of molecular clusters, the prediction of intermolecular magnetic interaction, and the investigation of photochemistry of molecular aggregates. Another interesting application of the LRD method is the physical adsorption on metallic surfaces. Not only dispersion force but also other interactions such as charge transfer and orbital-orbital interaction can be important. Before the application to metallic systems, further numerical assessment is required. The implementation of the LRD method in the program package using the plane-wave basis may be helpful. Theoretical advance might be required because of large deviations of C_6 coefficients of metal atoms as reported in Chapter 3. The local response approximation and the dispersion relation are expected to be improved.

In Part II, the isotope effect in noncovalent interactions was theoretically investigated using the NOMO theory, which is a WFT determining both electronic and nuclear .wavefunctions. In Chapter 6, the intermolecular GIE in the hydrogen bond was analyzed. First, the RVS-SCF method, which is an interaction energy decomposition method for conventional HF calculations, was extended to the NOMO framework. As a result of calculating the shift of energy components, the intramolecular bond shrinkage weakened the electrostatic interaction. On the other hand, the intermolecular bond elongation weakened the exchange-repulsion interaction to stabilize the total system. In Chapter 7, the GIE in the dihydrogen bond was investigated using the analytical energy gradient of the NOMO/HF energy. The averaged distance of proton and hydride increased with increasing nuclear mass. This tendency was contrary to the shrinkage of intramolecular covalent bonds.

For the future, the NOMO method is expected to be applied for other noncovalent interactions. For example, according to the recent study on the physisorption of cyclohexane on Rh(111) surface, the deuteration of cyclohexane weakens the surface-molecule interaction by 8.1 kJ/mol. This value is significantly larger than the weakening of the hydrogen bond reported in Chapter 6. The NOMO method will be helpful for the interpretation of this remarkable isotope effect.

The author hopes that the methodologies treated in this thesis will provide novel insights of various phenomena related to noncovalent interactions.

Acknowlegments

本研究は早稲田大学化学・生命化学科中井浩巳教授のご指導のもとで行われました。中井教授には研究室配属以来の 6 年間，電子状態理論の詳細から研究者としての心構えまで様々なことをお教え頂きました。また，海外での学会発表やアイオワ州立大学での滞在などの貴重な機会を与えてくださりました。本論文の作成にあたっても数多くのご助言を頂きました。ここに厚く御礼申し上げます。

また，本論文をまとめるにあたり同化学・生命化学科の古川行夫教授，井村考平准教授，山梨大学の常田貴夫特任教授から多くのご助言，ご意見を頂きました。心より感謝致します。

中井研究室の先輩である小林正人博士，赤間知子博士，渥美照夫博士には，研究室配属時から研究内容のみならず研究発表の技術につきましても様々なご助言を頂きました。本論文の第一部につきましては，LRD 法の開発者である佐藤健博士よりプログラムの実装および研究内容に関する貴重なご助言を頂きました。所属した班のリーダーであった清野淳司博士には，研究を進める上で大変お世話になりました。さらに，筆者と同じく博士課程に進んだ大越昌樹修士，吉川武司修士はじめ優秀な後輩たちに恵まれた環境で研究に集中することができました。第二部の研究は，主に学士および修士課程在籍時に行われました。NOMO 班の先輩方である今村穣博士，星野稔博士，西澤宏晃博士からは手厚いご指導を賜りました。時には研究の方向性を見失い苦悶したこともありましたが，同期生である後潟敬介修士，表達矢修士，河崎素良修士，藤井厚彦修士がいたことで乗り越えることができました。皆様に感謝の意を表します。

また，2009 年度から 2011 年度においては，文部科学省グローバル COE プログラム「実践的化学知教育研究拠点」による研究費の補助を頂き，円滑に研究を進めることができました。ここに御礼申し上げます。

最後に，大学入学から学位取得まで経済的，精神的に支援してくれた家族に感謝致します。

List of Achievements

1. Original Articles

1. ○"Self-consistent field treatment and analytical energy gradient of local response dispersion method"
   Y. Ikabata, T. Sato, H. Nakai
   Int. J. Quant. Chem. **113**, 257 (2013).

2. ○"Assessment of local response dispersion method for open-shell systems"
   Y. Ikabata, H. Nakai
   Chem. Phys. Lett. **556**, 386 (2013).

3. ○"Extension of local response dispersion correction to excited-state calculation based on time-dependent density functional theory"
   Y. Ikabata, H. Nakai
   J. Chem. Phys. **137**, 124106 (2012).
   This paper was seleceted as the Research Highlights of "*The Journal of Chemical Physics*", and is one of the Top 20 Most Read Articles in October 2012 and November 2012.

4. "Development of the explicitly correlated Gaussian-nuclear orbital plus molecular orbital theory: Incorporation of electron-electron correlation"
   H. Nishizawa, Y. Imamura, Y. Ikabata, H. Nakai
   Chem. Phys. Lett. **533**, 100 (2012).

5. ○"Interpretation of Intermolecular Geometric Isotope Effect in Hydrogen Bonds: Nuclear Orbital plus Molecular Orbital Theory"
   Y. Ikabata, Y. Imamura, H. Nakai
   J. Phys. Chem. A **115**, 1433 (2011).

6. ○“Isotope effect in dihydrogen-bonded systems: application of analytical gradient method in the nuclear orbital plus molecular orbital theory”
   H. Nakai, Y. Ikabata, Y. Tsukamoto, Y. Imamura, K. Miyamoto, M. Hoshino
   Mol. Phys. **105**, 2649 (2007).

2. Conference Presentations

International Conference

1. “Extension of Local Response Dispersion Method to Excited-State Calculation”
   Y. Ikabata, H. Nakai
   5th Asian Pacific Conference of Theoretical and Computational Chemistry
   T-21.6, Rotorua (New Zealand), December 2011.

2. “Local response dispersion method: implementation and assessment”
   Y. Ikabata, H. Nakai
   The 6th Global COE International Symposium on ‘Practical Chemical Wisdom’
   P45, Tokyo (Japan), December 2011.

3. “Extension of Local Response Dispersion Method to Time-Dependent DFT Calculation”
   Y. Ikabata, H. Nakai
   3rd NIMS(MANA)-Waseda International Symposium
   PS34, Tokyo (Japan), November 2011.

4. “Implementation and numerical assessment of local response dispersion method”
   Y. Ikabata, H. Nakai
   The Seventh Congress of the International Society for Theoretical Chemical Physics
   3PP-22, Tokyo (Japan), September 2011.

5. “Assessment of local response dispersion method in open-shell systems”
   Y. Ikabata, H. Nakai
   The 5th Global COE International Symposium on ‘Practical Chemical Wisdom’
   P42, Tokyo (Japan), January 2011.

6. “Theoretical study on isotope effects in hydrogen-bonded systems: Extension of Morokuma analysis to *ab initio* NOMO method”
   Y. Ikabata, Y. Imamura, H. Nakai
   4th Asian Pacific Conference of Theoretical and Computational Chemistry
   PP15, Port Dickson (Malaysia), December 2009.

Domestic Conference

1. “局所応答分散力法を用いた時間依存密度汎関数理論の確立”
   五十幡康弘・中井浩巳
   日本化学会第 93 春季年会，2G3-39，草津，2013 年 3 月発表予定.

2. “局所応答分散力(LRD)法を用いた励起状態における分子間相互作用計算”
   五十幡康弘・中井浩巳
   第 6 回分子科学会シンポジウム，P004，東京，2012 年 6 月.

3. “Divide-and-Conquer (DC)プログラムによる
   リニアスケーリング量子化学計算”
   小林正人・赤間知子・當眞嗣貴・吉川武司・五十幡康弘・中井浩巳
   第 2 回次世代ナノ統合シミュレーションソフトウェア説明会,
   P43，東京，2012 年 1 月.

4. “局所応答分散力(LRD)法の開殻系および励起状態への展開”
   五十幡康弘・中井浩巳
   第 5 回分子科学討論会，1E12，札幌，2011 年 9 月.

5. “局所応答分散力(LRD)法の GAMESS への実装”
   五十幡康弘・中井浩巳
   スーパーコンピュータワークショップ 2011，P13，岡崎，2011 年 1 月.

6. “局所応答分散力(LRD)法の数値検証：開殻分子系を中心として”
   五十幡康弘・中井浩巳
   第 4 回分子科学討論会，3P092，大阪，2010 年 9 月.

7. “局所応答分散力(LRD)法の数値検証：現実系への適用を目指して”
   五十幡康弘・中井浩巳
   シンポジウム「電子状態理論の新機軸」，P21，岡崎，2010 年 8 月.

8. “分散力を考慮した高速な DFT 計算法の開発：DC-LRD”
   五十幡康弘・佐藤健・中井浩巳
   日本コンピュータ化学会 2010 春季年会，1P16，東京，2010 年 5 月.

9. “NOMO 法を用いた水素結合系における同位体効果の理論的研究”
   五十幡康弘・今村穣・中井浩巳
   第 8 回早慶ワークショップ，東京，2009 年 10 月.

10. “NOMO-gradient 法の開発と水素結合系への応用”
    五十幡康弘・塚本泰弘・今村穣・星野稔・中井浩巳
    第 1 回日本化学会関東支部大会，1P-052，東京，2007 年 9 月.

11. “NOMO 法による二水素結合の量子効果に関する理論的研究”
    五十幡康弘・塚本泰弘・今村穣・星野稔・中井浩巳
    第 1 回分子科学討論会，3P042，仙台，2007 年 9 月.

3. Awards

1. Best Student Talk, 5th Asian Pacific Conference of Theoretical and Computational Chemistry, December 2011.

2. 優秀ポスター賞，第 1 回日本化学会関東支部大会，2007 年 10 月.